UNIVERSITY OF OKLAHOMA

GRADUATE COLLEGE

INVESTIGATING THE SYNTHESIS OF TRANSITION METAL OXIDE

NANOSTRUCTURES IN A COUNTER-FLOW FLAME

A DISSERTATION

SUBMITTED TO THE GRADUATE FACULTY

in partial fulfillment of the requirements for the

Degree of

DOCTOR OF PHILOSOPHY

By

MOIEN FARMAHINI-FARAHANI
Norman, Oklahoma
2014

INVESTIGATING THE SYNTHESIS OF TRANSITION METAL OXIDE
NANOSTRUCTURES IN A COUNTER-FLOW FLAME

A DISSERTATION APPROVED FOR THE
SCHOOL OF AEROSPACE AND MECHANICAL ENGINEERING

BY

_____
Dr. Wilson Merchan-Merchan, Chair

_____
Dr. Subramanyam Gollahalli

_____
Dr. Feng Lai

_____
Dr. Takumi Hawa

_____
Dr. Andrew Madden

I dedicate my dissertation to my loving parents

Zari and Morteza

& my brother

Amin

Acknowledgements

Table of Contents

List of Tables

List of Figures

Abstract

In this dissertation, the synthesis and growth mechanisms of various transition metal oxide (TMO) nanostructures inside a counter-flow flame medium were investigated. Transition metal oxide nanostructures with distinctive properties have broad applications in microelectronic devices, gas sensors, lithium-ion batteries, and catalysts. A flame is an exothermic chemical reaction that provides required energy for inexpensive synthesis of TMO nanostructures. The counter-flow flame is characterized by high temperature and chemical species gradients, one-dimensional axial temperature variation, and an oxygen-rich zone suitable for growth of metal oxide nanomaterials. Transition metal oxide nanostructures can be grown and collected through both solid-support and gas-phase synthesis methods inside a counter-flow flame.

Herein, grown TMO nanostructures include Nb_2O_5, ZnO, W-doped MoO_3, and WO_x nanostructures. The insertion of a high purity Nb probe in the flame resulted in an instantaneous formation of a material layer coating the surface of the probe. The results show that the material layer is composed of Nb_2O_5 nanorods. Size and growth rate of the Nb_2O_5 nanorods depend on the insertion positions of the Nb probe (source) inside the flame volume. Content of oxygen in the oxidizer stream plays an important role in the growth rate of Nb_2O_5 nanorods; higher oxygen content leads to higher growth rates. Low electron mobility of Nb leads to the basal growth mechanism for the synthesis of Nb_2O_5 inside the flame. On the other hand, transition metals with high electron mobility (such as Mo, W, and Zn) mainly form through the vapor-phase growth mechanism inside the flame. The vapor-phase growth mechanism was observed during the growth of ZnO nanostructures through the solid-support synthesis. It was found that the

morphology of the grown ZnO nanocrystals strongly depends on the insertion position inside the flame. Structural variations of the synthesized ZnO nanostructures include nanorods and microprisms with a large number of facets, and microprisms with a protruding nanorod. Grown nanorods are less than 100 nm in diameter and less than 1μm in length.

W-doped MoO_3 nanocubes were synthesized through the gas-phase synthesis by introducing high purity Mo and W probes inside the counter-flow flame volume. Energy dispersive X-ray spectroscopy elemental mapping shows evenly distributed W, Mo, and O_2 in the nanocubes. The measured lattice spacing of the nanocubes showed expanded lattice spacing which was attributed to an intercalation of tungsten atoms in the MoO_3 layers. Collected samples of fully grown W-doped MoO_3 nanocubes in the upper region of the flame volume show that the nanocubes have widths of less than 100 nm and well-defined edges like their base structures of MoO_3.

By inserting a high purity W probe inside the flame volume, fragments of tungsten oxide material formed over the oxidizer side of the W probe. We found that this material can be converted to 1-D tungsten oxide nanorods with lower oxidation state (WO_x) as exposed to the electron beam (EB) of a TEM. In this process, tungsten oxide nanorods reached ~90% of their final length within approximately one second of EB irradiation. The EB irradiation led to evaporation of a part of the fragment and subsequent growth of lower state tungsten oxide (WO_x) nanorods in the vicinity of the irradiation spot. It revealed that grown WO_x nanorods follow the vapor-phase growth mechanism. The evaporated material particles coalesced and deposited on the TEM grid to form seeds for further growth. These early seeds were the building blocks for the

formation of fully grown structures. Further influx of tungsten particle deposition on the surface of the seeds caused growth of the seeds in the preferred direction and formation of the nanorods. The smooth surface was evidence of total diffusion of deposited particles into the surface of the early formed nanorods. The length of WO_x nanorods was an exponential function of their distance to the irradiated spot. Longer nanorods were observed closer to the irradiated spot. This finding gives another unique characteristic of the flame to synthesize TMOs.

Much of the material in chapters 3, 4, and 6 of this dissertation is verbatim from published journal papers. Co-authors have granted full authority for the reproduction of the material.

The journal papers are the following:

1. W. Merchan-Merchan and M. Farmahini-Farahani, "**Rapid Catalyst-Free Flame Synthesis of α-Nb$_2$O$_5$ Micro/Nanorods**," *Materials Chemistry and Physics, 140, 516, 2013.*
2. W. Merchan-Merchan and M. Farmahini-Farahani, "**Flame Synthesis of Zinc Oxide Nanocrystals**," *Material Science and Engineering B, 178, 127, 2013.*
3. W. Merchan-Merchan, M. Farmahini-Farahani, Z.M. Rosenberg, "**Electron-beam Induced Formation of Tungsten Sub-Oxide Nanorods from Flame-Formed Microcrystals,"** *Mircon, 57, 23, 2014.*

Transition Metal Oxide Nanostructures

1-1- Motivation

Transition metal oxide (TMO) nanostructures can be produced using different synthesis methods such as chemical vapor deposition, laser deposition, plasma, sol-gel, etc. However, in all the above-mentioned methods, TMO nano/microstructures are produced through a batch-to-batch production process which might require pre-processing and/or post-processing and often vacuum equipment to provide a suitable environment for growth of nanostructures. Also, low growth rate of materials produced through some methods prevent them from being suitable for industry. Consequently, these methods cannot be considered for an inexpensive production of TMO nanostructures on a large scale. In contrast, flame synthesis runs in the atmospheric pressure, does not requires post-processing or pre-processing, provides the required energy for synthesis directly from the combustion reactions, and as a result, is an inexpensive method compared to other common methods. In addition, flame synthesis is an efficient method since it provides high temperature and chemical species, high growth rate of materials, controllability (by adjusting flame fuel/oxidizer ratio, geometry of source, and source insertion position), and continuous production (maintaining a constant flow process as opposed to batch-to-batch processes). As a result, flame synthesis is considered a cost effective and continuous method for TMO nanostructure production.

The one-dimensional counter-flow flame, established by oppositely impinging oxidizer and fuel flows, is only characterized by high temperature and chemical species gradient in the axial direction (in this dissertation Z height represents the distance from

the edge of fuel nozzle to a certain point in the flame medium). In other words, a radially inserted probe (source material) is surrounded by local flame conditions such as temperature and oxygen concentration. Therefore, the counter-flow flame offers a simple and well-defined flame geometry facilitating control of nanostructures growth. The counter-flow flame provides an elevated temperature to evaporate metals (sources), the required oxygen and oxygen radicals to transfer metals to metal oxides, and suitable temperature gradient for vapor-phase growth of TMO nanostructures. For further details about the counter-flow flame reactor employed in this study, please refer to sections 2-1 and 2-2.

1-2- Why transition metal oxides?

Nowadays, researchers working in nanotechnology are discovering and producing unique functional materials/structures such as carbon nanotubes, one-dimensional to three-dimensional metal oxides, and nano-porous materials. Particularly, TMOs are favorable and advantageous materials covering a wide range from semiconductors and insulators to superconductors. With reduction in size to nanometer, unique chemical, electrical, and mechanical properties appear. Nanowires are ideal structures for investigating the transport phenomena in one-dimensional materials, this is beneficial both for understanding the fundamental phenomena in low-dimensional materials and developing a new generation of high performance nano-sized devices [1].

For instance, it is well-known that the electrical conductivity of metal-oxide semiconductors is very sensitive to the composition of the surrounding gases. This property can be utilized in the production of gas sensors. Oxygen vacancies on the surface of metal oxide materials cause changes in electrical conductivity of the

2

materials as a result of molecular adsorption. Consequently to the adsorption of some molecules, such as NO_2 or O_2 at the vacancy sites, conductivity is reduced. But the conductivity increases when molecules, such as CO and H_2, are adsorbed at the vacancy sites on the surface. Most metal-oxide gas sensors operate based on this principle [2].

1-3- Fabrication of nanostructures

Two different approaches are used to produce nano/micro-structures: top-down and bottom-up methods.

The top-down methods are based on reducing the size/dimensions of micron-sized materials to nano-size materials through etching and/or ion-beam milling. Commonly, techniques such as focused electron beam and focused ion beam are employed for reducing the size/dimensions of materials. Highly patterned and aligned nanostructures can be produced via the top-down method. However, this method is an expensive method which requires a long preparation time and also sometimes single-crystalline structures cannot be produced. Thus, at the moment, the top-down method cannot satisfy and meet the industrial limitations and requirements for an inexpensive production of a great amount of structures.

The bottom-up method is based on the assembly of molecules through evaporation and deposition on a surface through vapor-phase transport or chemical reactions such as electrochemical deposition and solution-based techniques. In this method, highly pure nanocrystalline materials with small dimensions can be produced in a low cost experimental procedure. Also, doped and mixed materials can be synthesized easily. However, material integration (e.g. the combination of oxygen with a metal to form a metal oxide) on the surface of substrates might be troublesome and

also, production of well-arranged and patterned structures is often very challenging in this method [2]. Common synthesis methods of TMO nanostructures such as CVD, sol-gel, and flame, are all categorized under the bottom-up methods.

1-4- Synthesis and growth mechanism of transition metal oxide nanostructures

Transition metal oxide nano/microstructures are grown by different synthesis methods. Based on the synthesis environment, synthesis methods can be categorized into three main groups: vapor-phase growth, solution (liquid) phase growth, and basal growth. The majority of the TMO nanostructures are synthesized through the vapor-phase growth. The base of vapor-phase growth is reactions between metal and oxygen in the gas phase. Either one of the two growth mechanisms, vapor-liquid-solid (VLS) or vapor-solid (VS), appears through vapor-phase growth. Solution-phase growth is an alternative method with flexibility. Basal growth (in flame synthesis) is only observed during the growth of elements with low electron mobility such as niobium oxide and tantalum oxide. Thus, this mechanism is rarely observed and investigated. This section briefly discusses the above-mentioned growth mechanisms for the synthesis of metal oxides.

1-4-1- Vapor-phase growth mechanism

In the vapor-phase growth mechanism, metal (source) is heated up and evaporates (vapor formation) by a thermal means. The chemical reaction between oxygen O_2 (or oxygen radicals O) and vapor metal controls the morphology and crystallinity of grown nanostructures. This growth mechanism can be observed in synthesis methods such as CVD, laser deposition, plasma, etc. The vapor-phase growth

4

mechanism is divided into two mechanisms: vapor-liquid-solid (VLS) and vapor-solid (VS) [3-5].

Essentially, VLS is a catalyst-assisted growth mechanism in which metal nanoparticles or nanoclusters play the role of nucleation seeds. The seeds govern the growth direction and dimension of nanostructures. Thus, appropriate selection of catalyst is crucial [6].

The vapor-solid mechanism occurs in catalyst-free synthesis processes [7-9]. Through the VS mechanism, metal (source) in a solid phase is heated into a vapor phase. The vapor is transported by carrier gases to a downstream region of lower temperature then directly condensed on the substrate surface or growing structures. The initially condensed vapors play the roles of seeds for further growth [10]. The growth rate and morphology of structures depend on supersaturation of the condensing vapors [11]. This mechanism depends on several thermodynamic parameters and requires quantitative modeling to support fundamental understanding.

1-4-2- *Solution-phase growth mechanism*

The solution-phase growth mechanism is based on a chemical reaction that occurs in a solution. The chemical reaction can be initiated by different means such as thermal and electron current. Researchers have used many methods to synthesize nanostructures via the solution phase growth mechanism. Some of these methods are electrochemical deposition [12], sol-gel deposition [13, 14], and hydrothermal deposition [15-17].

1-4-3- Basal growth mechanism

In the basal growth mechanism a metal source combines with oxygen and forms a metal oxide without detaching from the source. In this process a layer of metal oxide appears at first and structures grow with the base attached to the source. Since grown structures are always attached to the base (source), diffusion of oxygen to reach and combine with source plays an important role in growth rate and morphology of the structures. In the flame synthesis method, the basal growth mechanism is only observed during the growths of niobium, tantalum, and vanadium which have low electron mobility.

1-5- Flame synthesis methods

The vapor-fed aerosol flame synthesis is the combustion or hydrolysis (a chemical procedure in which a molecule of water is added to a matter) of volatile precursors in a hydrocarbon and/or hydrogen flame. In this method, a precursor converts from the gas phase into larger particles by surface reaction and/or coagulation and subsequently coalescence. This method is industrially employed. However, only a few volatile precursors are available at a reasonable cost. To solve the problem, the liquid-fed aerosol flame is suggested.

In the liquid-fed aerosol flame synthesis, typically a liquid precursor solution, instead of vapor, is sprayed and converted to the particle product and subsequently to solid nanoparticles similar to the vapor-fed aerosol flame synthesis. Sometimes hollow and shell-like particles are produced as a result of incomplete evaporation. Air-assist nozzles or ultrasonic nozzles are utilized to spray/atomize the solution. Also, the solution might be pre-heated to facilitate the evaporation process. The pre-heating

depends on the solution composition. For high enthalpy organic solutions, small pilot flames are used to ignite and keep the combustion. This entire process is called flame spray pyrolysis. For low enthalpy organic solutions, external larger flames serve as the hot walls similar to spray pyrolysis process which is called flame-assisted spray pyrolysis [18]. Flame-made particles can be collected or deposited with the different aids/substrates. Deposition and collection of particles at different temperatures lead to growth of material with different morphologies [19].

In both above-mentioned methods a precursor is fed into the flame. However, it is possible to introduce the precursor (source) into a flame to synthesize and collect materials from the surface of the source or from inside the flame volume. This method is called flame synthesis. In this method, both co-flow and counter-flow combustion reactors, different kinds of fuel such as hydrocarbon and/or hydrogen, and different oxidizers such as oxygen and/or air can be employed to form a flame. Geometry, temperature, and oxygen content of the flame can be modified by changing different parameters to form an appropriate flame for synthesis. Depending on the collection of grown materials from the flame (sampling methods), flame synthesis can be categorized into two synthesis methods: 1) solid support synthesis method in which grown structures are collected from the solid source material inserted inside the flame, and 2) gas phase synthesis method in which grown structures are collected from the flame gas environments while they are traveling inside the flame volume. In this dissertation all the materials are grown through a counter-flow flame synthesis method, and both solid support and gas phase synthesis methods are employed.

1-6- Combustion synthesis method

Combustion synthesis uses extremely exothermic chemical reactions between combustor and metals (source). The "combustion" covers gas-phase flame and explosion (incineration). This synthesis method is also known as self-propagating high-temperature synthesis (SHS) [20]. In conventional SHS of nano-sized materials, initial reactants are in the solid phase. The heterogeneity of micron-sized initial reactants makes the production of nano-sized material difficult through the conventional SHS method. In the SHS method, as a requirement, high ignition temperature (thousands of Kelvins) can be attained by laser radiation, an electric arc, or by a heating coil. Researcher are trying to lower the ignition temperature and use metal oxides instead of micron-sized metal powders [21].

1-7- Objective

Previous experimental investigations prove the feasibility of producing metal oxide nanostructures via flame synthesis. In this work, transition metal oxide nanostructures, including niobium oxide, zinc oxide, and tungsten-doped molybdenum oxide are synthesized directly and indirectly in the flame. Also, the growth of tungsten sub-oxide nanorods under electron beam is investigated.

The principal objective of this research study is to increase the fundamental understanding of the growth mechanisms of metal-oxide nanostructure formation through the flame synthesis. Also, it presents that flamed formed tungsten oxide fragments can be transform to tungsten oxide nanorods with lower oxidation state under an electronic beam through the vapor-phase growth mechanism. It means, in case of providing suitable source of energy and source material, the vapor-phase growth

mechanism can be applied to a wide range of material growth. Secondly, this research study underscores feasibility of the counter-flow flame in producing TMO nanostructures through a simple single-step process.

The principal research components of this dissertation are:

1. Conducting experiments in a counter-flow flame to characterize the effects of flame temperature, oxygen concentration, and other controllable process parameters on nanostructure morphologies.

2. Examining the influence of the nature of the transition metal components (Zn, Nb, W, and Mo) on the growth mechanism and morphology of nanostructures. The energy source alone cannot cause vapor-phase growth, rather the source material plays an important role in the growth mechanism. In this step, a comparison is made with previous works in this field.

3. Investigating the influence of electron beam (energy source), which elevates enthalpy for transformation to vapor-phase, on the formation of nanostructure materials and the reduction to lower oxidation state.

4. Characterizing the synthesized nanostructures by means of scanning electron microscopy (SEM), high-resolution transmission electron microscopy (HRTEM), and energy dispersive X-ray spectroscopy (EDX); and proposing a growth mechanism based on characterization of the nanostructure.

1-8- Outline of this dissertation

Chapter one is dedicated to a general discussion on the synthesis of transition metal oxide nanostructures, advantages of the flame synthesis method over other conventional methods, and the objective of the dissertation. Chapter 2 describes the

experimental setup of the counter-flow burner employed to provide a suitable environment for growth of nanomaterials. Details of the counter-flow combustion reactor are discussed. Chapter 3 focuses on the basal growth of niobium oxide nano/micro-rods after introduction into the flame. The effect of temperature and oxygen content on the growth of material is discussed. Chapter 4 presents vapor-solid growth of zinc oxide via counter-flow flame synthesis. Change in the morphology of grown structures as a result of changing probe configuration is discussed. Chapter 5 examines the gas-phase synthesis of mixed tungsten and molybdenum oxide inside the flame volume. As material traveled towards the stagnation plane, they mixed and formed mixed metals oxides. In order to investigate the vapor-phase growth mechanism in an environment different from the flame, a new chapter is introduced. Chapter 6 presents growth of tungsten sub-oxide nanorods under an electron beam in the TEM. Finally, Chapter 7 offers some concluding remarks and suggestions for future research.

Counter-Flow Diffusion Flame and Experimental Apparatuses for

Synthesis of Nanostructures Experimental setup

In this study, various TMO nanostructures are synthesized by employing a combustion reactor which produces a counter-flow diffusion flame. In a counter-flow flame, fuel and oxidizer are introduced through nozzles in opposite directions and the flame forms between the nozzles. In these experiments, fuel and oxidizer flow from the top nozzle and bottom nozzle, respectively. The fuel used throughout all experiments is 96% methane (CH_4) and 4% acetylene (C_2H_2) (acetylene is also known as ethyne), and the oxidizer is a mixture of 50% oxygen (O_2) and 50% nitrogen (N_2). Nitrogen contained in air is used for the oxidizer flow. Gas mixture chambers are used to mix methane and acetylene in the fuel flow and oxygen and nitrogen in the oxidizer flow. They are located upstream of both nozzles. All gasses pass through mass flow controllers which have the precision of 1.5% and control the mass flow rates. Both nozzles (oxidizer and fuel) have diameters of 42 mm and are separated by a distance of 25.4 mm (one inch). Also, nitrogen is introduced parallel to the fuel and oxidizer flow from an annular duct around the oxidizer nozzle. The nitrogen flow has two roles. 1) It makes a protective shield to maintain a stable flame. 2) It prevents flame dissipation into the surroundings. Additionally, a series of stainless steel screens are placed at the fuel and oxidizer nozzles and a honey comb plate is located in the duct for the nitrogen flow. They make the gasses flow more uniformly and, as a result, help the flame stability. To transfer heat from the exhaust gases, cold water continuously flows through the exhaust chamber. Figure 2-1 shows a schematic image of the counter-flow diffusion reactor and control devices. The position of the probe holder with respect to the

11

combustion reactor is shown in figure 2-2, item number 11. The probe holder (and material source) is introduced radially into the flame.
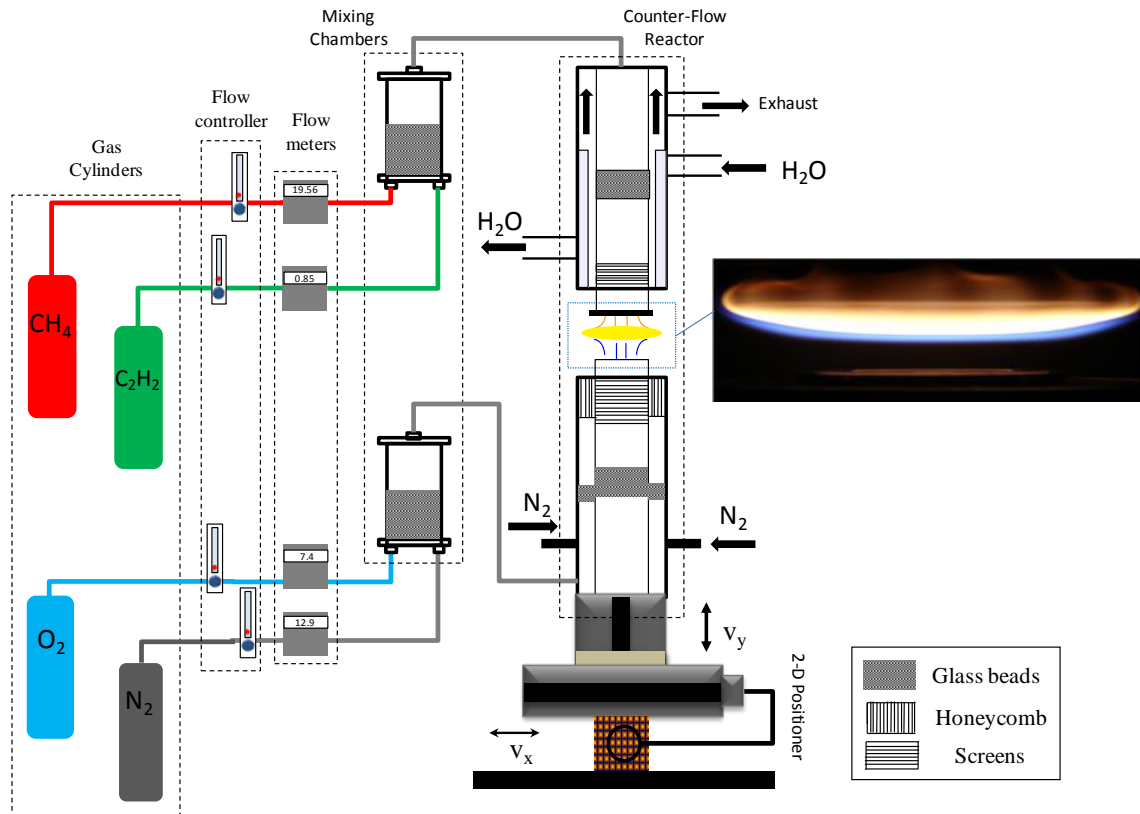
Figure 2-1- A schematic of the setup of the combustion reactor. Flow controllers and flow meters control and measure gas flow rates before entering in mixing chambers. The fuel enters the combustion zone through the top nozzle and the oxidizer through the bottom nozzle. The insert shows a photograph of a typical diffusion flame formed in the counter-flow reactor.

2-2- Counter-flow flame characteristics

The counter-flow flame with its unique structure provides a suitable medium for growth of TMO nanostructures. Advantages of the counter-flow flame are explained as follows: 1) it has one-dimensional geometry which provides constant temperature and oxygen concentration at each axial position inside the flame; 2) The blue zone has high temperature and oxygen concentration which is an ideal environment for transformation of metal to metal oxide; 3) it is a higher stable flame throughout the synthesis

experiments, in contrast to other flame types such as co-flow diffusion flames; 4) the thickness of the blue and yellow zones can be controlled by changing the oxygen content and strain rate (see section 2-6); 5) Carbon content of the yellow zone can easily be employed to produce hybrid carbon coated TMO nanostructures.

1. Screens
2. Glass beads
3. Honeycomb
4. Flame
5. Exhaust
6. Fuel inlet
7. Oxidizer inlet
8. Water inlet
9. Water outlet
10. Nitrogen curtain inlets
11. Probe and probe holder
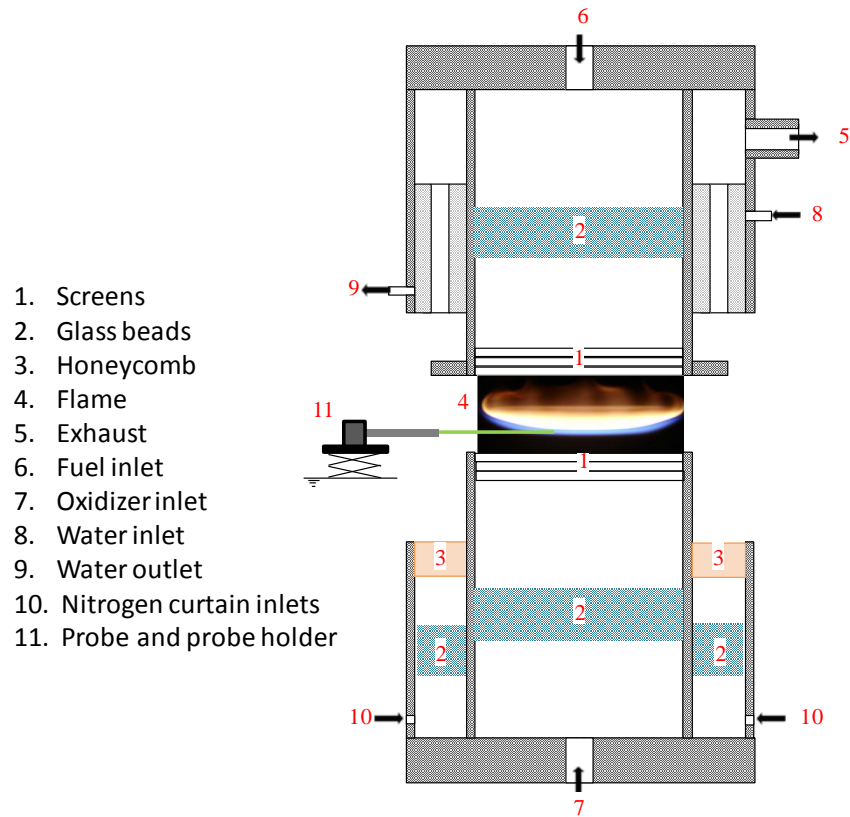
Figure 2-2- A schematic representation of gas flow directions in the counter-flow burner. The photograph shows a typical flame formed in the counter-flow burner. The insertion of a probe for nanomaterial synthesis is shown.

2-3- Positioning system

A stepper motor (UniSlide Velmex) with capability of moving in two directions was employed to change the position of the reactor. This positioning system allows obtaining a precise position of a probe inside the flame at various Z heights. The stepper motors are controlled through a computer with COSMOS V3.1.4 software. The

13

accuracy of this system is a faction of a millimeter with error less than 1.5e-4 (0.0015"/10"). A schematic of the positioning system is shown in figure 2-3.
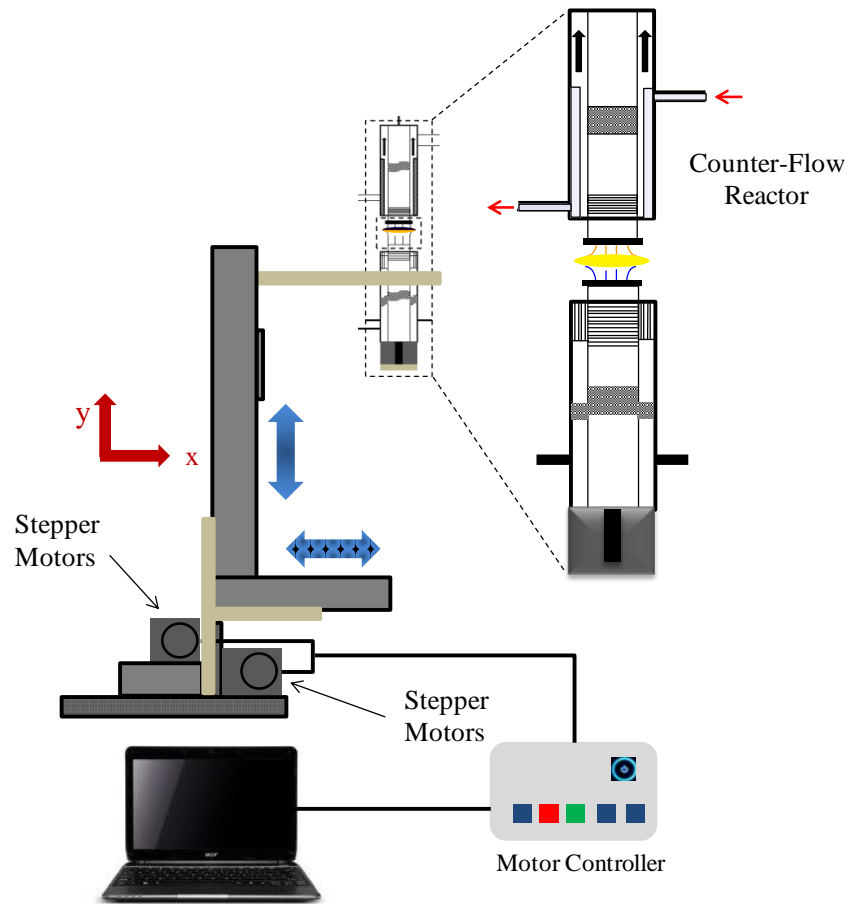
Figure 2-3- Schematic of the positioning system including the stepper motors which moves the reactor in two directions. The stepper motors are connected to a PC for control and movement.

2-4- Thermophoretic sampling method

To characterize structural and chemical composition of nanostructures grown inside the flame we need to capture them directly from the flame. Since the nanostructures form and transform in a narrow zone of the flame (blue zone), a highly accurate method is required. To capture grown materials in the gas-phase synthesis of TMO nanostructures, we utilized the thermophoretic sampling technique developed for studying soot formation by Dobbins and Megaridis [22]. In this technique, a sampler is

14

mounted on a 15° angled platform as shown in the figure 2-4. This particular angle limits the travel time of a TEM grid in the flame (high-temperature zone), thus it prevents the grid from burning inside the flame. The sampler has been employed in previous studies and the following description is extracted from those studies with authors' permission [23]. The sampler consists of a 50 mm stroke compressed-air piston controlled by a pneumatic valve (ModelSY5140, SMCCorp. of America), which drives the grid in and out of the flame. Thermophoretic deposition is driven by the presence of a temperature gradient that exists between the cold surface of the grid and the flame. The exposure of the grid inside the flame should last long enough to capture samples, but be short enough to maintain a temperature gradient between the flame and the grid. An electronic time controller sets the residence time of the grid inside the flame while the travel time is regulated by the air cylinder pressure. The cold surface of the grid freezes heterogeneous reactions of captured particles that can be analyzed later using TEM and HR-TEM. This precise technique can be operated in co-flow and counter-flow flames, making the recreation of nanomaterial synthesis evolution inside the flame volume possible, and also allowing for the characterization of its morphology. The utilized TEM grid has a substrate made of copper mesh with a thin film (~20nm) of pure carbon deposited on one side of the grid. The variable Z in our studies represents the axial distance from the edge of the burner's nozzle to approximately the center of the TEM grid inserted within the flame volume.
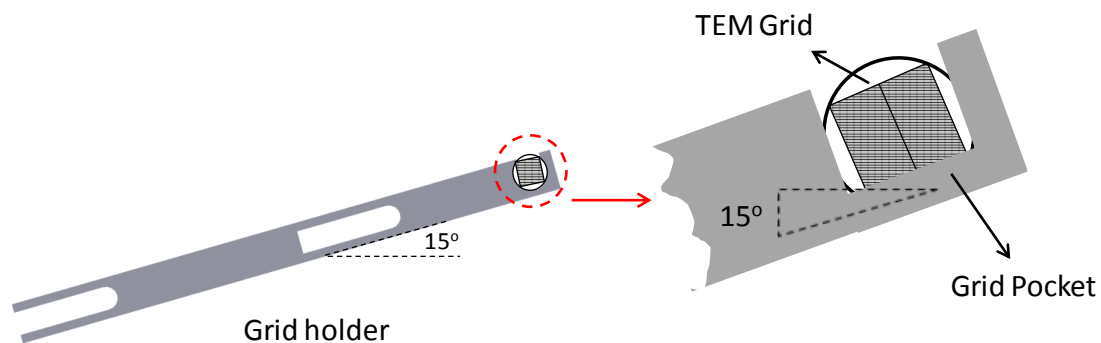
Figure 2-4- Schematic of TEM grid holder employed to capture formed samples from the flame directly.
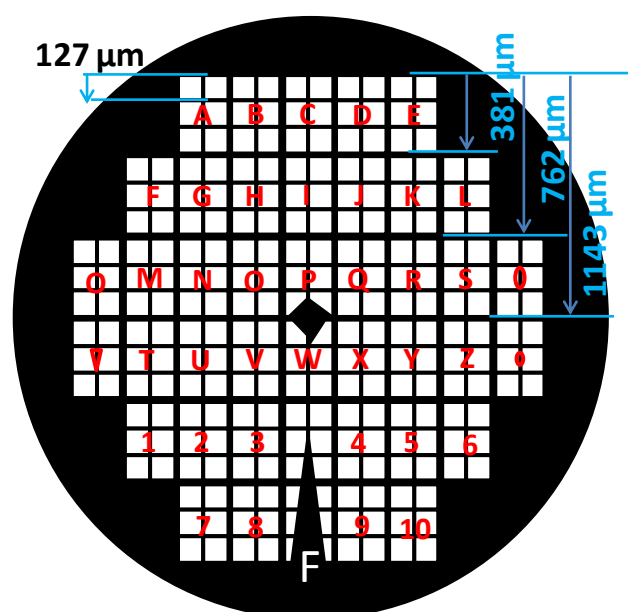
Figure 2-5- H2 Finder (index) grid. Letters in each block assist the microscopist to track the position of the particles/structures. Letters in the TEM grid allow tracking the precise position of the flame formed structures and development of the synthesized materials inside the flame volume.

All experiments involving gas-phase flame synthesis are performed using the thermophoretic sampling method. Nanostructures, which are collected using this technique, are studied using transmission electron microscopy (TEM). The H2 Finder (index) TEM grids (SPI Supplies) are used in order to gain a better understanding about the evolution and growth of material inside the flame. Each section on H2 Finder grid has a name which can be seen even under a light microscope. Named sections help a

microscopist to track the exact position of the grown structures. A schematic of the grid is shown in figure 2-5. For each experiment, the grid is shot five times inside the flame. The trajectory of the gird in and out of the flame volume is ~10 msec and residence time of the grid is ~30 msec; this gives enough time for collecting materials and preventing burnout and damage to the carbon coated grid.

2-5- Source material holder

A source holder device was employed to hold the source material in place when positioned in the flame throughout all experiments in this research. The source holder is an assembly of a cubic body, cylindrical tube, shield, and supports as shown in figure 2-6. The source holder is mounted on a laboratory vertical jack platform for precise positioning and control of probe insertion inside the flame. A 2.5 mm ID cylindrical tube with inner inserts is used to hold the source material. A larger tube with inner diameter of ~6 mm is used as a shield to protect the formed structures after the experiment time and when the source is taken out from inside the flame. Inside and tip support hold the source materials firm during the experiments. The source holder assembly is used for both types of gas-phase and solid-support experiments. The sample holder is used to hold the metal probe (source) firmly inside the flame. The sample holder can also be easily moved in the axial direction of the flame.
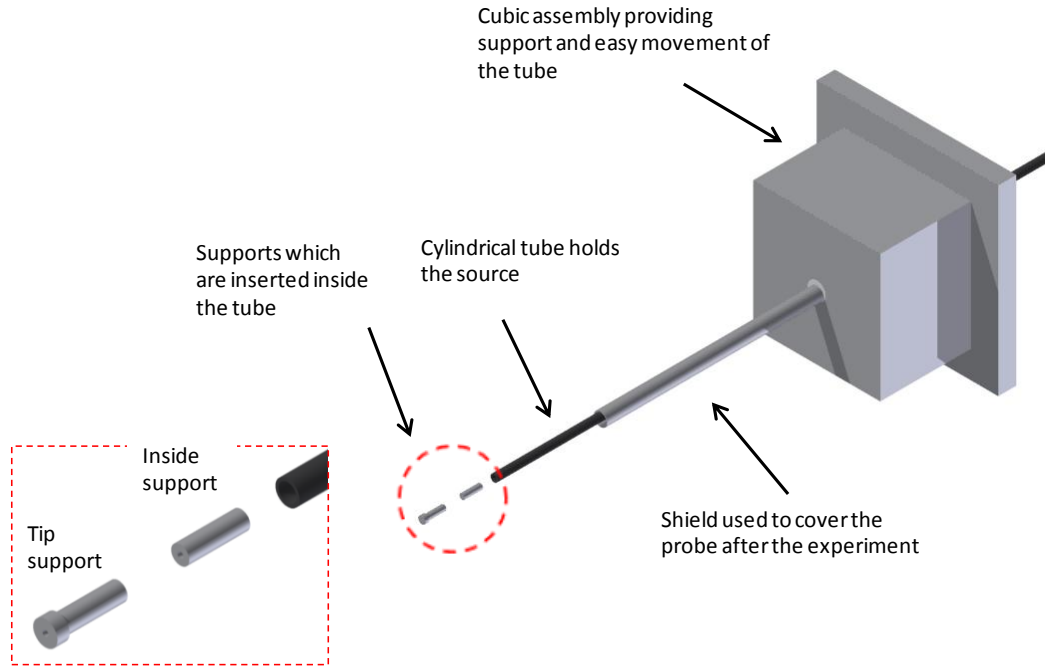
Figure 2-6- Schematic of probe holder, cubic assembly, tube, supports, and the shield.

2-6- Effect of oxygen and gas flow velocity on the counter-flow flame

We can change the geometry of the flame by 1) changing the oxygen content; 2) changing the strain rate (gas velocity) to add to flexibility of the flame. Flame temperature, chemical species concentration, and thickness of the blue zone (the suitable zone for growth of TMO nanostructures) vary by changing the flame geometry. At constant strain rate of 20 s^{-1} for both the fuel and oxidizer streams, by variation of the oxidizer oxygen content from 21% (air-based flame) to 100% (figure 2-7a) the following can be observed: 1- the air-based flame (21% O$_2$) has the thinnest blue zone; 2- the 100% O$_2$ flame has the thickest blue zone; 3- by introducing higher oxygen the flame is compressed which decreases the overall flame thickness; 4- by introducing higher oxygen, the stagnation planes along with the highest temperature plane are moved towards the fuel nozzle and the distance between them decrease.

18
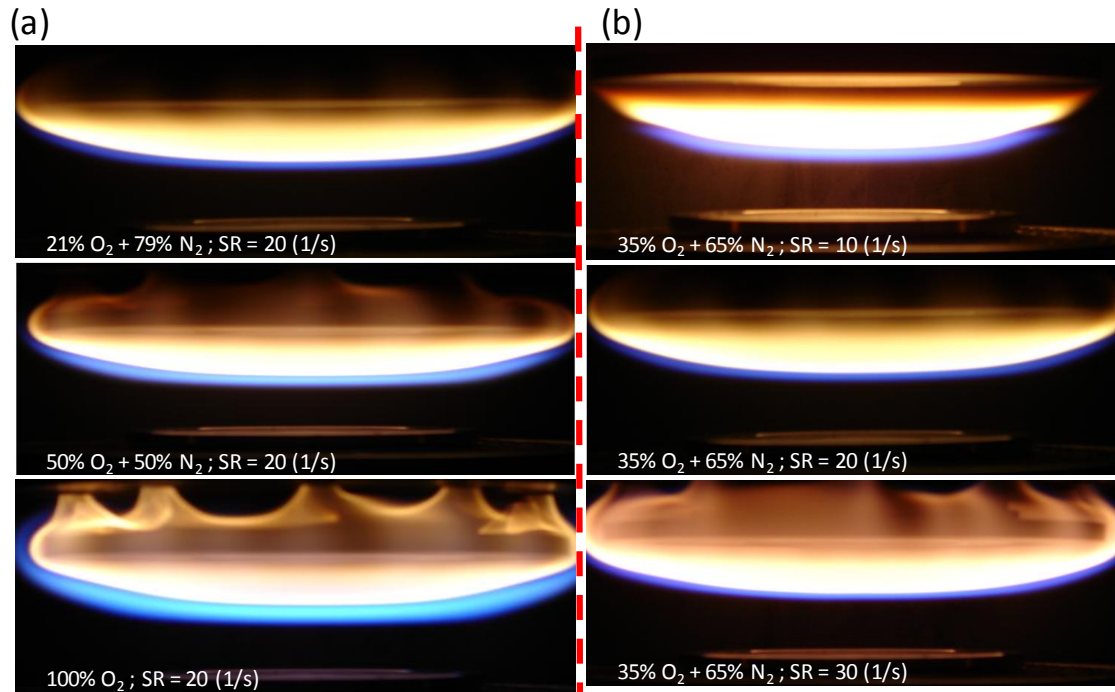
Figure 2-7- Photographs of the flame with different S.R and oxygen content; effects of (a) oxygen content; (b) strain rate on the flame geometry [24].

In addition, the gas velocity (momentum) of the fuel and oxidizer that impinge against each other causes variations in the flame geometry and temperature. The strain rate (S.R) with unit of s^{-1} is an indication of velocity the flows between the two nozzles. A higher strain rate means a faster gas introducing/flowing from the nozzles. The strain rate is calculated using the following equation:

$$S.R = \frac{2V}{D}$$

Where, S.R is strain rate, V is velocity of the gas flow, and D is the distance between the two nozzles. By maintaining the oxidizer concentration of 35% O_2 and 65% N_2 and changing the strain rates from 10 s^{-1} to 40 s^{-1} (figure 2-7b) (by changing the outlet flow velocities) the following can be observed: 1) by increasing the S.R, the brightness of the yellow zone decreases; 2) by increasing the S.R, the blue zone

becomes thinner; 3) by increasing the S.R, the flame thickness decreases. By experimental and computational analyses, it is found that a higher strain rate renders diffusion flame thinner, and thermal thickness is inversely proportional to square root of the strain rate [25].

2-7- Material characterization employed in this study

To prepare samples for TEM analysis the synthesized structures were mechanically removed from the probe and mixed with methanol. The mixture was sonicated for few minutes. A droplet of the mixture was placed on a TEM grid with carbon film and allowed to dry. In order to prepare powder for XRD analysis the grown structure were scraped off the probe. Since more accurate XRD analysis requires more powder material, several experiments are required to collect enough powder for XRD analysis.

2-7-1- Scanning electron microscopy

Scanning electron microscopy (SEM) is a basic tool for present nanotechnology characterization, and is used to observe/investigate the morphologies of as-grown nanostructures, and estimate/analyze the size of those nanostructures. Zeiss NEON and JEOL JSM-880 are two major high resolution SEMs at Samuel Roberts Noble Microscopy Laboratory at the University of Oklahoma that were used for this work.

2-7-2- Transmission electron microscopy

A transmission electron microscope (TEM) uses an electron beam instead of a light source compared to a light microscope. Since electrons have lower wavelength than light, higher resolution (1000 times higher) can be achieved. JEOL 2000-FX and

JEOL 2010F are available for research at Samuel Roberts Noble Microscopy Laboratory at the University of Oklahoma and also JEOL 3010F at UIC Research Resources Center - University of Illinois at Chicago was employed to investigate flame grown structures.

2-7-3- *Energy-dispersive X-ray spectroscopy*

In order to understand elemental characterization of flame-grown materials Energy-dispersive X-ray spectroscopy (EDS or EDX) is used. The elemental compositions of as-prepared nanomaterials grown through the flame synthesis are analyzed using EDS.

2-7-4- *X-ray diffraction*

For structural characterization of materials, the powder diffraction technique is used. This technique uses X-ray electron diffraction on powder samples. The powder X-ray diffractometer that is used in this research is Rigaku Ultima IV and it is located at the physical and environmental geochemistry laboratory at the school of Geology and Geophysics.

Counter-Flow Flame Synthesis of Niobium Oxide Nanostructures[1]Introduction

Niobium (Nb), vanadium (V), and tantalum (Ta) are in group five of the periodic table. The lighter three group five elements (Nb, V, and Ta) appear naturally and have similar properties; for instance, they are used as hard refractory metals (resistant to heat). Niobium exhibits very low mobility due to its high stability and very low solubility [26]. The reactivity of these elements is not evident because of the fast appearance of a stable oxide layer that prevents further reactions [27]. This stable layer also prevents the vapor-phase growth of niobium oxide. Stoichiometric niobium oxides mostly appear in four main forms: NbO, Nb_2O_3, NbO_2 and (α, β-) Nb_2O_5. NbO, Nb_2O_3 can be produced by melting Nb_2O_5 with Nb.

In this chapter, the flame synthesis of niobium pentoxide (Nb_2O_5) nano/micro structures using a counter-flow flame is discussed for the first time. The growth process of Nb_2O_5 occurs in a few minutes. The source material in form of a one-millimeter diameter high purity (%99.99) niobium probe was inserted in the oxygen-rich zone of the flame. Individual and coalesced micro/nanorods are rapidly formed on both sides (fuel and oxygen) of the Nb wire. Grown structures on each side have different morphologies; however, they form based on the same growth mechanism. The morphology of the grown Nb oxide structures significantly depends on the insertion positions inside the flame. The characterization of strong axial gradients of both temperature and chemical species of the flame leads to the alteration in morphology.

---

[1] The content of this chapter is an extension of a published paper by the author. The paper contains results of research which was solely conducted as partial fulfillment for the PhD requirement. Materials presented in the paper have not been submitted for a course or extra credit.

Nb_2O_5 structures grow through the basal growth mechanism due to the constant flow of oxygen onto the surface of niobium metal. Highly dense adjacent nanorods coalesce and form micro/nanorods. The flame temperature is sufficiently high to transform grown rods to monoclinic α-Nb_2O_5. Scanning electron microscopy (SEM), transmission electron microscopy (TEM), high resolution TEM, selected area electron diffraction (SAED) pattern imaging, X-ray diffraction (XRD), and Energy-dispersive X-ray spectroscopy (EDS) are employed to analyze the grown structures.

3-1-1- Applications

Among TMOs, niobium-oxide micro/nanostructures have wide applications in areas such as in sensors [28], solar cells [29], ferroelectric compounds [30], capacitors [31], optic glasses [32, 33], lithium-ion batteries [34], catalysts [35], electron emitters [36] and electrochromic devices [37] (figure 3-1). The Nb_2O_5 compound exhibits higher chemical stability and corrosion resistance than other niobium oxides. Different applications require different morphologies and structures. For example, high length-to-width aspect ratio is favorable in polymer technology [38], larger surface area is favorable for catalysts [39], bio-applications require pattern porous structures with high aspect ratio and adjustable pore size [40], semiconductors with wider band gap such as Nb_2O_5 are more favorite options for electrochemic devices [41]. As noted above, the wide range of applications of Nb oxide makes the study of Nb_2O_5 very attractive. Robust methods need to be developed for the generation of the structures.

23
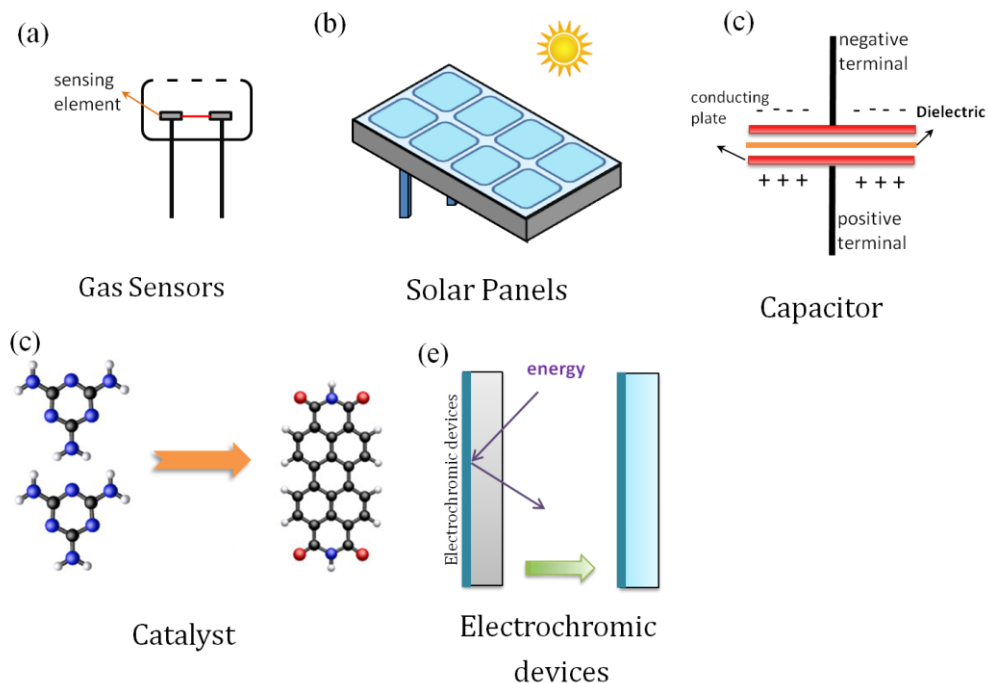
Figure 3-1- Typical applications of niobium oxide nano/micro structures; (a) gas sensor; (b) solar panel; (c) capacitor; (d) catalyst; (e) electrochromic device.

3-2- Current synthesis methods of niobium oxide nano/microstructures

Since niobium oxides show favorable characteristics, many research groups have employed various methods to fabricate niobium oxide nanostructures. For instance, the sol-gel method [29, 37], magnetron sputtering [33], chemical vapor deposition (CVD) [42], anodization [39, 43], plasma [44, 45], and pulse laser decomposition [46] have all been used to synthesize and control the morphologies and properties of niobium oxides. A brief discussion on current methods, including their advantages and limitations, is presented below.

3-2-1- Chemical vapor deposition method

In the chemical vapor deposition method, thin films of material can be grown on a substrate (usually silicon) through some chemical reactions. Oxygen and/or non-

reactive gases are fed into a furnace chamber (in lower pressure) and the gases react with the metal (source) and deposit on the substrate to form a thin film of metal oxide. A variety of CVD configurations have been established and examined for the synthesis of TMOs, such as horizontal furnace (most popular), vertical furnace and plasma enhanced CVD [47]. Few research groups have used CVD methods in order to synthesize Nb_2O_5.

O'Neil et al. (2003) [42] reported use of atmospheric pressure chemical vapor deposition for coating Nb_2O_5 on SiCo-coated float glass substrates via the reaction of $NbCl_5$ and ethyl acetate at 400-660˚C. The formed films show unexpected hydrophilicity with respect to water droplets with a contact angle of 60˚ for a pre-irradiated sample and a contact angle of 5-20˚ for irradiated samples.

Dabirian et al. (2010) [48] employed a high-vacuum CVD method with a precursor of niobium tetraethoxy-dimethyl-amino-ethoxide. The investigations of niobium oxide deposition were carried out at different substrate temperatures. The film growth rate of 220 nm/h was measured and the film was found to be homogenous all over the wafer. The XRD analysis showed that the films are polycrystalline Nb_2O_5. Although CVD methods have been widely used for synthesis of various TMOs, they have some limitations. For instance, the CVD processes require relatively high temperatures, thus dimensional tolerances are important restrictions and also this process requires vacuum conditions that cause low growth rate and make scaled-up production difficult. In addition, due to the use of catalyst or specific substrates, the processes might involve contamination.

3-2-2- Sol-gel method

The sol-gel method is based on the formation of an oxide network through reactions of a metal (source) in a solution. A sol is a stable dispersion of amorphous or crystalline particles in a solvent. And a gel encompasses a solution. In the sol-gel method, the film of material is formed from agglomeration of the particles.

Avellaneda et al. (1998) [37] used two alkoxy methods to prepare a transparent and stable niobium alkoxide solution. Sol one was prepared by a sonocatalytic procedure and allowed coatings with decent optical and electrochromic properties to be obtained. The solution was $NbCl_5$ powder in C_4H_9OH and $C_2H_4O_2$. This solution was ultrasonically irradiated for a few minutes. In the second method they did not use ultrasonic irradiation. Sol two was prepared by synthesizing Nb pentabutoxide, $Nb(OBu_n)_5$, by dissolving $NbCl_5$ in butanol, to which sodium butoxide was added under reflux. The process led to the formation of $Nb(OBu_n)_5$ and NaCl. NaCl was separated by centrifugation. The ultimate sol was formed by mixing the precursor with $C_2H_4O_2$ resulting in a stable sol at 20 ˚C. In this work they reported that sol one was easier and quicker in preparing sols than the other methods and this method avoided the possibility of Na residue. Also, they studied the electrochemical and microscopic characterization and electrochromic properties of both Nb_2O_5 from sol-gel coatings and dip-coating on an indium-tin oxide (ITO-) coated glass. Results show both methods can produce electrochromic materials with lithium electrolyte.

Pawlicka et al. (1995) [49] described a novel synthesis method of Nb_2O_5 through a sol-gel method and reported the electrochromic properties of Nb_2O_5 coatings formed on an ITO-coated glass. A stable niobium solution was prepared through a

sonocatalytic procedure that provided a coating with electrochromic properties. The initial solution was made by mixing powder $NbCl_5$, C_4H_9OH and $C_2H_4O_2$. The solution was irradiated ultrasonically for a few minutes. The coating was formed by dipping ITO-coated glass substrate into the solution in room conditions. They showed that Nb_2O_5 films grown by the sonocatalytic procedure exhibited excellent electrochromic properties. Coatings grown at 600 ˚C present a good, reversible and fast insertion and extraction of lithium ions. Solution phase methods, such as the sol-gel method, usually require some preparations such as cleaning, distillation, draining (drying) and sometimes annealing or post-heating. Furthermore, low growth rate and imperfect crystallinity might occur due to low growth temperature.

3-2-3- Anodization method

An electrochemical process that converts the metal surface into a metal oxide film is called anodizing. The oxide film can be grown on certain metals such as, niobium, tantalum, and zirconium through the anodizing process. For each metal there is a specific process condition which promotes growth of the film with a uniform thickness. Several researchers have been working on anodizing niobium and producing niobium oxide film.

Sieber et al. (2005) [50] anodized niobium in mixtures of H_2SO_4/HF as electrolytes. They found that hydrofluoric (HF) acid concentration and anodization time play essential roles on morphology and layer thickness; and uniform porous Nb oxide layers can grow under perfect electrochemical conditions. Also, they measured diameters of approximately 25 nm for pore diameters.

Yang et al. (2011) [51] reported the fabrication of hierarchical morphology with a super hydrophobic surface through a self-organized anodizing process. In their experiment, a niobium sheet with a purity of 99.9% and a thickness of 0.2 mm were employed to grow the film. Potential differences from 10 to 15V were applied to the sheet in mixed glycerol electrolyte at 443 K in dry nitrogen atmosphere. They showed that changing applied potential leads to different morphologies of niobium oxide microcones with different tip angles. They also found that by coating the surfaces with a fluoro alky phosphate layer, the surfaces become super hydrophobic with a contact angle of 175˚ and a contact angle hysteresis of approximately 2˚. Anodization results depend upon the nature of an electrolyte solution and its concentration, the applied voltage, and the temperature, which need several steps of preparation. Furthermore, most methods yield slow growth rates, consequently requiring a long process time.

3-2-4- Plasma (arc discharge) methods

With the plasma method, two graphitic probes perform as the negative and positive electrodes. An electrical discharge is created as a result of a conducting path between the two electrodes.

Mozetic and Cvelbar (2005 and 2007) [44, 45] have reported the use of oxygen plasma for synthesis of Nb_2O_5. A foil of 99.9% purity and thickness of 0.025 mm and diameter of 20 mm was employed as the source. Plasma was generated with a 27.12 MHz frequency and 150 W powers. Results show that foils are coated with crowded bundles of 10 µm long and 50 nm thick nanowires. They also mentioned that grown structures via plasma treatment are formed rapidly (90 s) in comparison with other

methods. However, the plasma method requires vacuum condition and high voltage. In addition, its growth rate is not as high as flame synthesis methods.

Table 3-1 lists different methods that are employed to synthesize niobium oxides nano/micro structures.

Table 3-1- List of different employed methods to grow niobium oxide nano/micro structures.

Method	Experimental configuration	Author(s)	Morphology of structures (schematic)
CVD		O'Neil et al.[42]	
		Dabirian et al.[48]	
Sol-gel		Avellaneda et al.[37]	
		Pawlicka et al.[49]	
Anodization		Sieber et al. [50]	
		Yang et al. [51]	
Plasma		Mozetic and Cvelbar [44, 45]	

3-2-5- Combustion and flame methods

Compared to other currently employed methods, the flame and combustion synthesis methods are usually a single-step process with no need for catalysts resulting in a rapid and inexpensive growth of micro/nanomaterials. For more information regarding different approaches of combustion and flame methods, please refer to sections 1-5 and 1-6. More details about the flame and combustion methods for growth of niobium oxide are explained in the following:
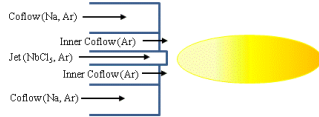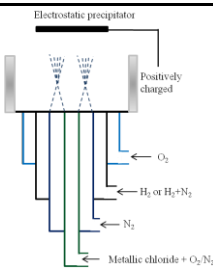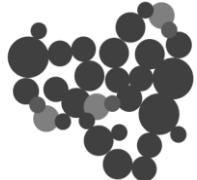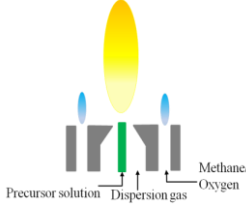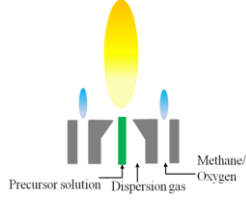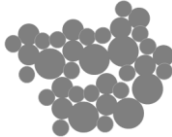
Guenin et al. (1988) [52] reported the formation of niobium oxide crystals through a hydrogen-oxygen flame reaction. Hydrolysis or/and oxidation of $NbCl_5$ and then condensation/deposition of vapor leads to the formation of niobium oxide particles. The reactor they employed was composed of four concentric tubes. The central and third tubes introduced metallic chloride vapor and hydrogen, respectively. The second tube introduced nitrogen as a screen to prevent the appearance of oxide on the tube. The fourth tube introduced oxygen. They produced pseudo-spherical, non-porous solid particles with a specific surface area (using BET method) of 50 m^2g^{-1}. The particles mostly showed isometric shapes and were isolated with an average diameter of ~35 nm.

Tomasi and Munir (2004) [53] used a self-propagating high-temperature synthesis (SHS) to study the effect of the reactants' sizes on wave propagation in the mixture of metal oxide fuel ($Al_2Zr + Al_2O_3$) and metal oxide (Nb_2O_5). The particle sizes affected the velocity of the self-propagating combustion wave. The experiments were carried out at 1 atm pressure of Ar in a stainless steel chamber. The specimens were inserted in the chamber on a graphite base and a preheating furnace around it. A uniform flame on the top of the specimens was formed. The flame affected the kinetics

of the wave. Fine particles were produced as a result of steady wave propagated for all dilutions. Other researchers such as Shon et al. (2001) [54], Zanetti et al. (2003) [55], Teleki et al. (2008) [56], Nuetzel et al. (2009) [57], Phanichphant et al. (2011) [58], and Yeh and Chen (2011) [59] have produced material combined with Nb through the combustion method.

Table 3-2 lists different niobium oxides and niobium alloys that are synthesized through different combustion and flame methods.

Table 3-2- List of different combustion/flame methods employed for the synthesis of niobium component and related structures.

Method	Experimental configuration	Author(s)	Composition	Morphology of structures
Jet flame		Nuetzel et al. [57]	Fe/Nb composite	
Flame spray pyrolysis		Guenin et al.[52]	L-Nb_2O_5	
Flame spray pyrolysis		Phanichphant et al. [58]	Nb-doped TiO2	
Flame spray pyrolysis		Teleki et al. [56]	Nb- and Cu-doped TiO2	

Method	Diagram	Reference	Material	Image
Flame spray pyrolysis		Kruefu et al. [60]	Nb doped ZnO	
Flame spray pyrolysis		Zanetti et al [55]	$SrBi_2Nb_2O_9$	
Combustion		Kachelmyer et al. [61]	$NbAl_3$	
Combustion		Tomasi & Munir [53]	Al_2O_3-ZrO_2-Nb	
Combustion		Shon et al. [54]	WSi_2-Nb	
Combustion		Yeh & Chen [59]	$(Ti_{1-x}Nbx)_2AlC$	
Combustion		Gedevanishvili & Munir [62]	Nb_5Si_3 and $NbSi_2$	

3-3- Synthesis of niobium oxide nanostructures in the flame

The same counter-flow flame reactor that was described in chapter 2 was employed for the niobium oxide experiments.

Niobium wires with a purity of ~99.99% (Sigma Aldrich Corporation) and a diameter of 1 mm were used as the source material. Wires were introduced radially in the flame parallel to the nozzles' planes. The Nb probes were inserted at two different heights of Z=12 mm and Z=13 mm. Z represents the distance between the fuel (top) nozzle and the center of the wire (figure 3-2a1). The Nb wire inside the probe holder was stabilized by two inserts, which are tip insert and inside insert. Both inserts have a hole through which the wire passes. The tip insert has a cap that prevents backward and forward movements of the wire. The inside insert keeps the wire in the center of the probe holder and prevents the wire from leaning towards the sides (see figure 3-2a2). The introduced wire in the counter-flow flame is affected by strong gradients of both temperature and chemical species (figure 3-2b). The temperature gradients reach ~2000 C/cm, and the chemical content changes rapidly from a hydrocarbon-rich zone on the fuel side to the oxygen-rich zone on the oxidizer side of the flame. Consequently, the probe position in the flame greatly impacts the synthesis processes. At Z=12 mm, the flame temperature is approximately 2500 ˚C and the oxygen content is 0.015 mole fraction. At Z=13 mm, the flame temperature is approximately 2400 ˚C and the oxygen content is 0.1 mole fraction.

Insertion time varies depending on the different stages of the experiment. However the longest insertion time was 70 seconds. A shorter insertion time assists in properly understanding the growth mechanism.
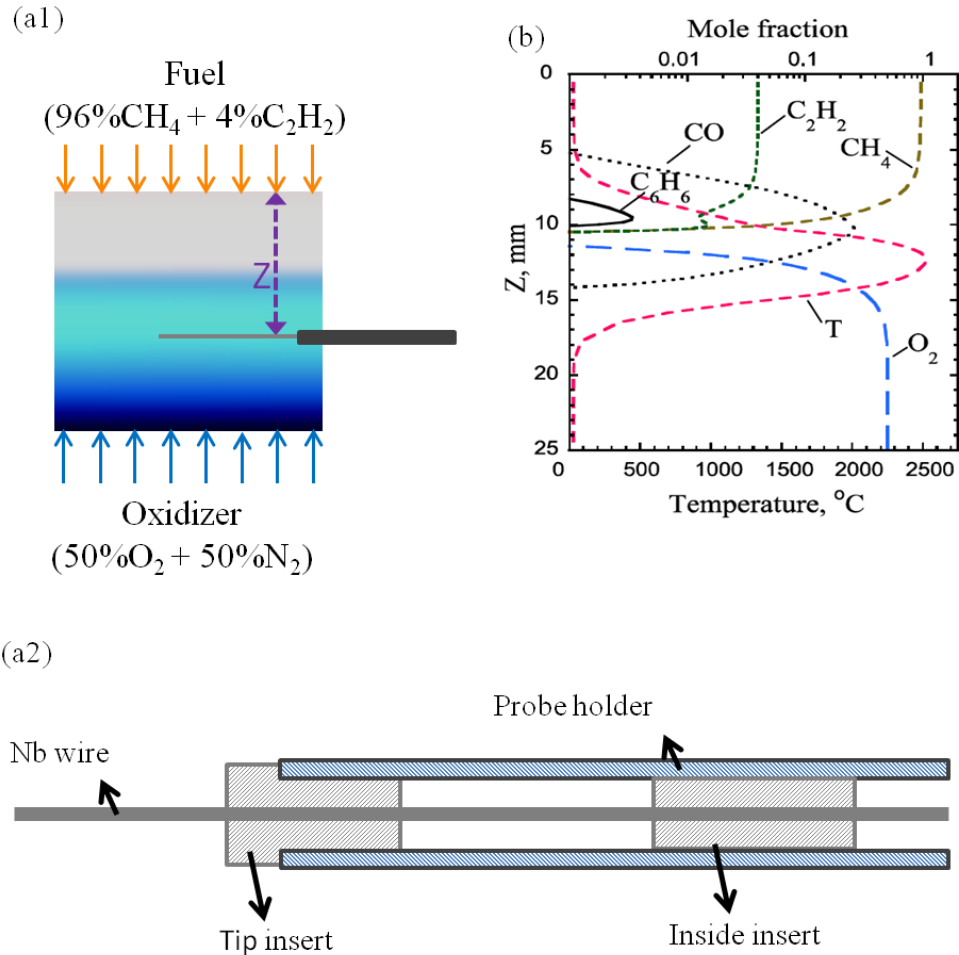
Figure 3-2- (a1) A photograph of the counter-flow flame along with a schematic showing the direct insertion of the niobium probe inside the oxidizer side of the flame for the synthesis; (a2) a schematic of probe holder and two inserts that keep the wire stable inside the flame; (b) profile of numerical predictions of temperature and major chemical species in the diffusion counter-flow flame as a function of the distance from the fuel nozzle (Z) [63].

3-4- Results and discussion

Just after the insertion of the probe inside the flame, a volume layer of material commences growing on the surface of the probe. The layer of material has a very

distinct white color. This layer initially appears on the oxidizer side where a higher oxygen concentration and oxygen free radicals are present. As the experiment continues, the layer expands to the sides and subsequently on the fuel side of the probe (figure 3-3). The layer has a higher thickness on the oxidizer side resembling a semi-oval covering the Nb probe.
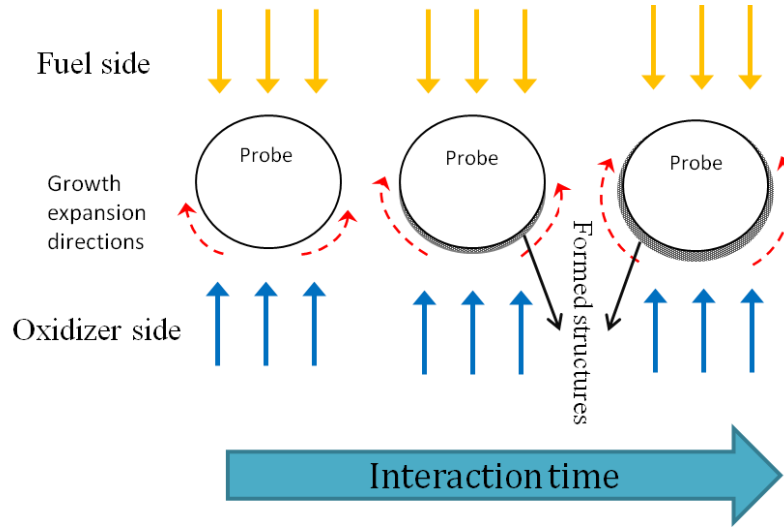
Figure 3-3- directions of growth expansion of the Nb oxide layer are shown by the dashed arrows.

3-4-1- Morphology of grown structures at different Z heights

The counter-flow flame is characterized by strong axial gradients of 2000 K/cm, consequently the probe position in the flame significantly affects the synthesis processes. Z represents the distance from the center of the probe to the edge of the fuel (top) nozzle.

3-4-2- Structures at Z height of 12 mm

Figure 3-4a depicts as-grown structures of niobium oxide formed on the fuel side surface of the probe (Z=12 mm) inserted in a flame volume for an interaction time of 70 seconds. The white solid arrow (figure 3-4b) points out an example of coalesced

microrods. High-resolution SEM shows that the coalesced rods are typically of the same height. The presence of non-coalesced microrods is evident as indicated by the white dotted arrow in figure 3-4b. The coexistence of non-coalesced and coalesced microrods suggests that individual rods grow continuously and coalesce to form the larger structures. The flame temperature at Z=12 mm is ~2500°C, which can cause the surface of the niobium oxide layer to consist of melted structures, as highlighted by the blue arrows in figure 3-4b. Figure 3-4c shows as-grown individual nanorods formed on the oxidizer side of the Nb probe at Z=12 mm for an interaction time of 70 seconds. The nanorods have diameters of ~50-200 nm with heights of more than 2 μm. The nanorods do not have uniform diameters and grow in different directions from the surface of the probe. In figure 3-4c the dashed arrows point out a typical nanorod with variable diameters along the central rod axial axis.

It is clear that some parts on the surface of the formed Nb oxide layer are covered with what appears to be melted materials. Melting of niobium oxide can be a possible reason for the appearance of such materials (black dotted arrow in figure 3-4b and c). Besides the high flame temperature, exothermic reactions might occur over the formed rods and thus increasing the temperature over the surface of the rods. Reactions such as radical recombination and surface quenching can contribute to an increase in the rods temperature [64, 65] and consequently the appearance of melted materials. Rise in the surface temperature due to surface reaction is well accepted [65, 66]. It is important to note that the material source for growth of the nanostructures is not supplied from the gas phase unlike in the vapor-liquid-solid (VLS) or gas-solid (VS) process. Here, the possibility that the metallic probe could form vapors is eliminated due to low electron

mobility and the high melting points of niobium (~2500˚C) and Nb oxides (NbO: 1940˚C, NbO_2:1900˚C, and Nb_2O_5:1520˚C). Instead, the rods grow by means of the basal attachment to the probe.
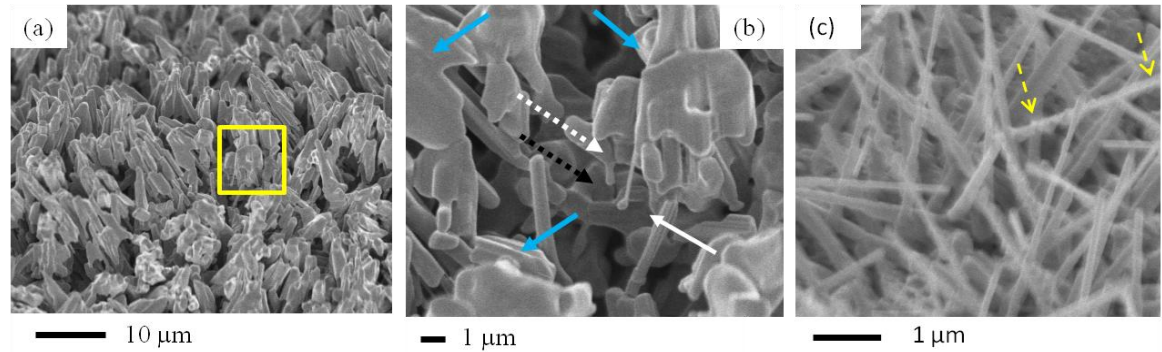
Figure 3-4- SEM images collected from the surface of the flame synthesized Nb oxide layer formed on the surface of Nb probes positioned at Z=12 mm. (a) Morphology of the oxide layer grown on the fuel side surface of the Nb probe inserted in the flame volume; (b) shows typical morphological details of the oxide layer from a selected area in (a); (c) mostly single nanorods are present on the oxidizer side of the Nb surface.

3-4-3- Structures at Z height of 13 mm

Coalesced and individual micro/nanorods grow on the surface of the probe inserted in the flame volume at Z=13 mm for an interaction time of 70 seconds (figure 3-5a and 5b). The rods have various diameters ranging from approximately 50 nm to 1 µm. A higher magnification image (figure 3-5b) shows that microrods (solid arrows) are formed by the coalescence of individual nanorods (dashed arrows). It is noteworthy that the diameters of the individual nanorods are similar to the rods present in the microbundles. Therefore, highly dense rods can coalesce and form bundle-like microrods.

Since the flame temperature at Z=13 mm is lower (~200˚C lower than Z=12 mm), no melted appearing material can be observed on the oxidizer side of the probe. However, the flame temperature and the oxygen concentrations are high enough for the

37

growth of highly dense structures on the oxidizer side surface of the probe. Moreover, structures grown at Z=13 mm have high aspect ratio which can be attributed to the higher oxygen concentration. On the fuel side surface of the probe, some melted-like material can still be observed. Arrows in figure 3-5c indicate melted-like structures grown at Z=13 mm (figure 3-5c). Mozetic and Cvelbar [44] found that growth of the Nb oxide depends on oxygen concentration atoms and that structures grown in low oxygen concentration are thicker in diameter. The same result, thicker rods at lower oxygen concentration, is found here in our study. Similarly, highly compact coalesced structures were previously reported by Sieber at al. in which niobium oxides formed on the metallic niobium after 10 min to 1 hour polarization [50].
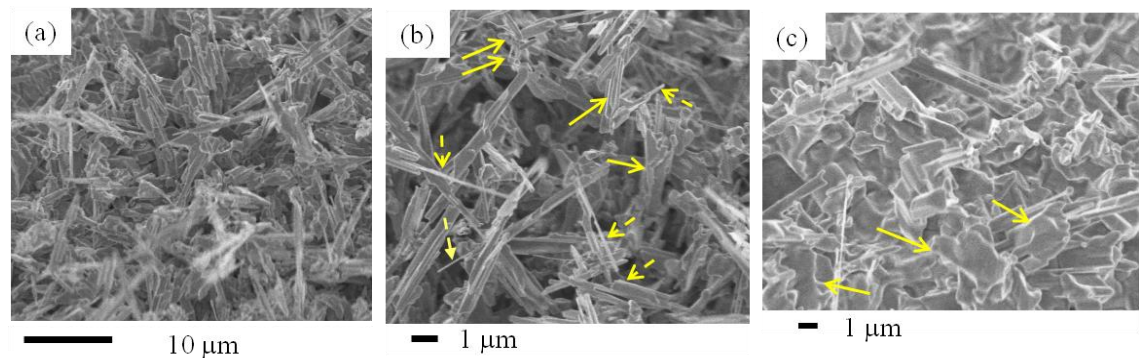
Figure 3-5- SEM image of grown structures at Z=13 mm; (a) morphology of the oxide layer formed on the oxidizer side surface of the probe; (b) high magnification of a selected area in (a); (c) structure grown on the fuel side surface of the probe.

3-4-4- Characterization of the grown structures

High resolution TEM, selected area electron diffraction pattern (SAED), Energy-dispersive X-ray spectroscopy (EDS), and X-ray diffraction analysis (XRD) were employed to characterize the structure and elemental composition of the flame rods. Figures 3-6a1 and 6a2 show TEM images of nanorods with diameters of ~250 nm and 120 nm, respectively. Nanorods have lengths of a few micrometers. The HR-TEM

images (figures 3-6b1 and 6b2) reveal highly crystallized structures and lattice fringes of 0.37nm and 0.35nm, which closely match with {110} and {$\bar{1}$12} plane spacing, respectively. A parallel pattern is repeated across the structure (figure 3-6b2), thus crystalline structures might be a polysynthetic twins crystal. Figures 3-6b1 and 6b2 reveal that the formed rods have no irregularity in crystalline structures and consequently, they are free of dislocations and crystalline defects. SAED images in figures 3-6c1 and 6c2 confirm that the rods are crystalline and have no crystalline defects. EDS analysis collected on the sample reveals that the nanorod structures are only composed of niobium and oxygen. Carbon and copper peaks are attributed to the TEM carbon gird. The grid is composed of copper with a thin carbon film on one side of the grid. Thus, the structures must be made of niobium and oxygen. EDS analysis cannot be used for elemental ratio (Nb/O) of the nanorods. Therefore, X-Ray Diffraction analysis (Rigaku Ultima IV) was used to identify the crystalline structures and elemental ratio of the products (figure 3-6e). The grown crystal structure closely correlates with α-Nb_2O_5 (PDF# 00-0371-1468) that has monoclinic structure. Bansal [67] reported that Nb_2O_5 heated over 1000˚C irreversibly transforms into monoclinic α-Nb_2O_5. In the same work, it was explained that α-Nb_2O_5 has a white color appearance, coinciding with the color in our products. During the experiments, no gas-phase formation and change in flame color were observed, thus establishing that neither niobium nor Nb oxides are transported by the gas flow of the flame. As it was discussed previously and reported in the literature [44, 64], due to the high melting point of niobium and its oxides, the possibility of VLS or VS are eliminated. Indeed, structures are formed at their initial positions. This behavior can be ascribed to the high melting

point of all common forms of the niobium oxides and the immobility of niobium at the flame temperature [44].
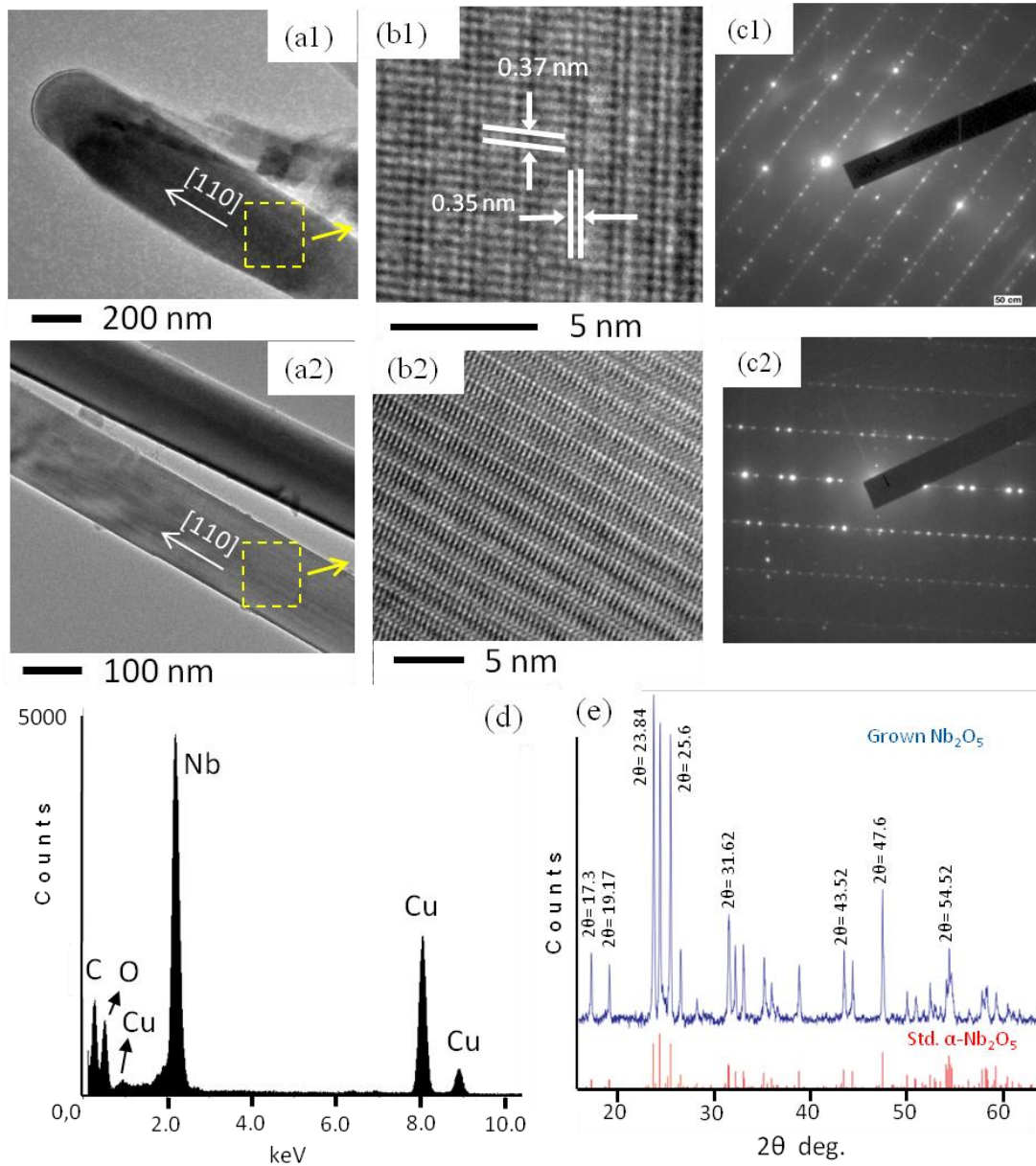
Figure 3-6- (a) TEM image of a typical rod forming the Nb oxide layer synthesized in the flame; (b) and (c) HR-TEM image and SAED of section of the rod in (a) reveals the structural uniformity and highly ordered crystalline structure. The measured lattice fringes of 0.35 and 0.37 nm closely match {110} and {$\bar{1}$12} plane spacing, respectively; (d) EDS spectrum of grown niobium oxide nanorods; (e) XRD spectrum of synthesized niobium oxide layer closely corresponding to α-Nb_2O_5.

Based on the previous studies, melting points of the transition metal oxides play a crucial role in the positions where structures grow/aggregate. Low melting points of TMOs augment the possibility of gas-phase formation and pave the way for the gas transportation of structures; however, high melting points of TMOs and/or transition metals increase the possibility of in-place formation. MoO_3 and WO_3 have melting points of ~795ºC and ~1475ºC, respectively. Studies have demonstrated that MoO_3 as well as WO_3 can be formed both on the surface of a probe and directly in the gas phase, but MoO_3 is more likely to evaporate and to be transferred by gas flow present near the surface of the probe [68-70]. However, niobium has low electron mobility which prevents the evaporation of niobium and leads to the formation of a niobium oxide layer over the surface of the source in the flame volume. Niobium oxides have high melting point temperatures that might hamper the gas-phase formation of structures.

The recorded distribution of grown materials on the surface of the probe suggests that material starts growing on the oxidizer side of the probe where gases (including O_2 and oxygen radicals e.g. atomic O) with higher oxygen concentrations are present, $[O]_1$. However, the fuel side of the probe interacts with lower oxygen concentration, $[O]_2$ (figure 3-2b). Due to the probe's interaction with higher oxygen content, rods on the oxidizer side grow at a higher growth rate in comparison to the fuel side. Consequently, the Nb_2O_5 structures form a semi-oval layer, thicker on the oxidizer side, surrounding the probe. The growth of the structures on the surface of the Nb probe was observed in all tested conditions. Morphologies of grown structures vary by the flame position (figure 3-4 and 5). Variation of TMO morphologies based on the probe flame positions and growth locations on the surface of probes were investigated by

previous studies and have been confirmed [68-70]. In this study, Nb_2O_5 rods grown on the oxidizer side have smaller diameters and a larger growth rate (figure 3-4 and 5); structures grown in a flame region closer to the flame front (Z height) have sharper tips (figure 3-5). Furthermore, structures grown at higher temperature (Z=12) show melted-like morphology. Figure 3-7b1 and 7b2 demonstrate the difference between melted-like structures and sharp tip structures grown at different temperatures. The temperature difference at Z=12 and 13 mm is 200 ˚C.
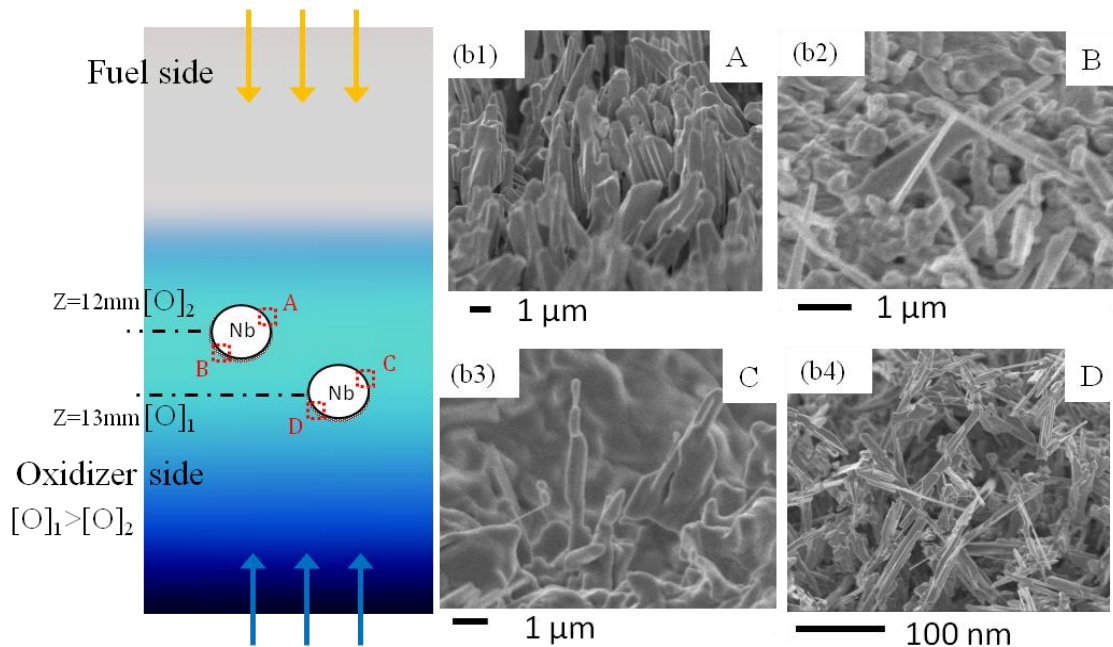
Figure 3-7- A schematic showing the growth characteristics of the Nb oxide layer on the surface of a Nb probe inserted in the flame volume;(b1 & b2) structures grown at Z=12 mm on the fuel side; (b3 & 4) structures grown at Z=13 mm on the oxidizer side.

Figure 3-8 shows the characteristic of the Nb-oxide layer growth around the surface of the probe. The grown structures are highly dense and connected in a way that the formed Nb_2O_5 layer can be easily removed from the bare niobium wire (figure 3-4a). The bulk of the structures maintain the shape of a semi-oval layer formed around the

probe. Structures grown on the other side of the layer are shown in figure 3-8a2. Structures have a height of 10 μm that protrudes on the other side of the white layer.
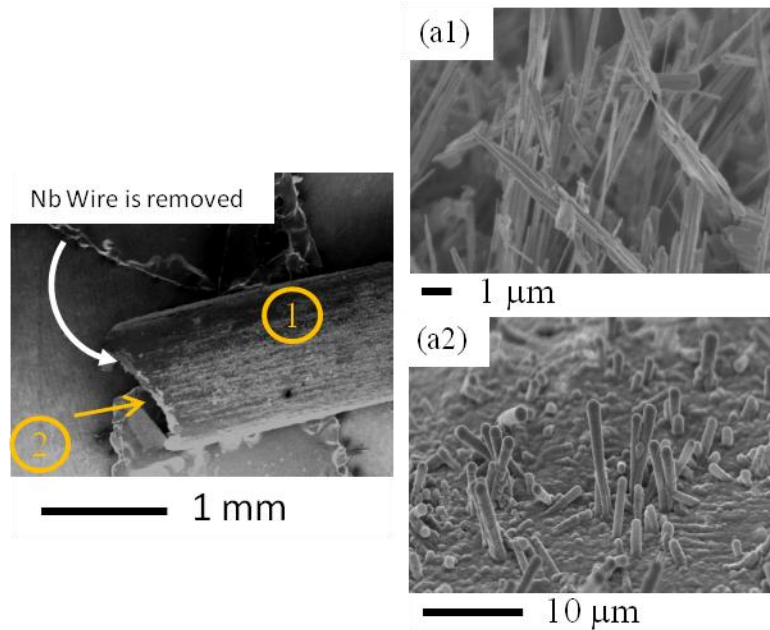
Figure 3-8- Represents an SEM image of the Nb-oxide layer after the Nb wire was removed (a1) structures grown on the outer surface; (a2) structures grown on the inner surface.

3-5- Growth mechanism

SEM images were collected on the surface of a niobium probe at various probe/flame interaction times in order to gain insight into the mechanism of the Nb oxide growth. The growth mechanism of the synthesis of the Nb oxide structures appears to involve several steps: 1) dissolution and diffusion of oxygen and oxygen radicals from the flame on the surface of the Nb probe forming a thin Nb oxide layer surrounding the surface of the probe; 2) nucleation of niobium oxide rods on the wire surface; 3) basal growth of nanorods; and 4) coalescence of nanorods which leads to formation of larger sized structures (bundles of nanorods). Figure 3-8 shows characteristic distributions of nanorod deposits on the surface of the Nb probe. The

43

probe with a diameter of 1 mm is inserted in the flame near the flame front (Z =12 mm) and exposed to the strong temperature gradients and variations of the chemical composition. Here oxygen flux is supplied from the formed flame and the only supply of a metal source is the niobium probe itself.

For an almost instant probe-flame interaction, a thin amorphous Nb oxide layer is already formed on the surface of the Nb probe (figure 3-9a). The metal oxide layer was formed by introducing a niobium probe in the oxygen-rich part of the flame for only a few seconds. The solids forming the layer have a white appearance, which is typical of Nb oxide powders.

The dissolution of oxygen leads to supersaturation of the surface due to the continuous flux of O atoms, as a result forming the amorphous oxide layer. As the probe/flame interaction time increases the supersaturation of the Nb surface, which causes spontaneous nucleation of niobium oxide crystals and crystallization of the amorphous layer (figure 3-9b). For this probe/flame interaction the probe remained exposed to the flame medium for ~5 seconds. A few rod-like structures protrude from the amorphous metal oxide layer. The rods have diameters of less than 100 nm and are less than a micrometer in length. Formations of an amorphous Nb oxide layer and its crystallization have been widely reported in the literature [64, 71, 72]. Consequently, the Nb oxide structures can grow due to constant flow of oxygen into the niobium metal and the surface. A significant change in the surface morphology of the grown layer is observed by increasing the probe-flame interaction time to 20 seconds (figure 3-9c). The density and size (diameter and length) of the Nb oxide structures significantly increase. The Nb oxide crystals grow at random directions by means of the basal

attachment of Nb and O (basal growth) in figure 3-9c. Arrows in figure 3-9c1 indicate some early coalesced rods that are protruded from the amorphous metal oxide layer. Figure 3-8c2 shows a close-up view of two rods that began to coalesce laterally.
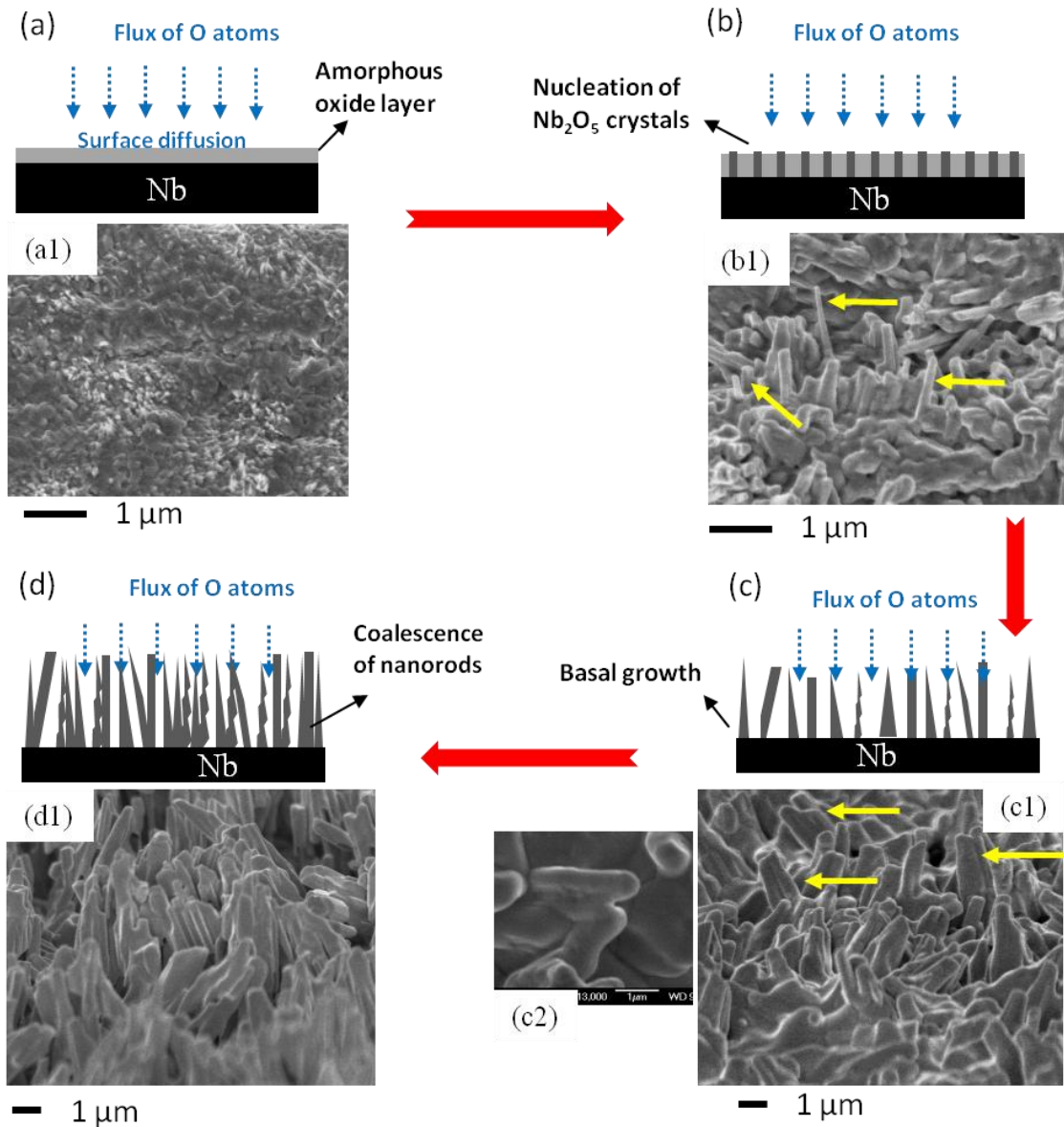
Figure 3-9- Collected SEM images on the surface of Nb probes after various probe-flame interaction times reveal the gradual formation and surface morphology of the Nb oxide layer. (a) It appears that for an almost instant probe-flame interaction (~ 2 sec.) a thin amorphous Nb oxide layer is already formed by diffusion and dissolution of atomic oxygen on surface of the Nb probe; (b) nucleation of Nb_2O_5 on the surface of the Nb probe (~5 sec.); (c) growth of Nb_2O_5 nuclei into nanorods due to base attachment of Nb and O (~20 sec.); (d) coalescence of the nanorods (~70 sec.). The probe is inserted at Z= 12 mm inside the flame.

As the exposure time of the probe-flame interaction was allowed to progress to 70 seconds, the morphology and physical characteristics of the Nb oxide layer significantly change (figure 3-9d). The Nb oxide layer is composed of a high density of structures that are closely packed. The length of the nano/micro rods is several micrometers. Close inspection in figure 3-9c2 shows that the nanorods are initially formed, then the adjacent nanorods become stuck together and form coalesced microstructures. The synthesis of niobium oxide at the flame's high temperature leads to transformation of all polymorphs to α-Nb_2O_5. A similar growth process was observed in cold plasma treatment using a high neutral oxygen flux [44].

3-6- Chapter conclusions

Niobium pentoxide has a variety of applications; therefore synthesis methods with a higher growth rate are required to respond to the demand. The flame synthesis method discussed in this chapter provides the fastest growth rate. A counter-flow flame is utilized for the rapid synthesis of the α-Nb_2O_5 nano/micro-sized structures. Niobium wires, with a diameter of 1 mm and a purity of ~99.99%, were inserted in the flame parallel to the nozzles' planes. The introduction of a niobium probe inside the flame volume results in the formation of an oxide layer (white colored) coating the surface of the probe. The surface morphology of the oxide layer strongly depends on the flame position. At Z=12 mm the Nb oxide layer is composed of coalesced microrods with a diameter of ~1μm. At Z=13 mm metal oxide layers composed of individual and coalesced micro/nanorods with diameters ranging from 50 nm to 1μm were formed. XRD analysis shows that the structures forming the oxide layer are composed of α-Nb_2O_5 with the monoclinic structure. The study of the characteristics of the deposits

suggests that the structures initially start growing on the oxidizer side of the wire where higher oxygen concentration is present. As the probe-flame interaction increases, the grown structures become highly dense and form a semi-oval layer around the surface of the Nb wire. The growth mechanism proposes that crystallization consists of four steps: 1) dissolution and diffusion of oxygen from oxidizer into niobium; 2) nucleation of niobium oxide on the wire surface; 3) basal growth of nanorods; and 4) coalescence of nanorods which leads to the formation of larger sized structures (bundles of nanorods).

Counter-Flow Flame Synthesis of Zinc Oxide Nanostructures[2]

4-1- Introduction

Because of the distinguished performance of ZnO nanostructures in electronic devices, they have received wide attention. Also, transparent conducting and piezoelectric properties of ZnO provide a unique position for ZnO among other semiconductors. These properties make it ideal for applications in flat panel displays and thin film layers in solar cells [73, 74]. Also, structures of ZnO have been considered as important components for applications of photocatalysts [75], gas sensors [76], ultraviolet (UV) light-emitting diodes (LED) and UV lasing [77, 78], field emission devices [79], and biological probes [80]. These notable physical properties motivate researchers to synthesize, characterize and test properties of ZnO nanomaterials. ZnO nanostructures can be produced in a wide range of morphologies by a variety of synthesis methods. Various applications of ZnO nanostructure are shown in figure 4-1. Different applications require different properties. Properties of ZnO are discussed in the following.

Mechanical behavior of nanostructures cannot be measured by traditional methods. In an experiment, a special TEM holder was prepared to hold ZnO nanobelts and their bending modulus was measured by an electric-field- resonant using TEM [81]. One-dimensional ZnO nanostructures prove to be a promising tool as a nanocantilever. A nanocantilever is simplest micro-electro-mechanical system (MEMS) that is a perfect

---

[2] The content of this chapter is an extension of a published paper of the author. The paper contains results of research which was solely conducted as partial fulfillment for the PhD requirement. Materials presented in the paper have not been submitted for a course or extra credit.

device for detecting very small forces and masses due to sensitivity to extremely small displacements. The sensitivity is improved compared to a conventional cantilever [82].

Both thin film and bulk of ZnO are considered as one of the main materials for gas sensor, for CO [83], O_2 [84], alcohol [85] and H_2 [86]. Nanowires and nanorods of ZnO, have superior gas sensitivity compared to thin film ZnO [87].

It is shown that exciton binding energy can be enhanced in quantum size scale [88]. Another application of ZnO nanorods is in optoelectronic circuits, because of oxygen vacancy in ZnO, a green-yellow emission can be observed. Investigations show that with increasing surface-to-volume ratio the green-yellow emission intensity increases [89].

Electrical transport of measured 1-D ZnO nanostructures is presented in the references. It is shown that, due to zinc interstitials and oxygen vacancies, 1-D ZnO nanostructures show a n-type semiconductor characteristic [90, 91].
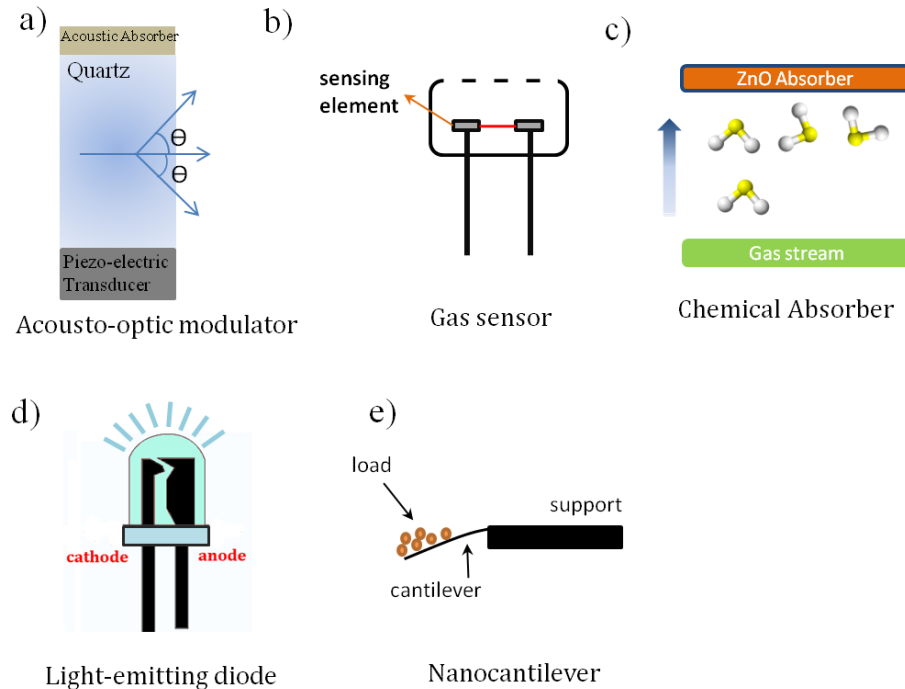
Figure 4-1- Typical applications of ZnO nano/micro structures.

49

4-2- Current synthesis methods of zinc oxide nanostructures

Due to wide applications of ZnO at the present time, a variety of 1D and 3D nanostructured ZnO crystals have been formed such as nanorods [92, 93], nanowires [94], nanowhiskers [95], nanobelts (nanoribbons) [96], nanospings [97], nanocombs [98], nanowalls [99], nanobridges [100], nanonails [101], nanohelices [102], and hierarchical nanostructures [103]. The richest family of nanostructures, both in properties and morphology, belongs to ZnO nanostructures. Various techniques have been developed for the preparation of ZnO nanostructures, including vapor-phase transport [104], chemical vapor deposition (CVD) [105], plasma enhanced CVD [106], reactive magnetic sputtering [107], spray pyrolysis [108, 109], and sol-gel techniques [110], among others. Although these methods are capable of producing ZnO structures, they are generally limited by the complexity of the process, scalability and purity of the products. Some of these methods are composed of a multi-step process, which is time consuming and expensive.

Table 4-1 lists different methods that are employed to synthesize zinc-oxide nano/micro structures.

Table 4-1- List of different employed methods to grow ZnO nano/micro structures.

Method	Experimental configuration	Author(s)	Morphology of structures (schematic)
Vapor Trapping CVD		Chang et al. [105]	
CVD		Saitoh et al. [111]	
Sol-gel		Znaidi et al. [112]	
Plasma Enhanced CVD		Yang et al. [106]	
Heat treatment		Zhang et al. [113]	
Hydro-thermal		Qiu et al. [17]	

4-2-1- Combustion and flame synthesis methods

Zinc oxide nano/microstructures are also synthesized through different combustion and flame methods. Regarding different flame and combustion methods please refer to section 1-5 and 1-6 in chapter one. A summary of combustion and flame methods is tabulated in table 2-4. This section focuses on combustion and flame methods with a brief description of approaches.

Tani el al. (2002) [114] synthesized zinc oxide (ZnO) nanoparticles by FSP of zinc acrylate-methanol-acetic acid solution. They examined the effect of solution feed rate on crystalline size and particle surface area. Their results show that a higher solution feed rate leads to higher flame height, coalescence and surface growth. The synthesized particles were collected by a vacuum pump on a glass fiber filter. The grown powder has the smallest particles with highly homogeneous diameter, compared to ZnO powder produced through other methods. Also, by increasing feed rate by a factor of 4, the primary ZnO particle diameter increased from 10 to 20 nm.

Kruefu et al. (2010) [60] employed FSP to synthesize pure ZnO and Nb-doped ZnO. They sprayed precursor solutions of $2(C_{11}H_7O_2)Zn$ (zinc naphthenate) and $Nb_2(OC_2H_5)_{10}$ (niobium ethoxide) in toluene/methanol. They were able to produce crystalline and nanostructured particles. A vacuum pump was used to collect the Nb-doped ZnO nanopowders on glass microfiber filters. The grown ZnO nanoparticles have morphology of sphere and nanorod structures. The diameters of grown ZnO hexagonal and spherical particles were 5 to 20 nm. Grown ZnO nanorods had widths of 5-20 nm and lengths of 20-40 nm.

Xu el al. (2007) [115] synthesized ZnO nanowires on zinc-plated-steel substrates at large growth rates of microns per minute without catalysts. An inverse diffusion co-flow flame was employed to carry out the synthesis. A zinc-plated-steel source was introduced radially inside the flame medium at different heights, which provide different temperatures and chemical species. They found out the morphology of the nanostructures depends on temperature and chemical species contents such as O_2 and H_2. They synthesized different structures of ZnO such as nanowires, short nanorods, nanoribbon, and nanocones. Nanowires with diameters larger than 100 nm with hexagonal-cross-section are produced at higher temperatures. Nanowires with diameters of 25-40 nm are grown at lower temperatures.

Kathirvel el al. (2013) [116] synthesized highly crystalline ZnO nanorods by a simple flame synthesis technique. Materials are collected 25 cm above the flame on a plate. Results shows that particles have irregular shapes in sizes of 40 to 50 μm and also grown nanorods have a hexagonal cross section in diameters of 31.7 to 53.5 nm. They produced wurtzite ZnO nanorods structures, which show interstitial vacancy of zinc in their photoluminescence spectrum. Also, grown-ZnO nanorods exhibit ferromagnetic and gas sensing characteristics because of the oxygen deficiency

Tarwal et al. (2011) [117] synthesized ZnO nanopowder by a combustion method. They used precursor and fuel of zinc nitrate and glycine, respectively. The initial precursor and fuel were prepared at room temperature. The ZnO powder was formed in a high pressure and temperature combustion within a few minutes. The results show that ZnO have a size of 25 nm and sharp ultraviolet emission at room temperature indicating a proper optical characteristic.

Table 4-2 lists different flame/combustion methods that are employed to synthesize zinc oxide nano/microstructures.

Table 4-2- List of different combustion and flame methods to synthesize ZnO nano/micro-sized structures.

Method	Experimental configuration	Authors	Fuel/ precursor	Morphology of structures (schematic)
Flame spray pyrolysis		Tani el al. [114]	Zinc acrylate-methanol-acetic acid	
Flame synthesis		Kathirvel el al. [116]	Acetylene	
Flame spray pyrolysis		Kruefu et al. [60]	$2(C_{11}H_7O_2)Zn$ & $Nb_2(OC_2H_5)_{10}$ in toluene/ methanol	
Co-flow flame synthesis		Xu el al. [115]	Methane	
Combustion		Tarwal et al. [117]	Glycine	

4-3- Synthesis of zinc oxide nanostructures in the flame

The same counter-flow flame reactor that was explained in chapter 2 is employed for zinc oxide experiment.

Zinc wires, with a purity of ~99.99% and diameter of 1 mm, were used as the source material. Due to the low melting point of Zn (~ 419°C) the probe was sequestered inside a sleeve in order to protect it from the high temperature zone of the flame (figure 4-1a). An insert containing a window opening at its center was inserted at the tip of the sleeve, which was exposed to the flame medium. The insert and sleeve were placed in the flame so that the gas flows perpendicular relative to the position of the Zn probe (figure 4-1b1). The probe and sleeve were introduced radially at various flame heights (Z). Z represents the distance from the edge of the fuel nozzle to the center diameter of the sleeve opening (figure 4-1a). An inside insert was used inside the sleeve to keep the wire in the sleeve. The wire was placed inside the sleeve in a position that the tip of the wire was 3 mm away from the tip of the sleeve (figure 4-1b2). The flame height was used in our experiments as a means to control the growth of the nanostructures. It is evident from figure 4-1c that at various Z heights, the flame temperature and chemical species vary significantly within the flame [118]. Scanning electron microscopy (SEM), transmission electron microscopy (TEM), high resolution TEM (HR-TEM), X-ray energy dispersive spectroscopy (EDS), and selected area electron diffraction pattern (SAED) were used to characterize the chemical composition and structure of the sampled materials.
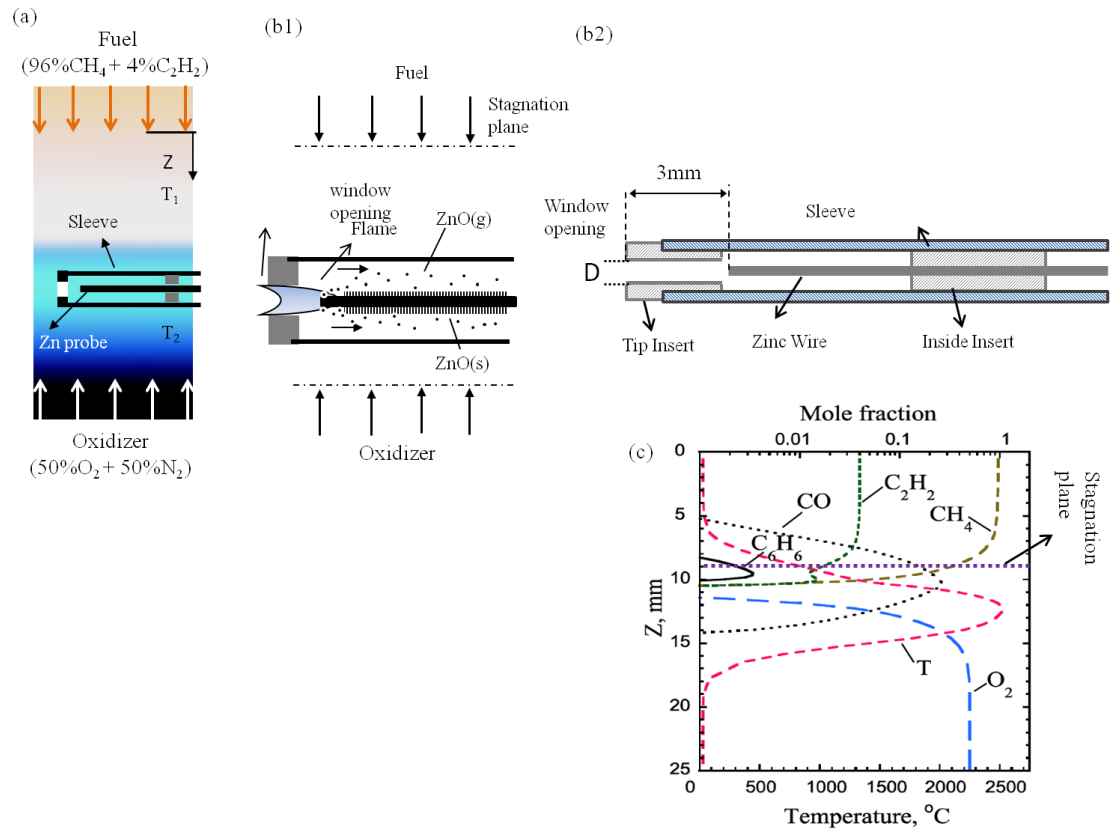
Figure 4-2- (a) a schematic image of sleeve and Zn probe inside the flame volume; (b1) a schematic image of flame penetration through the sleeve and formed structures over the zinc wire; (b2) a schematic drawing of sleeve and two insert that keep the wire stable inside the flame; (c) profile of numerical predictions of temperature and major chemical species in the diffusion counter-flow flame as a function of the distance from the fuel nozzle (Z) [63].

4-4- Result and discussion

Figure 4-3 represents SEM images of as-grown nanomaterials deposited on the surface of a Zn probe inserted in the flame volume at the flame height of 12 mm for 2 minutes residence time. It is evident that a high density of nanostructures can be grown on the surface of the probe. It was also observed that the bases of the structures have a larger diameter than the tips. The diameter of the rods is less than 100 nm and length of them is several microns. Grown rods have an approximate length-to-diameter aspect ratio of 10 to 30 with a growth rate of 8 to 17nm/s. Scanning of the probe with SEM

56

showed that the entire probe is covered with 1-D nanocrystals. Figure 4-3b and c

represent SEM images showing a close up view of the selected areas in figure 4-3a. The

structures were synthesized using a sleeve with a window opening of 2 mm in diameter.
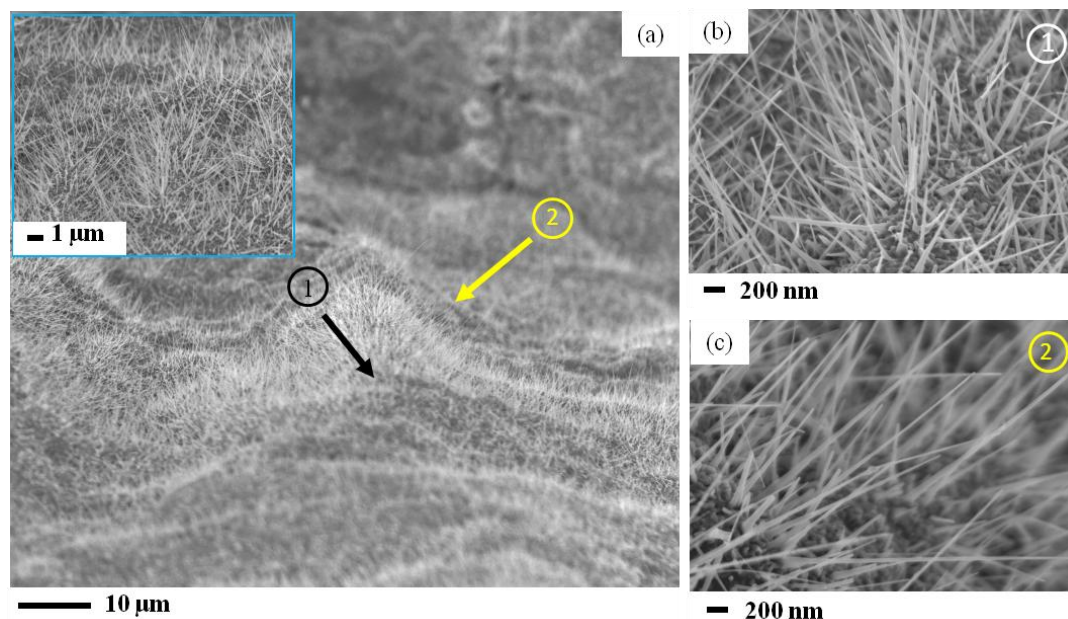
Figure 4-3- SEM images of zinc oxide nanorods formed on the surface of the zinc probe; (a) low resolution SEM showing the high density growth of nanorods; (b-c) high resolution SEM images of selected areas in (1) and (2) in (a). The Zn probe is inserted in the flame medium at Z= 12 mm with a 2 mm opening size sleeve.
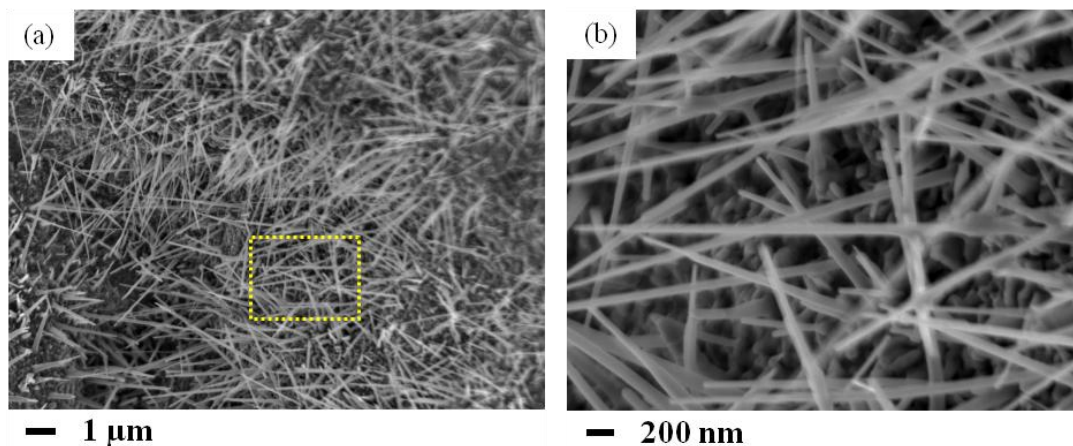
Figure 4-4- SEM images of zinc oxide nanorods formed on the surface of the zinc probe at Z=12 and 2.5 mm opening; (a) low resolution SEM showing the high density growth of nanorods; (b) high resolution SEM images of selected areas in (a).

Figure 4-4 represents nanorods grown at Z=12 mm and size opening of 2.5 mm. It is clear that by altering the size opening 2.5 mm, the morphology of grown structures does not significantly change. Nanorods are grown in high density and possess a high length-to-diameter aspect ratio and sharper tips than the base.
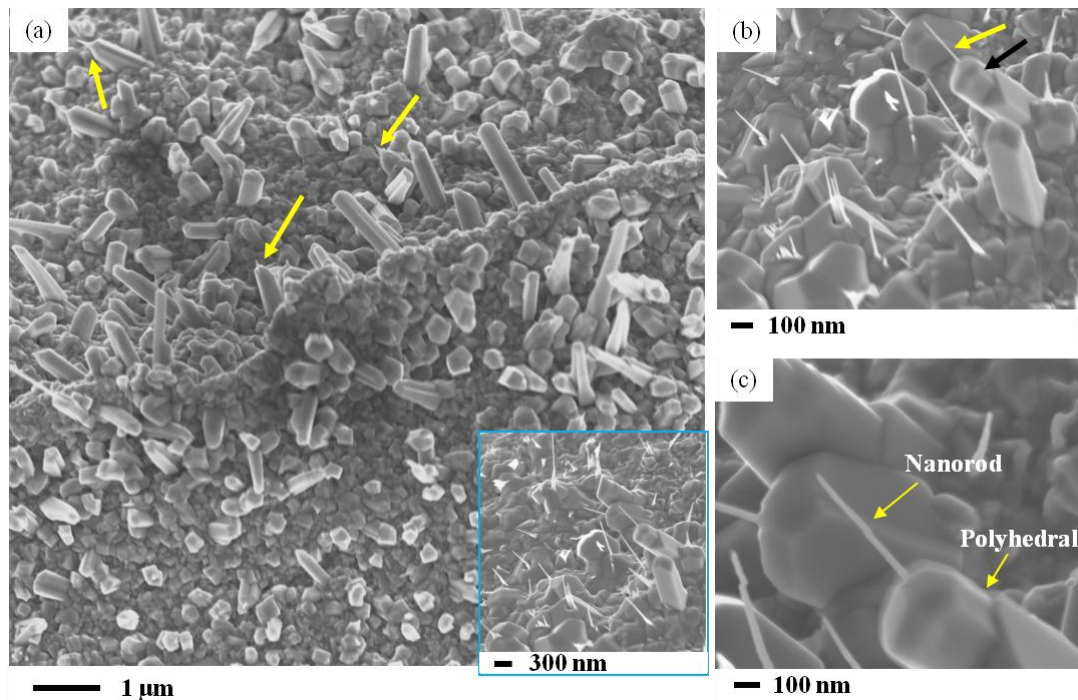
Figure 4-5- SEM images of structures formed on the surface of the Zn probe inserted in the flame medium at Z= 11 mm with a 2 mm sleeve opening size; (a) Shows that a high density of crystal structures can be synthesized; (b) High resolution SEM image of a selected area in (a) shows that the larger polyhedral crystals have a protruding nanorod at their tips; (c) a close-up view show that the larger crystals have a high number of facets with their edges well defined.

In this study we found that by altering the position of the probe, different types of structures can be grown due to the significant changes in the temperature and the content of oxygen near the surface of the probe. The repositioning of the probe to Z=11 mm (with an opening of 2 mm) resulted in larger polyhedral crystals on the surface of the probe (figure 4-5). In the literature, large ZnO polyhedral crystals similar to the ones observed here are called ZnO microprism (ZMP) [119]. The ZMPs can have a large

number of facets with rectangular, pentagonal, and hexagonal cross-sectional areas, Schematics of ZMPs are shown in figure 4-6.
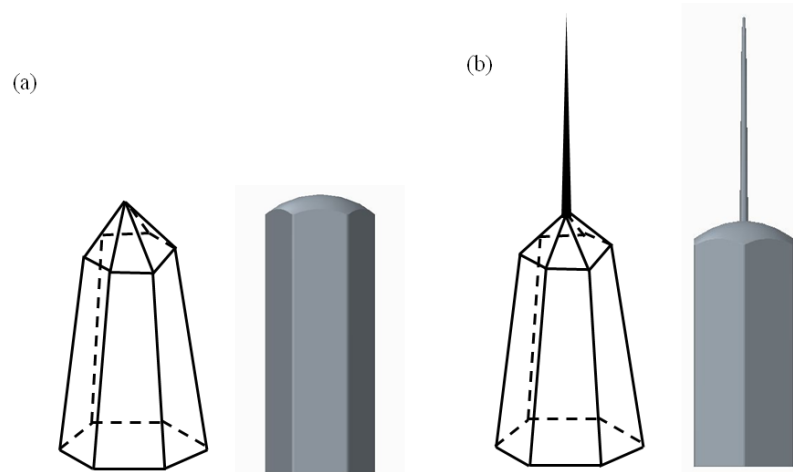
Figure 4-6- Schematic of ZnO microprism;(a) ZMP without a nanorod at the tip; (b) ZMP with a nanorod at the tip.

High resolution SEM reveals that the ZMPs have a protruding nanorod at their tips (white arrows figure 4-5a and b) creating a needle-like structure. The protruding nanorods at the top of the ZMP crystals have diameters less than 100 nm and are several hundreds of nanometers in length. It is interesting to note that the protruding nanorods have similar morphological characteristics to the structures grown in the lower part of the flame (Z=12 mm), figure 4-4. That is, they have a nanoscale diameter and the sharp tip suggesting that these structures grow in a similar manner. Similar to the previous testing position, the protective sleeve assures that the probe is not instantly oxidized and consumed in the flame medium. The counter-flow flame has a strong axial temperature (up to 2000˚C/cm) and chemical composition gradients. At the flame position of Z=11 mm the flame temperature is predicted to be ~2100 ˚C compared to ~2500 ˚C at Z=12 mm. The flame environment at the flame height of Z= 12 mm contains higher oxygen (or oxygen radical) content compared to no oxygen (or oxygen radical) at the flame

position of Z=10.5 mm (figure 4-2c). Thus, the position of the probe/sleeve can significantly affect the results of the nanomaterial synthesis. The effect of temperature and oxygen on the flame synthesis of ZnO nanostructures correlates well with other complex thermal methods where it is shown that both temperature and oxygen content can greatly affect morphology and size of ZnO structures [105, 120-123]. Grown nanorods on the tip of the ZMP crystals have length-to-diameter aspect ratios in the range of 2 to 8, and have a growth rate of 5 to 15nm/s.

For TEM studies, samples were prepared by suspending the removed synthesized structures in methanol. The solutions were sonicated until the material was well dispersed in the solvent. A drop of the suspension was then placed on a copper substrate/carbon-film of a TEM grid and dried. HR-TEM and SAED imaging of the grown structures reveal the structural uniformity and highly ordered crystalline structure as shown in figure 4-7. Figure 4-7a represents a TEM image of a nanarod in which its diameter appears to gradually taper at its tip to the shape of a pipet-like structure. Also, a very similar nanorod is shown in figure 4-7b. A TEM image of a ZMP is shown in figure 4-7c. TEM and HR-TEM reveal that the structures possess a high degree of perfection (without defect or dislocation) and grow in [001] direction. Figure 4-7c represents the atomic resolution of a typical nanorod (from the circled area in figure 4-7b). The lattice fringes from TEM studies correspond to a d-spacing of approximately 0.26 nm that closely matches the (002) plane of the hexagonal ZnO (Wurtzite) cell. The work of Li et al. showed that the [001] direction is the preferred growth direction of ZnO and it grows at much faster rates than the facet sides [124]. Once the facets appear, they do not disappear; crystal faces with this behavior cause the gradual reduction in

cross-sectional area along the growth direction and hence yield the sharp tip morphology. Since no catalyst was employed in the experiments and also no condensate structures such as droplets can be observed in SEM and/or TEM images, the growth mechanism of ZnO nanostructures can be explained through the vapor-solid (VS) mechanism. As for the VS mechanism, it is very typical that the nanorods or nanowires reduce gradually in diameter during growth and possess a sharp tip [125, 126].
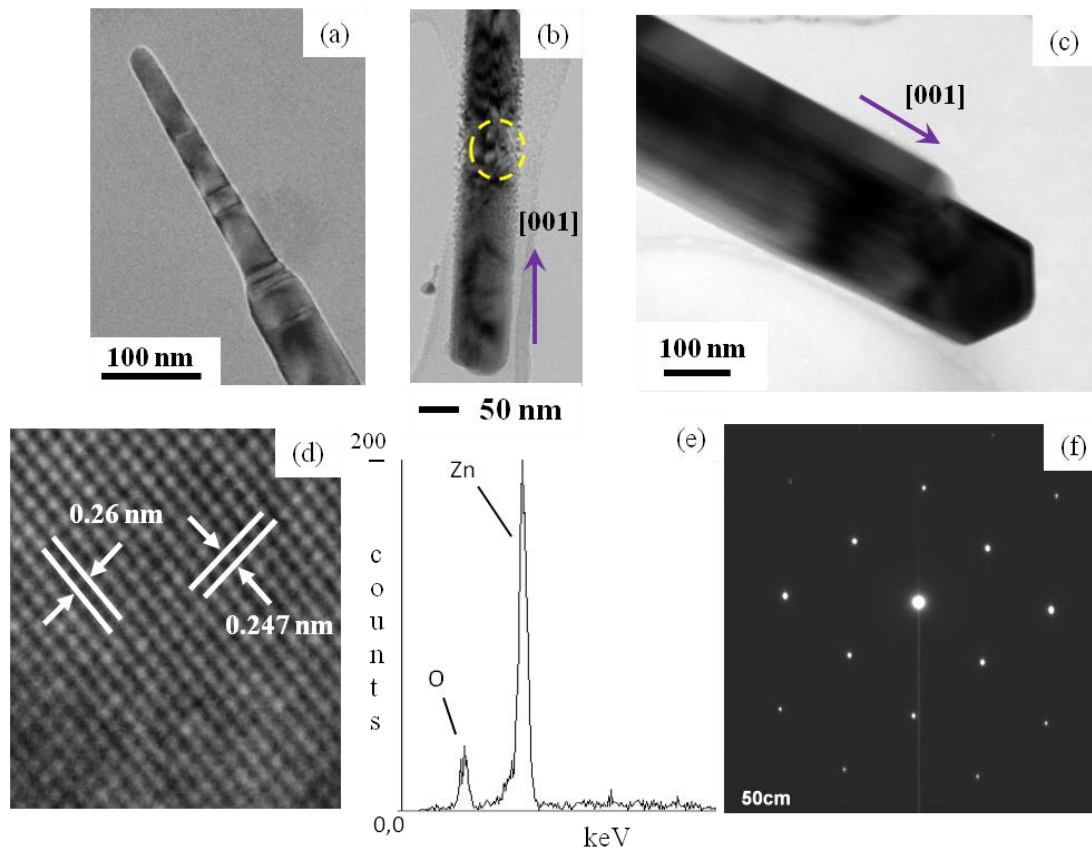
Figure 4-7- Structural and chemical composition analysis of the Zn oxide crystals formed in the flame medium; (a) TEM image of a nanorod with its tip gradually decreasing into a pipet-like structure; (b) and (c) low resolution TEM image of a Zn oxide nanorod; (d) HR-TEM image of the same nano-rod (circled area in b) showing a well-ordered crystal structure with characteristic d-spacing corresponding to {002} planes; (e) EDS spectrum collected on the structure shows the presence of Zn and oxygen (f) SAED with diffraction spots confirming the crystallinity of the structure.

HR-TEM imaging of a typical nanorod at different points shows that they are free of dislocations and structural defects. The HR-TEM analysis and SAED diffraction

pattern with the diffraction spots confirms the crystallinity of the structure. X-ray energy dispersive spectroscopy (EDS) conducted on the synthesized structures revealed that the structures are indeed composed of zinc and oxygen (figure 4-7d).

4-5- Growth mechanism

Figure 4-7 represents TEM and SEM images of grown crystals at the earlier, intermediate, and final stages. We propose that the growth mechanism is composed of two different processes: 1) the global growth mechanism is responsible for the formation of vapors by the evaporation of the base metal as it is partially exposed to the flame medium. The Zn atoms are intercalated with oxygen atoms from the flame to form ZnO nuclei. 2) Once the nuclei are formed, elongated structures start to form through the vapor-solid (VS) growth mechanism. For the first step, the mechanism involves a partial interaction of a high purity Zn probe in the form of a 1-mm diameter wire with a high temperature flame rich in oxygen and oxygen radicals. It is important to note that the temperature of the 1-mm diameter probe is much higher closer to the tip of the sleeve where the flame-probe interaction takes place. Consequently, a high rate of zinc vapor is produced due to the low melting point of Zn which is ~420°C. As the process continues, Zn atoms combine with oxygen atoms from the flame to form ZnO. The Zn oxide is deposited on the surface of the probe and can act as a nuclei to form elongated structures. A continuous influx of ZnO vapors can be further deposited on previously formed rods to further crystallize complex 1D or 3D structures. A recent work by Li et al. [124] reports the formation of ZnO micro- and nano-structures prepared by thermal evaporation that very closely resemble our flame synthesized ZnO structures reported here. In that study, the structures are grown in a tube chamber

operating at ~1000°C with varying oxygen percentages. It is proposed that at the applied temperature condition Zn vapors are mass-produced from the Zn source material and later combine with the oxygen atoms in the gas-phase to form ZnO nuclei.

In previous works on synthesis of TMO nanostructures, it was shown that metal oxides are first formed on the side of the base probe located in the higher temperature of the flame [70, 127]. These oxides are further evaporated and transported by the gas flow to the lower temperature side of the probe where they are deposited in the form of TMO nanostructures. In the Zn oxide case, the melting and boiling point temperature of ZnO is ~1975 °C and 2360 °C, respectively. Therefore, our experimental results suggest that the Zn in the vapor phase must combine with oxygen atoms and deposit along the surface of the probe to serve as nuclei and source material for the continuous growth of the ZnO structures. The density of metal and metal/oxide vapor and consequently the nuclei can be controlled by a simple relocation of the probe within the flame. A higher environment temperature results in a higher Zn vapor formation, thus higher density nuclei. Experiments conducted in vapor phase transport using Au-catalyzed Si substrates for the synthesis of ZnO nanostructures have shown that a wide variation in morphology of the synthesized structures can be obtained by a small variation of temperature [125]. The effect of variation of temperature for the growth of the Zn oxide structures is also very evident in our flame synthesis method. At Z=12 mm, the local flame temperature generated by the counter-flow reactor is higher than that at Z=11 mm by ~400 °C. In our experiments, we observed that the higher temperature (Z=12 mm) results in growth of ZnO nanorods. However, at the lower temperature (Z=11 mm),

ZMPs with facets and a nanorod extruding from the tip grow on the surface of the probe.
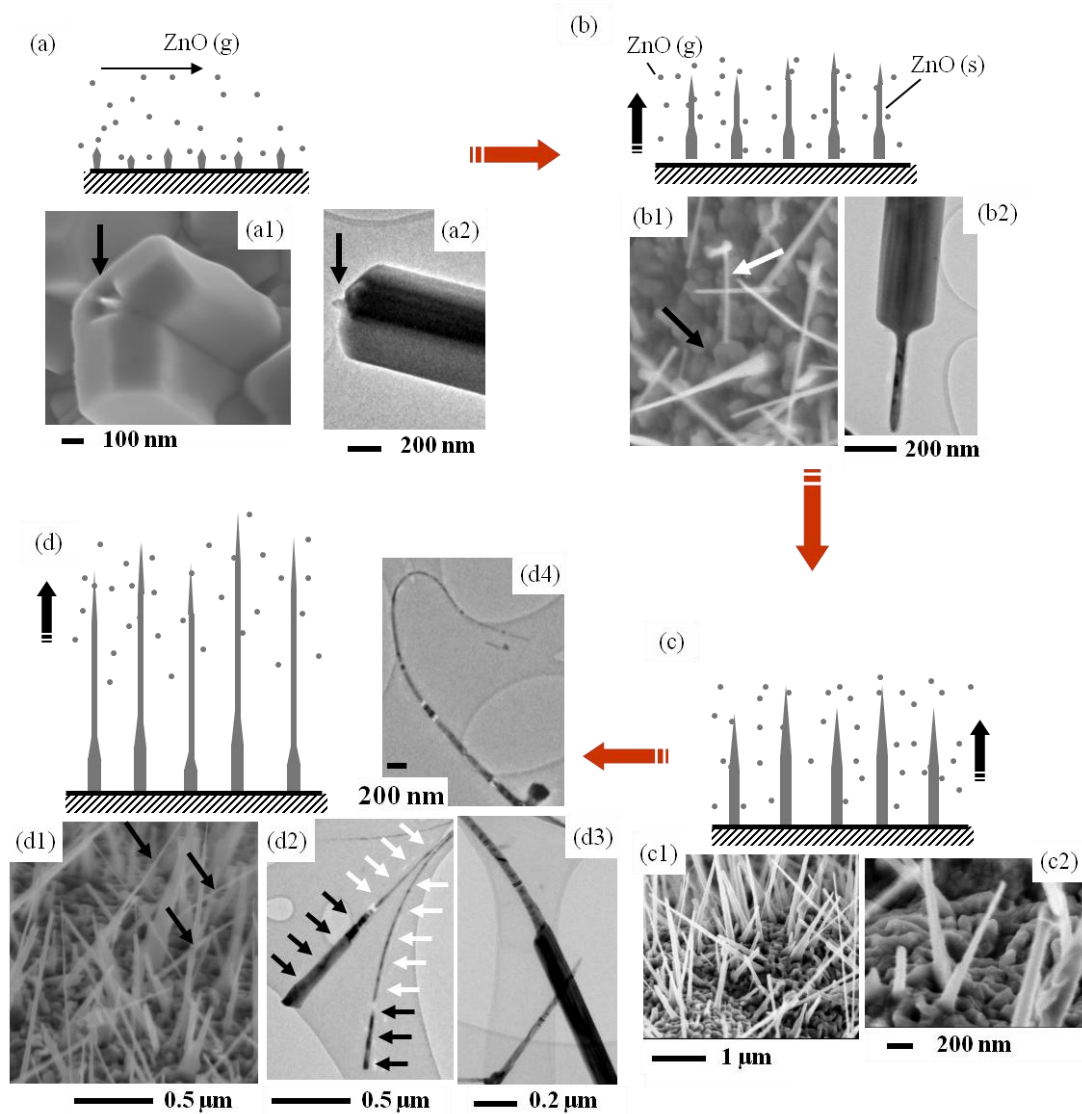
Figure 4-8- Proposed growth mechanism of ZnO nanostructures.

It is important to note that the temperature of the 1-mm probe used for Zn-oxide nanostructure synthesis is always lower than the local flame temperature due to the radiant and conductive heat losses.

A probe inserted in the flame volume at Z= 11 mm results in lower Zn vapor supersaturation, which leads to the formation of ZnO microprism (ZMP) crystals with high numbers of facets and sharp tips. Our results show that ZMP crystals with a few micrometers in length are first formed on the surface of the Zn probes. SEM images also show that the tips of the ZMP crystals have a structural defect in the form of a nanometer sized hole (figure 4-8a1). The hole constitutes an instable site that is ideal for a second nucleation process [124]. As the growth proceeds, the probe is consumed and the diameter of the probe reduces. Consequently, the temperature of the probe increases, leading to a higher vapor supersaturation and to a level that favors the synthesis of 1D nanorods of high crystallinity extruding from the tip of the ZMP crystals. The black arrow in figure 4-8a1 points to the nanosized hole or indentation at the tip of a ZMP crystal, revealing the early stage growth of nanorods (second nucleation). TEM analysis confirms that the nanorod emerging from the indentation (as observed by SEM) is indeed a part of the larger crystal, figure 4-8a2. That is, after sonication of the crystals in methanol, the nanorod remained at the tip of the ZMP. It is not clear what activates the growth of the nanorods on the tip of the ZMPs, but it appears that the nanosized hole on the tip of the ZMP crystal serves as an auto-catalyst similar to the VLS growth model.

Once the nucleation of the nanorod is initiated it continues to grow in a preferential direction away from the tip of the ZMP crystal. A close inspection of the SEM image (figure 4-8b1) reveals that the size of the ZMP crystals remained the same (black arrow) but the length of the protruding rods at the tips of the crystals significantly increased, as indicated by the white arrows. The protruding rods are of an

aspect ratio resembling solid pipet-like structures. The TEM image in figure 4-8b2 clearly shows that both the base and tip form a single crystal. The pipet-like structures are modified to needle-like nanorods due to the continuous deposition on their surfaces of ZnO species, figure 4-8c. A close inspection shows that the cross-sectional area at the base of the pipet-like structures (figure 4-8b1 and c2) coincides with the base of the needle-like structures (figure 4-8c1 and c2). Further deposition of the ZnO vapors on the surface of existing structures results in the transformation of structures, figure 4-8d. The SEM image in figure 4-8d1 shows structures with larger bases and pointy tips as highlighted by black arrows. The nanorods have lengths of several microns and a gradual reduction in diameter. They also appear to be flexible, for instance, the structure in the inset in figure 4-8d1 has a "U" shape curve/bend at its tip which shows that some of the ZnO structures can have very small bending radius. The black arrows in figure 4-8d2 highlight needle-like structures and the white arrows highlight nanorods protruding from the tips of the needle-like structures. Figure 4-8d3 is a close up view of a selected area in figure 4-8d2 highlighting the transformation from needle-like to a nanarod structure.

The hypothetical growth mechanism of the ZnO structures discussed above shows that a continuous presence of ZnO vapors (source) are necessary to form and transform the shapes of the crystals. The precipitation of ZnO on the surface of the activated rods is necessary for continuing the growth of the structures. That is, the initial structures themselves (rods) play the role of support for the deposition of ZnO vapors to transform into crystals of various shapes. The rate and availability of ZnO vapors can significantly change the morphology of the structures.

To support the above mechanism, additional experiments were conducted by increasing the residence time of the probe/sleeve inside the flame volume. By increasing the residence time of the probe (~3 minutes), the amount of ZnO vapors inside the sleeve increases and this should lead to crystal formation containing different characteristics on the surface of the Zn probe. Indeed, the formation of only well faceted large crystals or ZMPs with a short nanorod protruding from the tip was not observed in the experiment performed at Z=11 mm with a sleeve diameter of 2 mm. Instead, other unique complex crystal structures are formed (figure 4-9). Further crystallization is formed by vapor deposition directly on the nanocrystal surfaces to form more complex structures. It can be observed (figure 4-9) that some of the elongated rods have several slender polyhedral structures attached to their surfaces as if decorating the protruding nanorod. Arrows 1 and 2 in figure 4-8a1 point to diamond and rectangular shaped structures attached to the surface of the two different nanorods, respectively. Arrow 3 points to several cubic structures attached to the surface of a single rod. Arrows 4, 5 and 6 point to ZMPs that have pentagonal, circular, and rectangular cross-sections, respectively. The hypothesis is further supported by noting that the rods are independent from the "decorative" polyhedral structures. The TEM images in figure 4-8b-c show a rod outside the polyhedral and partially embedded at its base as pointed out by the arrows. This characteristic is much more clearly observed in figure 4-9f-g where slender polyhedral structures are fused diagonally to the surface of a nanorod. The rods have a darker contrast as compared to the slender polyhedral structures.
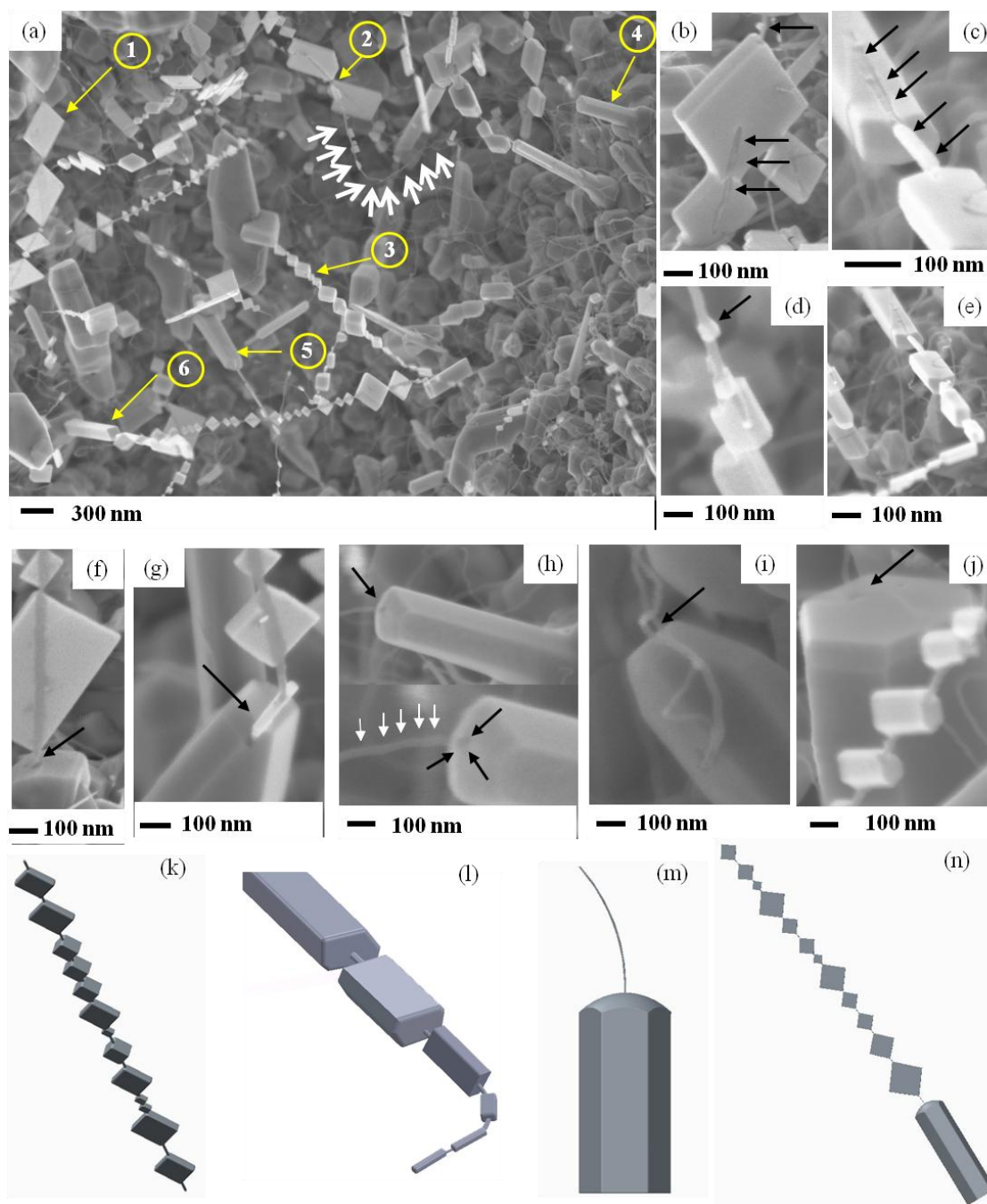
Figure 4-9- (a) SEM image collected on the surface of a Zn probe reveals the presence of high density of complex crystals. Arrows 1-6 point to several slender structures that have diamond and rectangular shapes growing on the surface of a rod, several cubic structures grown on the surface of a rod, and crystal bases that have pentagonal, circular, and rectangular cross sections, respectively; (b-e) higher magnification of selected areas in (a); (f-j) HR-SEM images showing that the larger well-faceted crystals have a protruding nanorod at their tips; (k-n) computer generated images of crystals and nanorods grown at their tips.

The direct deposition of smaller crystals on the surface of the nanorod is evident as pointed out by the arrow in figure 4-9d. The nucleation of the polyhedral structures appears to occur simultaneously at several locations on the surface of the formed nanorods due to the continuous precipitation of ZnO vapors. Figure 4-9e shows a nanorod with several decorative cubical structures with a sudden direction change of ~90 degrees. The similar bending of a rod with an earlier deposition of the decorative structures is evident in figure 4-9a (white arrows). Figure 4-9f-j shows that the ZMPs all have a nanorod protruding from the indentations (darker contrast) present at the center of their tips as pointed out by the arrows. Computer generated images of grown structures are shown in figures 4-9. Figure 4-9k represents structures shown in figure 4-9b, c, f and g, and figure 4-9l represent structure depicted in figure 4-9d and e; figure 4-9m represents structures shown in figure 4-9h and i; and figure 4-9n represent structures grown in figure 4-9j.
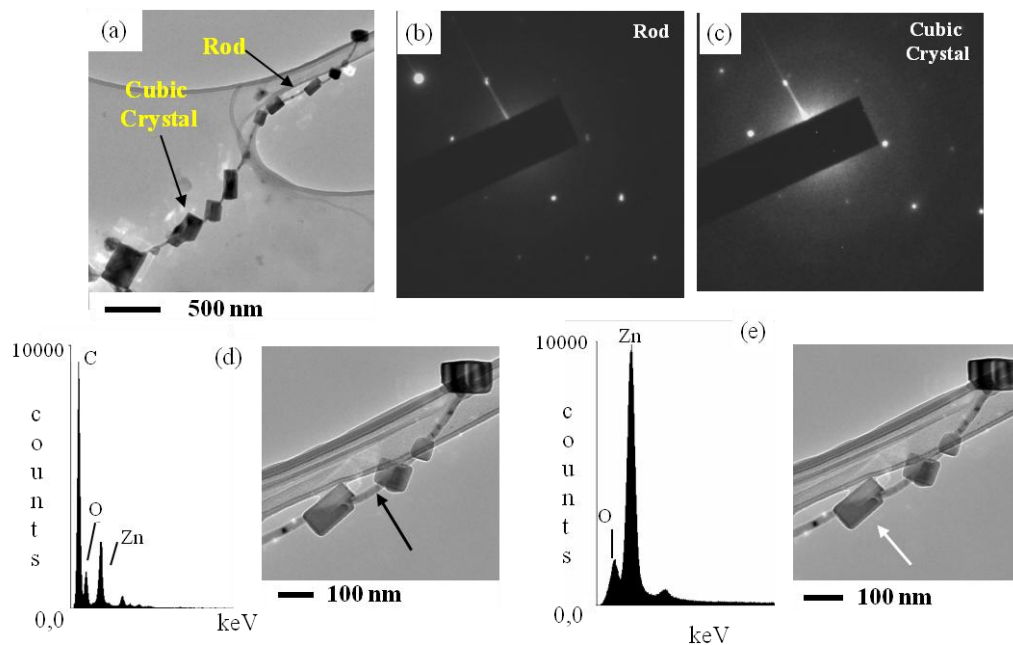
Figure 4-10- TEM image of the nanobead-like structures with corresponding SAED and EDS spectra in selected locations rod and cubic.

Figure 4-10a-e shows TEM images, SAED, and EDS spectra of the nanorod with several cubic structures attached to its surface forming a nanobead-like structure. It is interesting to note that even after several minutes of sonication, which is required for TEM analysis, the small cubical structures and the rod remained together, figure 4-10a. The EDS spectra in figure 4-10b and 10c are of the nanorod and of a cubical crystal, respectively. The EDS analysis over the nanorod shows the presence of Zn, O, and C. The carbon peak is coming from the film supporting the nanorod. The SAED collected from both, the rod and the polyhedral structure, show that they are nearly identical (figure 4-10b and c). This association is quite analogous to our proposed mechanism that the initial structures themselves play the role of supports for the deposition of Zn oxide vapors to transform into various solid shapes.

4-6- Chapter Conclusions

ZnO offers remarkable potential in applications of electronic, optoelectronic, magneto-electronic devices. In this chapter, the synthesis of ZnO nanocrystals is performed using Zn probes inserted in a counter-flow flame medium. The source material is introduced in the form of a solid wire through a sleeve. For the synthesis of the ZnO nanocrystals, the sleeve containing the zinc probe is introduced in a region of the flame that is rich in oxygen and oxygen radical. The shape and structural parameters of the grown crystals strongly depend on the flame position. The variation of insertion position from Z=12 mm (flame temperature is ~2500 °C) to Z=11 mm (flame temperature is ~2100 °C) leads to modification of crystal morphology from short thick based ZMPs with a short protruding nanorod at their tips to very elongated nanorods. The diameters of the protruding nanorods in both cases are less than 100 nanometers.

However, the physical characteristics of the crystal bases remained approximately the same. The proposed growth mechanism of the nanocrystals is composed of two different processes: 1) the global growth mechanism is responsible for the formation of vapors by the evaporation of the base metal as it is partially exposed to the flame medium. The Zn atoms are intercalated with oxygen atoms from the flame to form ZnO nuclei, and 2) once the nuclei are formed, elongated structures start to form through the vapor-solid (VS) growth mechanism. This mechanism is indirectly confirmed by increasing the residence time of the wire/sleeve inside the flame volume. This strongly suggests that the initial structures themselves (rods) play the role of support for the deposition of Zn oxides vapors to transform into various solid shapes. The protruding nanorods have slender polyhedral structures that have diamond, rectangular, and cubical shapes as if decorating the nanorods.

Counter-Flow Flame Synthesis of Tungsten-doped Molybdenum Oxide Nanostructures in the Gas Phase

5-1- Introduction

Molybdenum oxide is a chemical compound that is often used as a metallic conductor. The structural and surface properties of molybdenum oxide play an important role in its applications. Molybdenum oxides occur with a wide structural variety and range of stoichiometry. MoO_3 can exist in three polymorphs: 1- thermodynamically stable orthorhombic MoO_3 (α-MoO_3); 2- metastable monoclinic MoO_3 (β-MoO_3), and 3- metastable low temperature hexagonal (h-MoO_3). Each phase has different properties than the others. The most common fully oxidized polymorph is α-MoO_3. Also, α-MoO_3 is the most interesting because of its stacked bilayered structure of MoO_6 octahedrals with common edges and corners formed by Van der Waals force, which makes the surface easy to slice, figure 5-1a [128]. This intrinsic structure assists molybdenum ion in changing its oxidation state [129, 130]. It is possible to transform β to α at temperatures of 370-400˚C. The β-MoO_3 has a cubic structure with Mo in center of six O atoms (shared MoO_6 octahedral), figure 5-1b. The ability of MoO_3 to change oxidation state, as well as its layered structure, allows it to serve in field emission [131], lithium-ion batteries [128, 132], catalysts [133], gas sensors [134], photochromic devices, and electrochromic devices [135, 136]. The electrochromic properties have led to innovative displays and smart windows that have a role in the heating and cooling conditions in buildings. The focus on the new electrochromic devices is to improve the coloration efficiency, cycle life, and coloration response time. Also, magnetic

characteristic can be observed by doping magnetic elements in molybdenum oxide structures [137].

Tungsten in its natural state is a hard and brittle material that possesses outstanding thermal and mechanical properties. Tungsten oxides are among the most studied transition metal oxide nano/micro-sized structures. The WO_3 has a crystal structure of the perovskite-type (oxygen in the face center) and displays different polymorphs at different synthesis temperatures. The triclinic low-temperature phase is observed at -40 ˚C, and at 17 ˚C transforms to the monoclinic phase which is stable up to 330 ˚C, and again at higher than 330 ˚C transforms into the orthorhombic phase [138]. Additional high-temperature tetragonal phases exist over 740˚C. Tungsten trioxide (WO_3) has been investigated/synthesized due to its electrochromic [139-141], photochromic [142], gas, humidity and temperature sensing [143-145], and catalytic properties [146].

As some of the applications strongly depend on impurity or doping, attempts are made to synthesize mixed or doped structures. For instance, electrical conductivity of WO_3 can be significantly increased two ways: (1) reduction to WO_{3-x}, and (2) formation of tungsten bronzes M_xWO_3. The latter seems to be possible by replacing W with Mo in $W_xMo_{1-x}O_3$.

So far, grown ZnO and Nb_2O_5 nanostructures are synthesized though the solid-support synthesis method. One alternative approach is the gas-phase synthesis method. This method introduces continuous production and evolution of materials inside the flame volume. Since material can be collected at any position in the distance between the stagnation plane and source insertion, different morphologies can be collected in

one process. The thermophoretic sampling technique is the primary collection method we used to analyze materials at different positions and track the growth of them inside the flame.
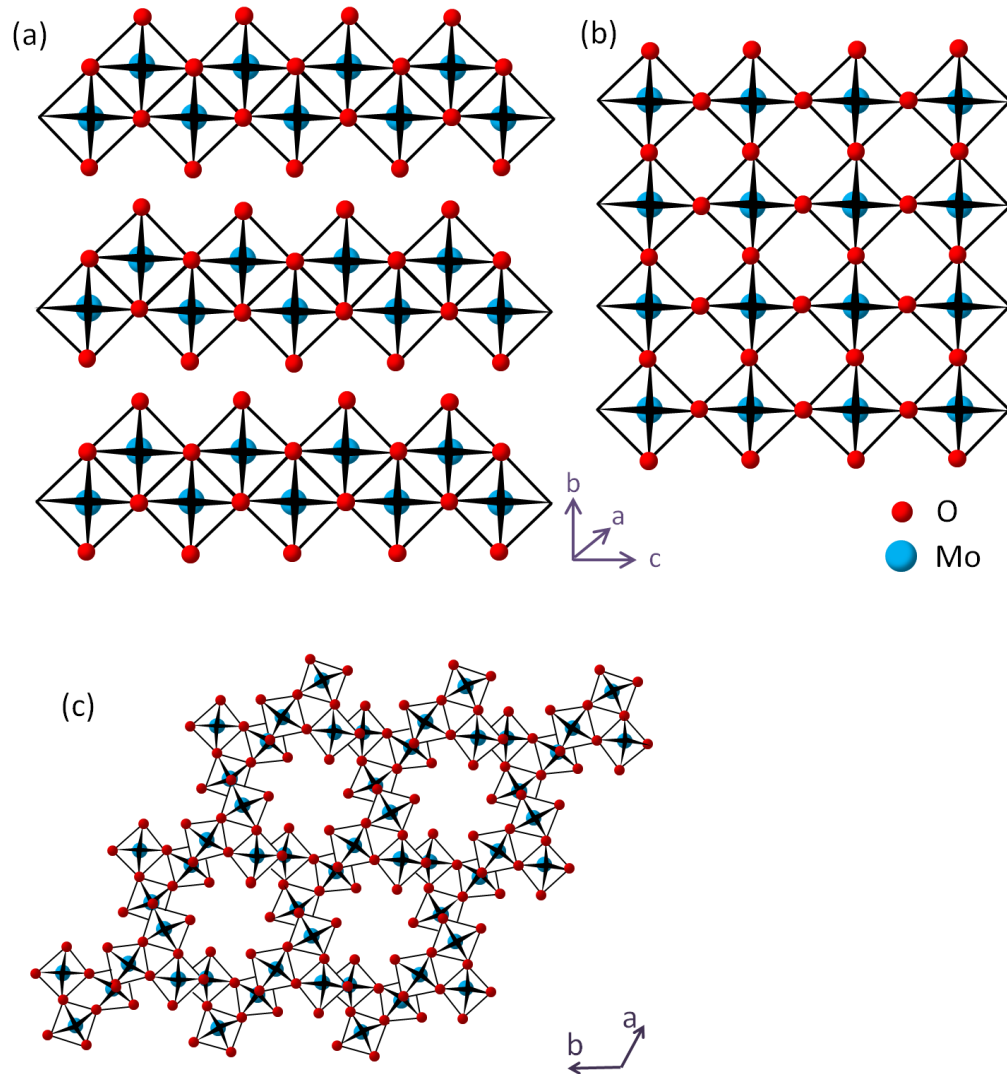
Figure 5-1- Polymorphs of MoO_3; (a) layered α-MoO_3 with orthorhombic symmetry; (b) monoclinic β-MoO_3 [147]; (c) tunnel h-MoO_3 [148].

5-2- Properties and applications of mixed molybdenum-tungsten oxide

Molybdenum and tungsten oxides have various common properties and applications. Mixed molybdenum-tungsten oxides are employed to expand applications

of molybdenum and tungsten oxides. Some potential applications of binary and single WO_x and MoO_x are briefly outlined below.

5-2-1- Gas sensing

Mixed Mo-W oxide is potentially useful in gas sensing. It exhibits a strong sensitivity to some gases present in low concentrations without any significant interference from changes in relative humidity. Molybdenum and tungsten oxide represent important sensor materials: MoO_3 exhibits sensitivity toward NH_3, H_2, CO, and NO_2 [149], and WO_3 responds well to NO_x and O_3 [150]. These sensor properties can be improved through the preparation of mixed oxides; for instance, $W_{0.9}Mo_{0.1}O_3$, independent of changes in the relative humidity (RH), shows strong sensitivity to gases such as O_3 and NO_x in low concentrations [151]. Highly selective mixed MoO_3–WO_3 show improved sensing towards detection of NO_2 and response toward O_2 as compared to pure MoO_3 [150, 152].

5-2-2- Elechtrochromic

Both MoO_3 and WO_3 separately and as mixed compounds, have commonly been applied to fields relative to electrical conductance [153]. The electrochromic process of metal oxides has been enlightened by the double intercalation of an electron and a proton to form a colored metal bronze [154]. Optically transmissive devices exhibit reversible color changes from transparent to blue (WO_3) or blue-purple (MoO_3) with applied potentials of 3-4 V. Electrochromic properties improve as the ratio of W/Mo approaches unity. Compared to either pure WO_3 or MoO_3, the mixed oxides show significantly enhanced intercalation properties, with the $W_{0.5}Mo_{0.5}O_3$ film exhibiting the highest intercalation properties. Other cations like H+, Li+, and Na+ reveal the same

trend as K+. Six major ionic species of W_{6+}, W_{5+}, W_{4+}, Mo_{6+}, Mo_{5+}, and Mo_{4+} present in the mixed oxide, which allow for increased inter- and intra-valency charge transfer [155].

5-2-3- *Lithium-ion batteries*

Nano-particles of molybdenum and tungsten oxides improved lithium-ion battery (LIB) technology. Graphite is mainly used in LIBs as anode electrodes and it shows the capacity of ~350 mAh/g. However, it has been reported that nano-structured MoO_x electrodes display the capacity of ~620 mAh/g [140]. Moreover, the Li storage performance of MoO_2 improves by tungsten doping and results in a high reversible capacity, better cycling and rate performance. Mesoporous W-doped MoO_2 sample exhibits a reversible electrochemical lithium storage capacity as high as 700 mAh/g with good cycling and rate performance. This material can improve properties of LIBs since it shows higher capacity than a regular battery. MoO_2 possesses metallic electrical and high capacity storage and is a key candidate as an anode material for LIBs [156]. Studies show that a film made of homogeneous mixed $Mo_xW_{1-x}O_3$, with Mo content ranging in 0.4<x<0.7, demonstrates moderately improved electrochromic, ion-transport (e.g. lithium-ion batteries) properties, and structural stability compared to WO_3 and MoO_3 during electrochemical cycling [157].

5-2-4- *Photochromic*

Both molybdenum and tungsten oxide nanostructures have displayed very strong photochromic effects. Photochromic is defined as the capability of a material to change reversibly color or shade when exposed to light. Change in color occurs upon going from one oxidation state to another state. It has been shown that mixed WO_3 and MoO_3

76

nanostructure color change is significantly faster than bulk MoO_3 [158]. h-MoO_3 shows higher photochemical efficiency than α-MoO_3 under UV light. Openness in structure (tunnel structure) of h-MoO_3 leads to an efficient electron-hole separation and provides larger spatial locations for ion insertion/extraction and diffusion and consequently enhances photochromic properties [159]. Schematic images of some of the aforementioned applications are shown in figure 5-2.

(a) Rechargeable batteries

(b) Capacitors

(c) Solar cells

(d) Gas Sensors

(e) Catalyst

(f) Electrochromic windows
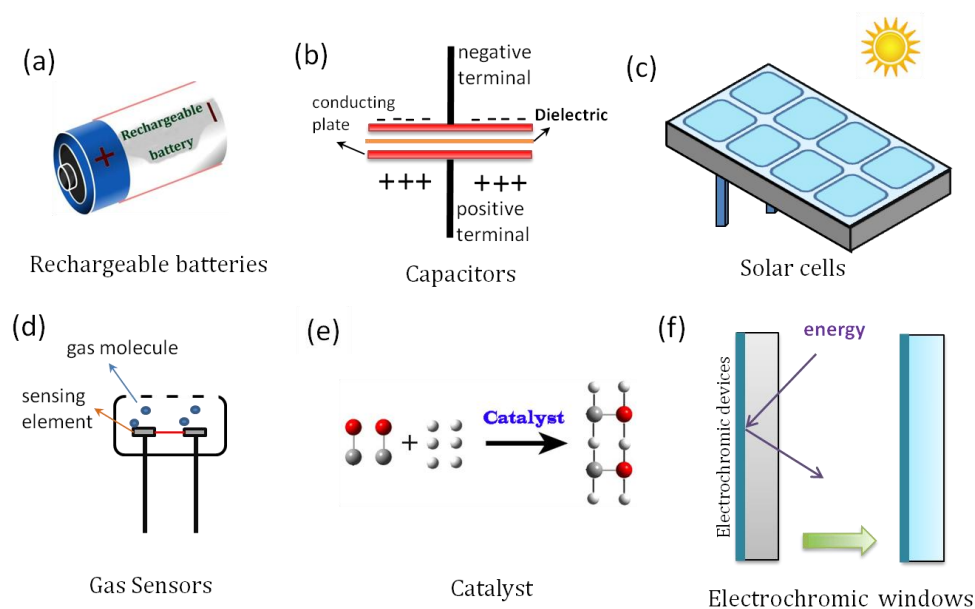
Figure 5-2- Different applications of molybdenum and tungsten oxides.

5-3- Synthesis methods of mixed Mo-W Oxide nanostructures

This section outlines different methods by which MoO_3, WO_3, and mixed MoO_3-WO_3 compounds are synthesized. The experiment procedure, source materials, and results are briefly explained.

5-3-1- *Chemical vapor deposition method*

Gesheva et al. (2007) [160] reported a study on the structural transformation and electrochromic and optical properties of a single molybdenum oxide compared to a

MoO_3-WO_3 mixture. Thin films of molybdenum and tungsten were deposited at 200˚C in the hexacarbonyls structure. As the compound reached 400˚C, the molybdenum oxide crystallization process was nearly complete, forming both triclinic and orthorhombic crystalline phases. The mixed oxide films formed the triclinic crystalline phase containing tungsten oxide with molybdenum atoms as substitutes. All of the films showed electrochromic effect, however the mixed MoO_3-WO_3 films expressed stronger electrochromic effects with higher color efficiency.

Ivanova et al. (2003) [161] prepared mixed Mo/W oxides through atmospheric-pressure CVD by having the Mo/W oxide films formed by decomposition of $W(CO)_6$ and $Mo(CO)_6$ in the ratio of 4 to 1 at atmospheric pressure. The decomposition time was kept constant at 40 minutes and due to the dissimilar growth rates, the film thickness of MoO_3, WO_3, and Mo/W mixed oxide films were 300nm, 400nm, and 120nm, respectively. The cyclic-voltammetry measurements were performed with three electrodes. The WO_3 showed a bluish color, MoO_3 as yellowish, and W-Mo mixed oxide as brownish. The MoO_3 films crystallized into orthorhombic phase while the WO_3 and W-Mo films remained amorphous. The most interesting character is the increase in the charge rate for the W-Mo films. This makes the mixed oxides suitable for electrochromic devices. After extracting Li^+, the films were bleached and the most color change was obtained for the W-Mo mixed oxide film. In this study, the group found that $Mo_{0.07}W_{0.93}O_3$ and MoO_3 films electrodes exhibit a strong performance as a component in electrochromic devices.

5-3-2- Sol-Gel method

Sun et al. (2009) [162] synthesized mixed molybdenum-tungsten oxides with various stoichiometry through sol-gel deposition on a conductive fluorine doped tin oxide (FTO) coated glass. Also, the optical transmittances of the films were recorded with respect to air in the reference beam in an ultraviolet-visible near-infrared spectrophotometer. Finally, the cyclic voltammetry measurements were carried out to measure ion storage capacities and reversibility of the films during the coloring process of mixed metal oxide films in an electrolyte solution. Results showed electrochromic and lithium-ion transport properties of mixed molybdenum-tungsten oxides were moderately enhanced.

Galatsis et al. (2001 and 2003) [150, 152] produced MoO_3, WO_3, and MoO_3-WO_3 compounds at different atomic percentages by sol-gel spin coating techniques and annealing at 450˚C on silicon substrates. Electrical responses were recorded as the mixtures were exposed to specific levels of CO and NO_2. Results proved that gas responses, morphology, and crystalline phases for each mixture were strongly influenced by the W/Mo weight ratio. It was reported that when MoO_3 single oxide annealed between 400ºC and 500ºC displayed well developed orthorhombic structures, but as the temperature was increased to roughly 600ºC, the MoO_3 changed from a crystalline to an amorphous phase. WO_3, on the other hand, displayed a well crystallized monoclinic form ranging through temperatures as low as 300 ºC and up to 700 ºC. When comparing these results to the mixed oxide, the Mo/W compound was annealed at 450 ºC, forming a monoclinic oriented WO_3 compound in an amorphous MoO_3 phase.

5-3-3- Plasma method

Plasma is a widely used technique which merges with other methods such as CVD to enhance performance of the synthesis methods. Following are examples of experiments incorporating the plasma synthesis method.

Tracy and Benson (1986) [163] investigated the feasibility of using plasma enhanced chemical vapor deposition (PE-CVD) to produce electrochromic thin films of tungsten and molybdenum oxides. Gaseous WF_6 or vapors of either $W(CO)_6$ or $Mo(CO)_6$ were employed as the source materials. The wavelengths and electrochromic properties were carefully measured and recorded. Optically transmissive devices exhibited reversible color changes from transparent to blue (WO_3) or blue-purple (MoO_3) with applied potentials of 3-4 V. Results proved that the MoO_3 films offered the potential for manufacturing electrochromic devices with higher contrast ratios. Various techniques, such as emission spectroscopy and x-ray diffraction, indicated that all of these thin film deposits of various chemical mixtures were predominantly amorphous tungsten and molybdenum oxides. Results show that the contrast ratio of a PE-CVD MoO_3 electrochromic device is high and its color change is more neutral. This proves that both tungsten and molybdenum oxides produced the greatest amount of electrochromic qualities.

Cvelbar et al. (2012) [164] created sub-oxide-to-metallic crystalline nanowires with uniformly distributed nanopores by using a novel combination of plasma and re-deposition with electron-beam reduction. This process involves synthesizing single-crystalline MoO_3 nanowires using the RF- (radio frequency) PECVD method. Pure Mo foil is exposed to RF plasma created in oxygen gas discharge. As the oxide layer is

being created on the Mo foil, the surface temperature increases, then the molybdenum oxide evaporates from the sample. The evaporated oxide is then deposited to 20 mm distant borosilicate glass plate heated to ~500 ˚C. The interaction of evaporated molybdenum oxide with oxygen radicals localized Mo-O plasma, created between the Mo foil and the deposition plate. The MoO_3 is then deposited on the substrate holder surface in dense arrays. A typical length of the NWs grown in array is 1-2 µm with a diameter of 40-80 nm. This is dependent on the plasma parameters which are typically controlled by discharge parameters.

Table 5-1 lists frequent methods that are employed to synthesize molybdenum and tungsten oxides nano/micro structures.

Table 5-1- List of different employed methods to grow molybdenum and tungsten oxide nano/micro structures.

Method	Experimental configuration	Author(s)	Morphology of structures
CVD Process		Gesheva et al. [165]	
Electro-deposition		McEvoy et al. [166]	
Sputtering		Vomiero et al. [167]	
Sol Gel		Galatsis et al. [168]	

5-3-4- *Flame synthesis methods*

It has been shown that flame synthesis offers high growth rate for scalable production of metal oxide nanostructures with unique properties and morphologies [115, 169]. This method not only can grow single crystalline nanostructures, but also dope the nanostructures to give additional functionalities to the materials. Compared to other currently employed methods, the flame synthesis is usually a single-step process

with no need for post-preparation resulting in an inexpensive growth of nanomaterials. Further information regarding different approaches of the flame method is provided in sections 1-4 and 1-5. Details of the flame method in production of mixed metal oxides are explained below.

Lili Cai et al. (2011) [170] used co-flow flame synthesis to create the mixed oxides such as W-doped MoO_3 and $Cu_3Mo_2O_9$. By using flame vapor deposition and solid diffusion methods, three new methods were introduced: simultaneous vapor-vapor and solid-vapor growth, and sequential solid-vapor growth. In those experiments, they employed a co-flow flat premixed flame with a diameter of 6 cm. The main goal of the flat premixed flame is to get the temperature nearly constant in any plane parallel to the burner. In the simultaneous vapor-vapor growth, vapors of two different metals were combined and deposited. This can only occur when the vapor content of WO_x and MoO_x and growth substrate temperature are moderately low. Through this growth W-doped MoO_3 nanoplates and nanoflowers were produced. Nanoflowers appeared as a result of using Au catalyst after 20 minutes. For the simultaneous solid-vapor growth, the diffusion substrate and vapor metal needed to be at positions where highest growth rate and lowest vapor concentration were respectively available. $Cu_3Mo_2O_9$ nanowires were grown through this process. The last growth method used solid diffusion as seeds for further flame vapor deposition. For this, the diffusion substrate and vapor metal need to be at positions where the highest growth rate and lowest vapor concentration are respectively available. It resulted in the growth of core/shell CuO/MoO_3 and MoO_3-branched CuO nanowires.

Yunzhe Feng et al. (2013) [171] introduced a sol-flame method to form mixed molybdenum-tungsten oxides. The new sol-flame method was used to synthesize hybrid metal oxide NWs (nanowires) such as nanoparticle- (NP-) shell decorated NWs and NP-chain decorated NW. The processes in the sol-flame method are a combination of flame synthesis of the NWs and a sol-gel preparation. The single metal oxide NWs were grown on the surface of a substrate. A NP precursor solution was first prepared and then the NWs (on the substrate) were dipped into the solution. The dip-coated NW arrays were allowed to dry, which left a metal salt cover on the NWs. Subsequently, the NWs were heated in the premixed flame that dissociates and oxidizes the metal salt and also evaporates the rest of the solvents. The flame temperature has a direct effect on the morphology of the NPs. For example, when Zn salt was annealed at 550°C, it formed a uniform ZnO NP shell, but when it was annealed at 1100°C, it formed a hybrid structure fanning radially from the NW core. The annealing process of the sol-flame method can be achieved either with furnace annealing or flame annealing. Flame annealing leads to smaller diameter NPs and densely covers the NWs. The Sol-Flame method is able to synthesize three different sorts of hybrid metal oxide NWs: NP-shell@NW, NP-chain@NW, and doped NWs.

Table 5-2 lists different flame methods that are employed to synthesize molybdenum and tungsten nano/micro structures.

Table 5-2- List of different employed flame methods to grow mixed Mo and W oxide nano/micro structures.

Method	Experimental configuration	Author(s)	Component	Fuel	Morphology of structures
Co-flow flame		Cai *et al.* [170]	MoO_3	Ch_4+H_2	
Co-flow flame		Cai *et al.* [170]	W-doped MoO_3	Ch_4+H_2	
Co-flow flame		Cai *et al.* [170]	$Cu_3Mo_2O_9$	Ch_4+H_2	
Co-flow flame		Cai *et al.* [170]	CuO/MoO_3	Ch_4+H_2	
Sol-flame		Feng *et al.* [171]	W-doped TiO_2	Ch_4+H_2	
Sol-flame		Feng *et al.* [171]	ZnO @CuO	Ch_4+H_2	

85

5-4- Synthesis of W-doped molybdenum oxide nanostructures in the flame

The same counter-flow flame reactor that was explained in chapter 2 is employed for the synthesis of W-doped-MoO_3 nanostructures.

Molybdenum and tungsten wires with a purity of ~%99.99 (Sigma Aldrich Corporation) and diameters of 1 mm were used as the source materials. Wires were simultaneously introduced radially in the flame medium parallel to the nozzles' planes. The tungsten wire was inserted at Z=12 mm and the molybdenum wire was inserted at Z=14 mm. Z represents the distance between the fuel (top) nozzle to the center of the wire (figure 5-3a1). Wires are held by a ceramic tube with four holes. Two holes with a 2 mm center-to-center distance were used for the experiment (figure 5-3a2 and 3a3). The introduced wire in the counter-flow flame was affected by strong temperature and chemical species gradients (figure 5-3b). The position of the wires in the flame volume greatly influenced the synthesis processes. At Z=12 mm, the flame temperature is ~2500 °C and the oxygen content is 0.015 mole fraction, and at Z=14 mm, the flame temperature is ~2150 °C and the oxygen content is 0.25 mole fraction. Silvestrini et al. predicted the flame temperature by a numerical calculation. It was performed by considering 1160 reactions and 325 chemical species [63].

The longest insertion time period was 120 seconds and shorter insertion time periods assisted us to properly comprehend the growth mechanism. A schematic image of the grid used for the thermophoretic sampling technique is shown in figure 2-5, chapter 2.
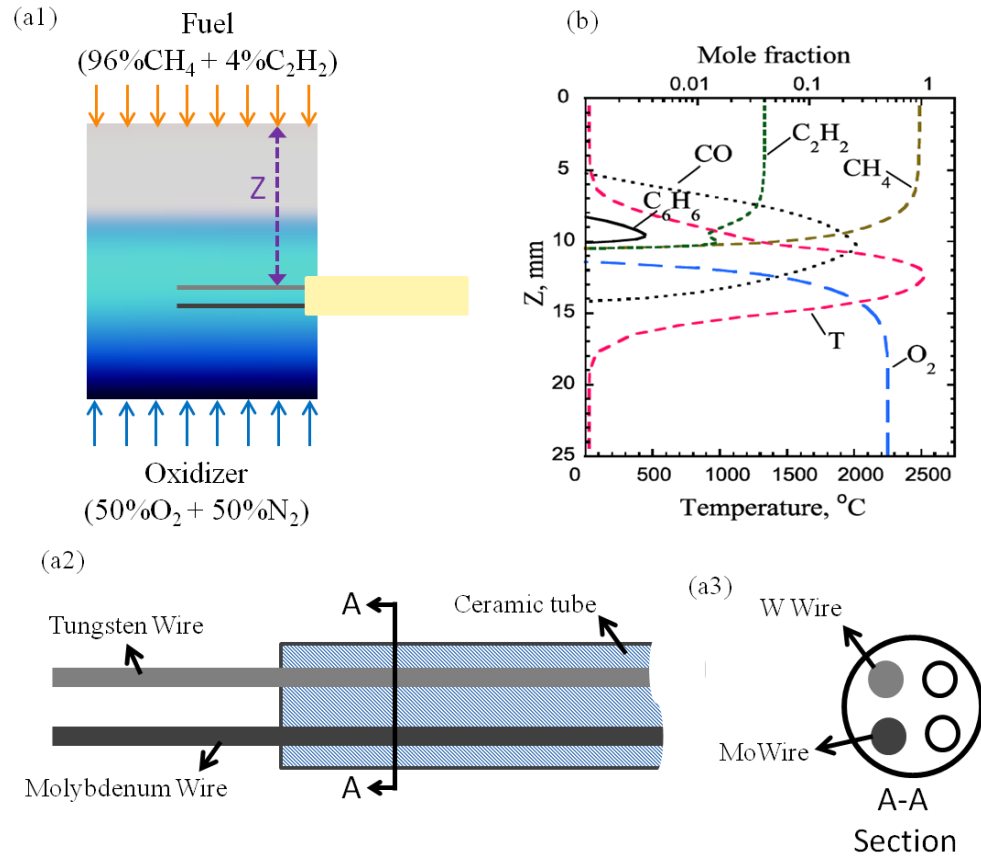
Figure 5-3- (a1) A photograph of the counter-flow flame along with a schematic showing insertion of the molybdenum and tungsten probe inside the oxidizer zone of the flame; (a2) a schematic of the ceramic tube that keeps the wires stable inside the flame; (a3) A cross section of the ceramic tube and the wires inside it; (b) profile of numerical predictions of temperature and major chemical species in the diffusion counter-flow flame as a function of the distance from the fuel nozzle (Z)[63].

5-5- Results and discussion

The one-dimensional counter-flow diffusion flame is characterized by strong chemical species gradients and temperature (up to 2000 K/cm). While the oxidizer side is rich in O, OH, O_2, and other oxidative species, the fuel side of the flame is rich in hydrocarbon species (figure 5-3b). As a result, the insertion position of the probes in the flame plays a key role in growth and morphology of synthesized structures.

In this study, two probes, one tungsten and the other one molybdenum, were simultaneously inserted at Z= 12 mm and Z= 14 mm (oxygen-rich zone of the flame),

87

respectively. The thermophoretic sampling technique was employed to directly collect samples of nanomaterials from the flame volume at heights of Z= 10, 11, and 13 mm. Considering the 3 mm diameter of the TEM grids, it was possible to study the evaluation of structures in the Z height range of 9 to 14 mm. This range covered the entire oxygen-rich zone. The configuration of probes led to the growth of novel mixed metal oxide nanostructures. The gas-phase synthesis happens on the oxygen-rich zone. A TEM analysis of the samples shows the particles' evolution as they are carried by the gas flow towards the stagnation plane. An evaluation of grown structures from early shapeless particles near the surface of the probes to intercalation of W and Mo oxide and final state of well-defined cubical nanostructures was conducted.

Particles collected at the flame height of Z= 13 mm, where the TEM grid is just above the surface of the Mo probe, show that small shapeless particles are formed (figure 5-4a). The small particles are surrounded by larger particles. Particles are indicated by arrows in figure 5-4a. The larger particles resemble spherical shape with an irregular boundary. Spherical-like particles are molybdenum oxide vapors evaporated/sublimated from the Mo probe as a result of the probe and flame interaction. The characteristic of these particles resembles structures grown in the gas-phase synthesis of molybdenum oxide alone [68]. Metal oxide vapors formed near surface of probes in the gas-phase are characterized by neither regular shapes, which means no well-defined edges, nor sharp corners [68, 172]. The particles grow larger and also they form a well-defined shape as they travel in the flame towards the stagnation plane.
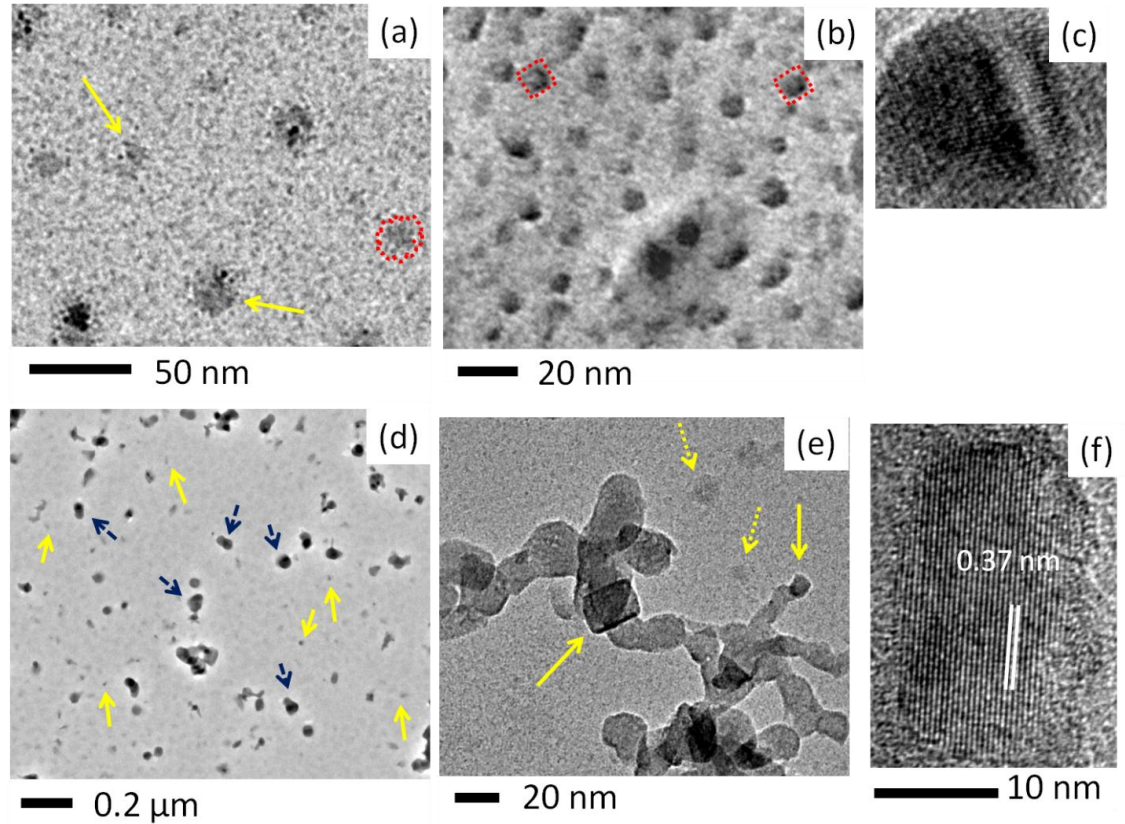
Figure 5-4- Transformation of molybdenum oxide structures through the flame; (a) shapeless particles near surface of the Mo probe at Z=14 mm; (b) high density cubic structures of molybdenum oxides; (c) a HR-TEM image show well-organized atomic structure; (d) shapeless particles of evaporated tungsten from the W probe accompanied by developed molybdenum oxide structures; (e) link-like chain structures and a well-faceted cubic molybdenum oxide; (f) a HR-TEM image shows structures at Z=12 mm are α-MoO_3.

Figure 5-4b represents transformation of shapeless molybdenum oxide particles to cubic structures. Cubic morphology is the typical shape of molybdenum oxide nanostructures synthesized in the gas phase. These structures are collected thermophoretically at Z= 12.4 mm from the flame medium. The grown molybdenum oxide structures have high density at this position. It is evident from the TEM image that the structures begin to form a well-defined morphology, which here is cubic. A careful inspection reveals that cubic structures have flat solid edges and tend to form sharp corners as it is shown by dotted lined around sample structures in figure 5-4b. In

the case of synthesis of molybdenum oxide alone, structures form more well-defined morphology and evolve into elongated rod structures as they travel 2 mm away from the molybdenum surface in the flame volume [68]. However, due to impact of tungsten probe, well-defined structures are not fully formed in a short distance away from the molybdenum probe. Figure 5-4c shows a high-resolution TEM image of a typical shapeless molybdenum oxide structure collected at Z= 12 mm. As it can be seen, even shapeless particles have a well-organized atomic structure.

The tungsten probe is inserted at Z=12 mm. At this position evaporated tungsten oxide particles from the tungsten probe can be observed on TEM grids (figure 5-4d). Small discrete shapeless particles, which are tungsten oxide nuclei, (solid arrows) are accompanied by larger crystalline molybdenum oxide structures (dashed arrows). Higher resolution TEM images show that particles are agglomerated to form chain-like structures as a result of particles fusion (figure 5-4e). Molybdenum oxide structures tend to transform to cubic structures away from the probe [68]. A cubic molybdenum oxide is pointed by a solid arrow in figure 5-4e. Also, a HR-TEM image of structures collected at Z=12 mm shows that the structures have lattice spacing of 0.37 nm which is corresponding to orthorhombic MoO_3 with lattice constants a=3.963, b=13.856, c=3.696 Å (PDF card # 035-0609).

Evaporation and deposition of tungsten oxide vapor on the surface of MoO_3 structure lead to crystalline transformation of the structure. Samples collected at Z=11.6 mm, at higher position than the surface of the tungsten probe, show that faceted (cubic) structure are attached to and also accompanied by shapeless structures. Faceted structures are highlighted by doted rectangles and shapeless structures are indicated by

solid arrows in figure 5-5a. It is the effect of deposition of tungsten oxide vapor on the surface of the previously formed MoO_3. The deposition of the tungsten oxide vapor leads to irregularity and transformation in the crystalline structure of the MoO_3 structure. Figure 5-5b shows a HR-TEM image of a structure at this position (Z=11.6 mm). Inconsistency and irregularity in crystal and direction of atomic layers are obvious. Also, lattice spacing at this position is increased to 0.39 nm which might be as a result of tungsten intercalation into layered structure of MoO_3 [173].
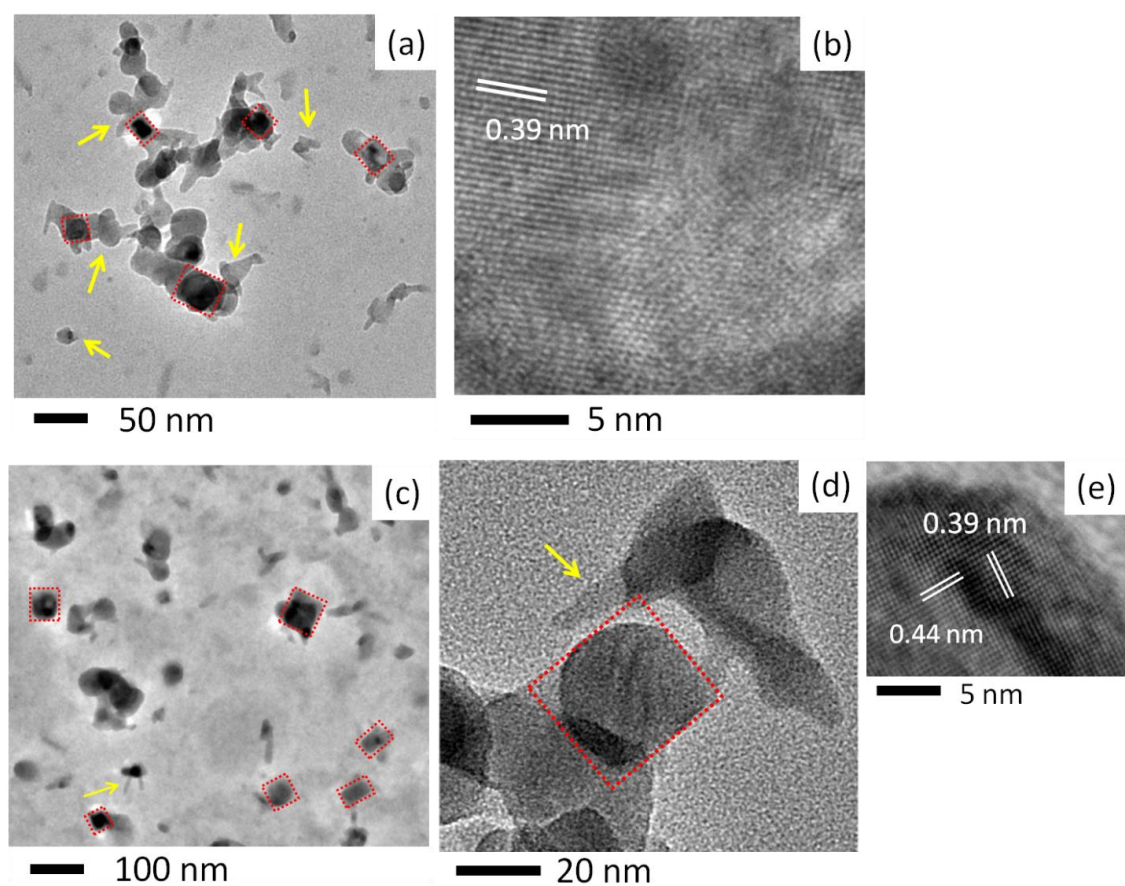
Figure 5-5- Evolution of structure through the flame medium; (a) collected structures at Z=11.6 mm; (b) HR-TEM image of structures shown in (a); (c) collected structures at Z=11 mm and appearance on nanorods attached to cubic structures; (d) collected structures at Z=10.6 mm; (e) HR-TEM image of structures shown in (d).

The deposition and intercalation of tungsten oxide vapor continue as structures/materials are carried by the gas flow of the flame towards the stagnation plane. Collected samples show that structures tend to transform to cubic structures. Figure 5-5c depicts cubic structures collected at Z=11 mm. As it can be seen, nanorods-like structures are attached to some other structures; arrows in figures 5-5c and 5d indicate them. Tungsten oxide structures turn to nanorods in the gas-phase synthesis [172]. Thus, appearance of nanorods is a possible effect of tungsten oxide on growth of the structures. A HR-TEM image of structures collected at Z=10.6 mm is shown in figure 5-5e. It shows that structures at this position are well crystallized and have constant lattice spacing throughout crystalline structure. Measured lattice spacing are larger than typical MoO_3 which shows transformation of the material from pure MoO_3 (figure 5-5f) to intermediate structures (figure 5-5b) and then well-developed structures (figure 5-5e). Intercalation of tungsten atoms in MoO_3 layers is a possible reason for increase in lattice spacing of the structures [173, 174].

As grown structures are carried by the gas flow in the flame, they encounter high temperature and chemical species gradients which bring about evolution and change in morphology of structures. Collected samples at Z=10.2 and 10 mm reveal that cubic structure is still the dominate morphology throughout the process. As discussed before cubic structure is the typical observed morphology of synthesized MoO_3 in the gas phase [68]. Cubic structures are shown in figures 5-6a and 6b. The lattice spacing of crystals has not changed as it is shown in figure 5-6c. Nanorods attached to the structure tend to disappear at this position (Z=10 mm). Figure 5-6d shows that thickness of attached nanorods is reduced in comparison with the figures 5-6a. Tale-like structures

are indicated by solid arrows. Growth of structures continues as they travel in the flame. More fully developed structures can be observed further away from the probes. Fully-developed structures have well-defined facets as it can be seen in figures 5-6e and 6f. They show collected structures at Z=9 and Z=9.8 mm respectively. Cubic structures have widths in the range of 20 to 100 nm.
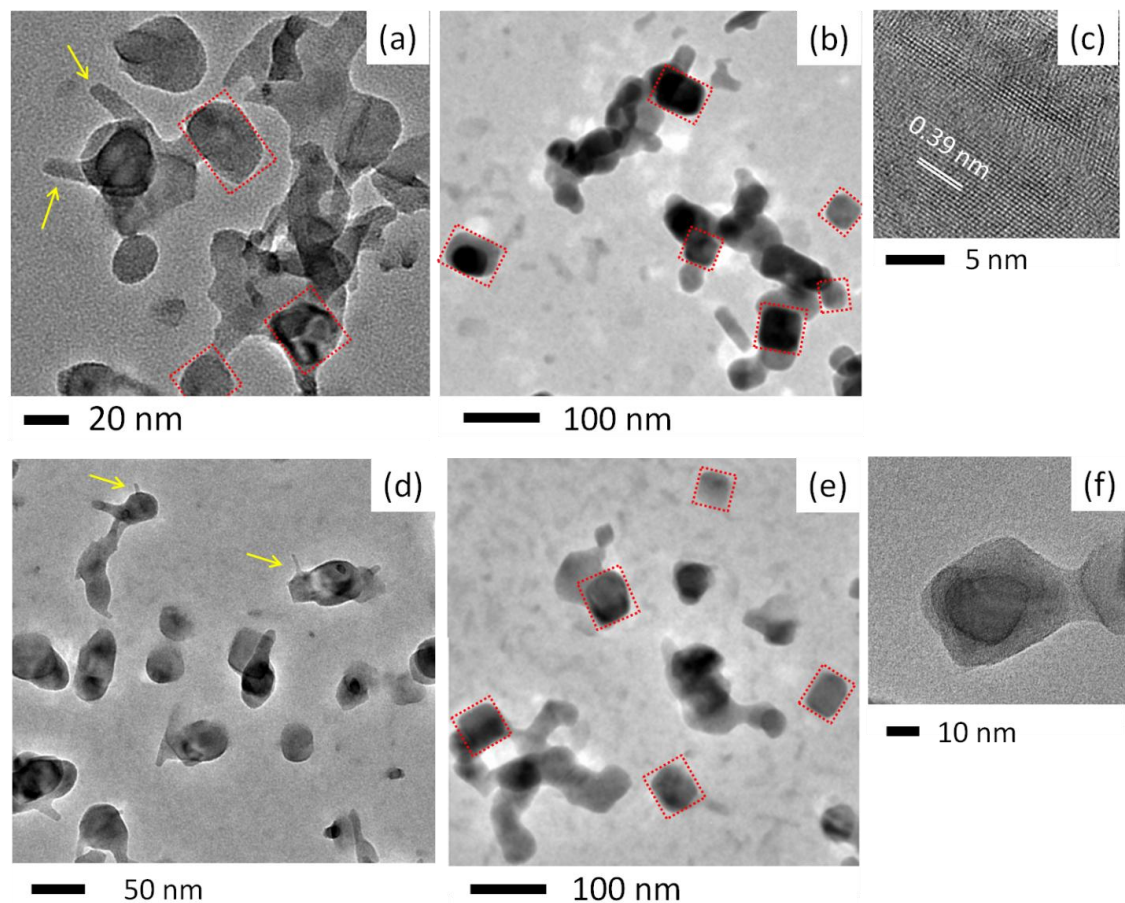
Figure 5-6- Evolution of grown structure in the flame volume at distances from the probes; (a) collected sampled at Z=10.2 mm; (b) collected structures at Z=10 mm; (c) HR-TEM image of structure shown in figure (b); (d) Structures at Z= 9.8 mm; (e) collected crystal structure at Z= 9 mm; (f) the cubic structure of grown structures at Z=9.8 mm.

The TEM image in figure 5-7a shows typical accumulated grown cubic structures in the flame volume. These structures are developed under constant flux of MoO_x and WO_x in form of vapor. Energy-dispersive X-ray spectroscopy (EDS)

elemental mapping under TEM reveals that the nanostructures contain evenly distributed tungsten, molybdenum, and oxygen (figure 5-7b-d). The HR-TEM image (figure 5-7e) and SEAD pattern (figure 5-7f) of structures indicate rectangular diffraction pattern on the (010) surface correlated to orthorhombic configuration. The measured lattice spacing of the structures shows expanded lattices in both a and c axes which may be attributed to the incorporation of tungsten in the MoO_3 structures. Thus, the synthesized structures are tungsten-doped MoO_3. The synthesized structures still maintain the α-MoO_3 crystal structure. These images indicate that the high temperature, even for a short travel inside the flame volume, is very effective to make the diffusion of the dopant (W) into existing crystal possible without altering the crystalline structure.
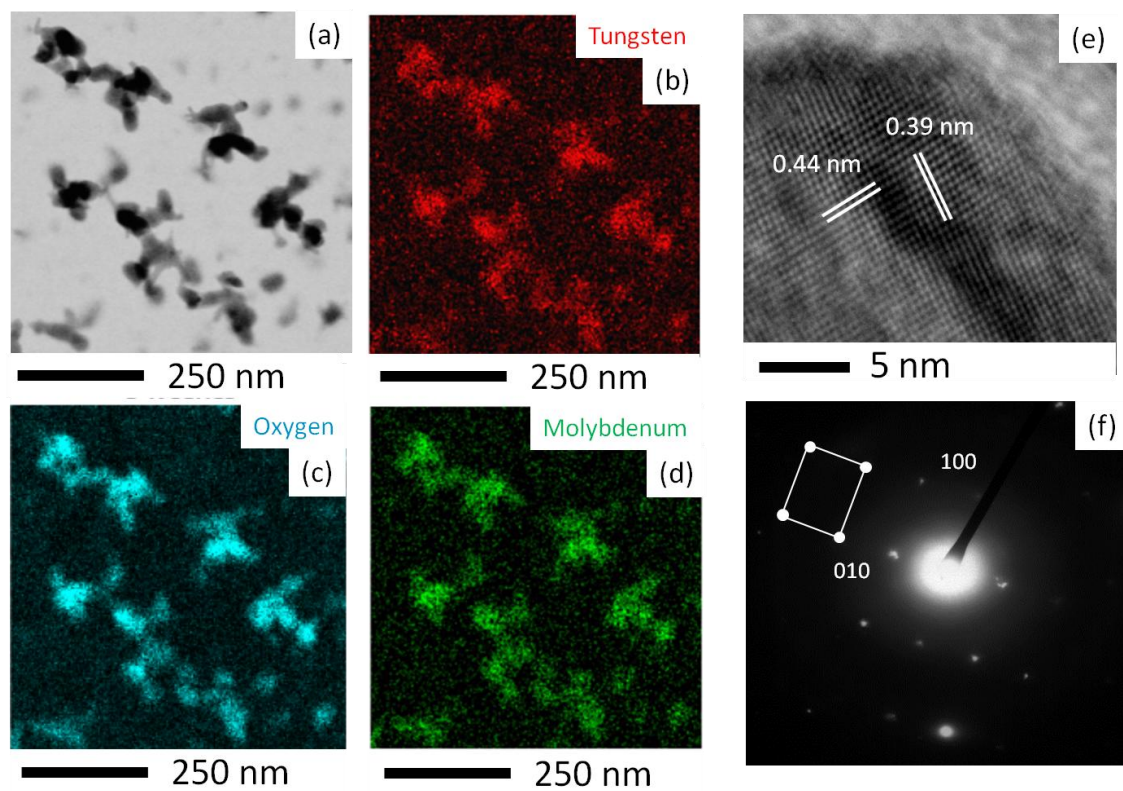
Figure 5-7- TEM-EDS analysis of the tungsten-doped MoO_3 nanostructures; (a) TEM image of the nanostructures. EDS mapping of (b) Tungsten, (c) Oxygen, and (d) Molybdenum in W-doped MoO_3; (e) HR-TEM image of a nanostructure; (f) SAED pattern image of grown W-doped MoO_3.

5-6- Growth mechanism

Structures are directly collected from inside the flame volume at different Z heights employing the thermophoretic sampling technique. The contour of flame temperature is shown in figure 5-8a. As the Mo and W wires are exposed to the high flame temperature, WO_x and MoO_x vapors nucleate near the surface of wires. At high temperature region, nuclei are suppressed by the high vapor concentration, so nuclei coagulate and form small particles. Further shape evolution and crystallization continue as structures/particles are carried away from the wires at a region of lower temperature towards the stagnation plane, figure 5-8b [175]. Temperature gradient is 550 K/mm at the blue zone. The combination of temperature and chemical species variation creates a suitable environment for a shape evolution and growth condition for cubic crystals (figure 5-8c). At the relatively low temperature region, the growth mechanism correlated with transformation of gas to solid by direct vapor deposition on previously formed nanocrystal surfaces [108]. The deposition of WO_x nuclei on MoO_3, the intercalation of W into MoO_3 structures, and further crystallization are chemically assisted by the temperature gradient of the flame volume. Figure 5-8c clearly shows that particles near the surface of the W wire transfer to well-defined cubic crystals at the lower temperature (further away from surface of the wire).
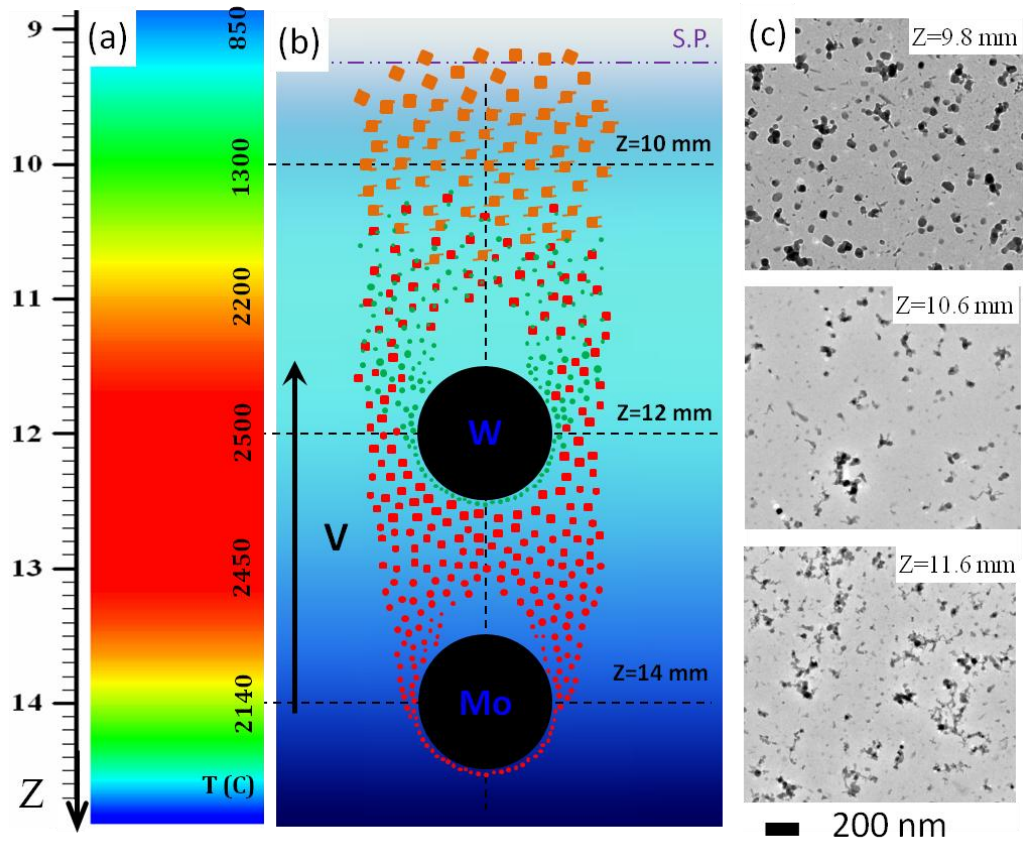
Figure 5-8- (a) contour of predicted flame temperature in Celsius at the blue zone [63]; (b) particles and structures are carried by the gas flow towards the stagnation plane; (c) shape evaluation of the structures inside the flame volume. Particles and fully developed structures are carried by the gas flow towards the stagnation plane.

The Mo wire is introduced at Z=14 mm where the flame temperature is approximately 2100°C, figure 5-8a. At the high flame temperature evaporation starts and produces Mo vapors or monomers. Simultaneously, Mo vapors combine with oxygen (from the flame volume) to form molybdenum oxide nanoparticle vapors. The MoO_x particles in the form of vapor are carried by the gas flow. The continuous influx of the vapor leads to increase in the vapor concentration and consequently suppersaturation occurs. The coagulations of the vapors generate clusters or particles. The clusters/particles further grow by either coagulation with other particles or condensation of vapor [176]. Figure 5-9a shows a sample of an early-formed a particle

and monomers collected at Z= 13 mm, just above the surface of the Mo wire. The monomers are indicated by arrows in figure 5-9a1. The shapeless particles at this position are building block of larger well-defined structures collected at the upper part of the flame. The growth progress depends upon oxide phase development. Figure 5-9a2 shows a HR-TEM image of an early-formed particle which has a well-organized lattice structure. Measured lattice spacing matches with α-MoO_3 structures. The same result was observed by gas-phase synthesis of molybdenum oxide alone in the counter-flow flame [68]. Growth of particles/clusters continues and they transform to well-defined structures at higher positions.

Right at Z=12 mm, where W wire is introduced in the flame volume, shapeless particles are transformed to discrete cubic MoO_3, figure 5-9b. At Z= 12 mm, thermophoretically collected materials are well-define and discrete MoO_3 nanocubes that are shown in figure 5-9b1. A few micrometers above the W wire chain-like structures attached to MoO_3 cubes are observed. Flame temperature around tungsten wire is ~2500˚C which causes evaporation and vapor formation of tungsten. Shapeless vapor of tungsten are coagulated very similar to molybdenum vapors. However, vapors form chains and deposited over previously formed MoO_3 nanocubes or other tungsten chains. Figure 5-9b2 clearly shows that discrete nanocubes are surrounded by chains-like tungsten oxides. Arrows indicate chain-like tungsten structures and cubic MoO_3 are indicated by rectangles in figure 5-9b2. The coherent interface (happens when two crystals have the same atomic configuration) between the mother MoO_3 (mother phase) and the WO_x monomers/vapors requires a low interfacial energy. This low energy favors the nucleation of the WO_x on MoO_3 [177]. The nucleation might be the basic

reason for the topotactic reaction (a topotactic transition associates with a structural change due to loss or gain of material, so that the ultimate lattice is related to that of the mother material) and transformation in the solid state [177].
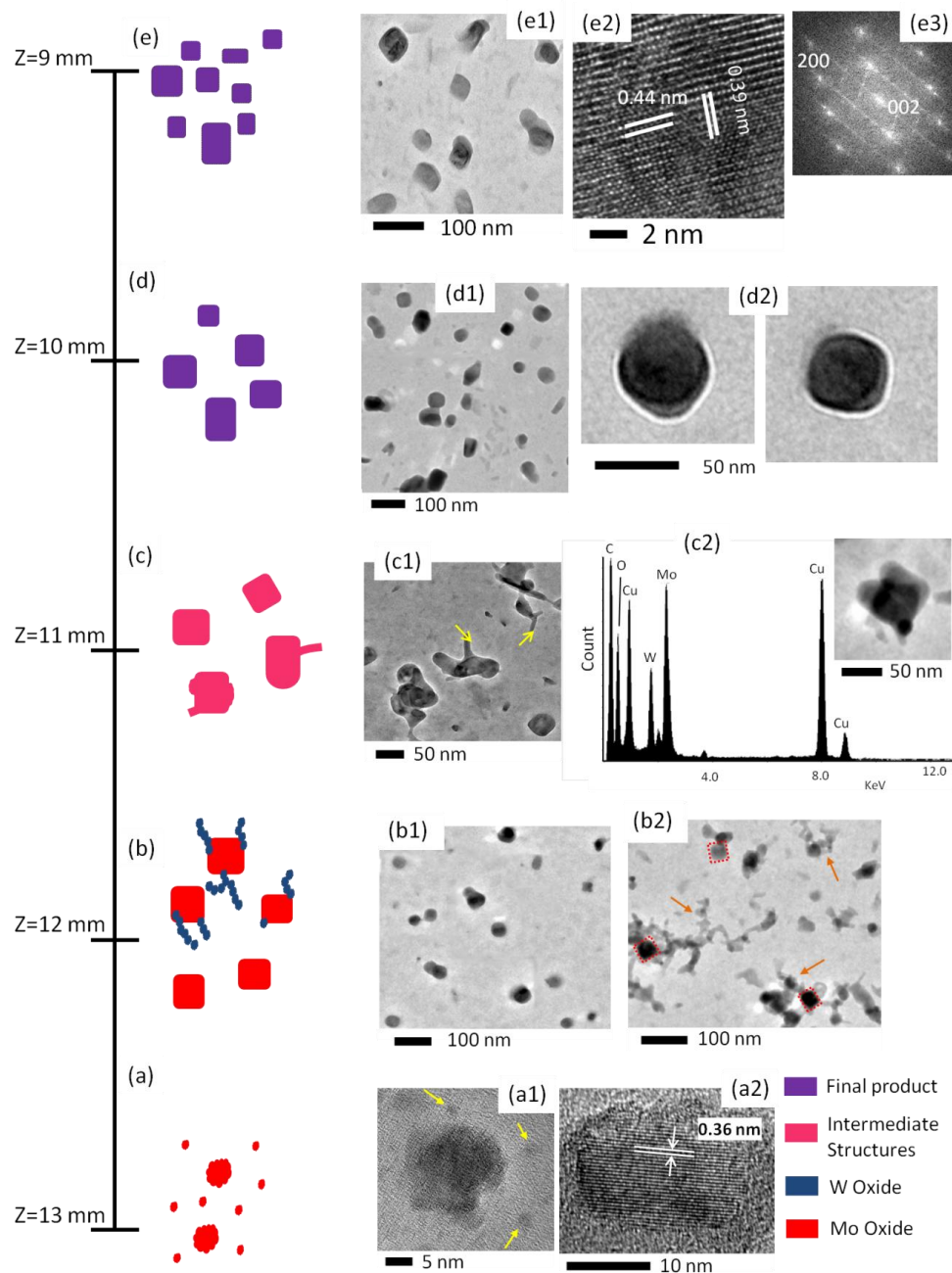
Figure 5-9- Growth mechanism of W-doped MoO_3 structures. (a) early formed MoO_3 vapors at Z=13 mm; (b) deposition of tungsten over MoO_3 nanocubes; (c) intermediate formed structures composed of tungsten and molybdenum and oxygen; (d) and (e) W-doped MoO_3 nanocubes.

At upper part of the flame, Z= 11 mm, chain-like structures turn to tale-like nanorods attached to sides of primary structures. Arrows indicate tale-like nanorods in figure 5-9c1. The EDS results show that structures at this position are composed of both Mo and W, figure 5-9c2. Carbon and copper reading are related to the TEM grid which is composed of copper and carbon film. It is believed that structures at this position are not fully-developed and can be called intermediate structures. Although few cubic structures can be observed, major of collected materials have not well-defined morphology.

Materials are carried in the flame volume and exposed to temperature and chemical gradient which lead into evolution in crystalline structure and morphology. As it can be seen in figure 5-9d1 structure once again transform to nanocubes. The smooth surface of the nanorods suggests that the influx of W(g) and formed tales are totally consumed/diffused on/into the surface of the existing nanocubes. Samples of cubic structures are shown in figure 5-9d2. Structures are grown continuously with high density in a way that cause change in the flame color (observation) and can be collected effortlessly with a micro suction pump through the flame volume. At upper positions (lower Z heights), more well-defined and discrete nanocubes can be observed. Cai et al. [170] grew W-doped MoO_3 at growth temperature over 350 ˚C and Baeck et al. [153] synthesized $W_{1-x}Mo_xO_3$ at 450 ˚C, the flame temperature is high enough to provide sufficient energy for formation of mixed W-Mo oxides. Also, low W concentration in mixed W-Mo oxide does not cause a change in the crystal phase (orthorhombic to monoclinic) [153]. Thus, evidences strongly suggest that grown structures are W-doped MoO_3 with low W:Mo ratio less than 0.1. Figure 5-9e1 shows cubes structures that can

be grown/collected at Z=9.0 mm. The HR-TEM and SAED images of collected/grown structures (figure 5-9e2 and 9e3) and EDS analysis (figure 5-7a and 9c2) closely match with W-doped MoO_3. From geometrical point of view, indeed, layered orthorhombic MoO_3 structures is preserved the three-dimensional structure during the course of reaction. Since the α-MoO_3 is a stable phase, it can be consider as the mother phase which does not change. In the gas-phase synthesis method, dopant (W) is introduced into existing nanocube crystals (in-situ doping), and it has minimum impact on the structures and keeps the crystallinity of the starting materials.

We can hypothesize that the following processes take place: (I) high temperature flame causes instantaneous evaporation/release of elemental molybdenum and combination of Mo with oxygen (from flame). Monomers and particles are formed by continuous influx of M/O molecules evaporated and/or sublimated due to flame high temperature; (II) shapeless particles transform to nanocubes as they travel inside the flame volume; (III) tungsten evaporated particles deposit on existing MoO_3 nanocubes and form chain-like tales attached to the nanocubes. Chain-like tales almost instantaneously diffuse into the nanocubes and elemental tungsten intercalate into layers of nanocubes structures; (IV) as nanocubes are carried inside the flame, elemental W distribute evenly inside structures and increase the lattice spacing of existing nanocubes. However, nanocubes maintain crystalline structure.
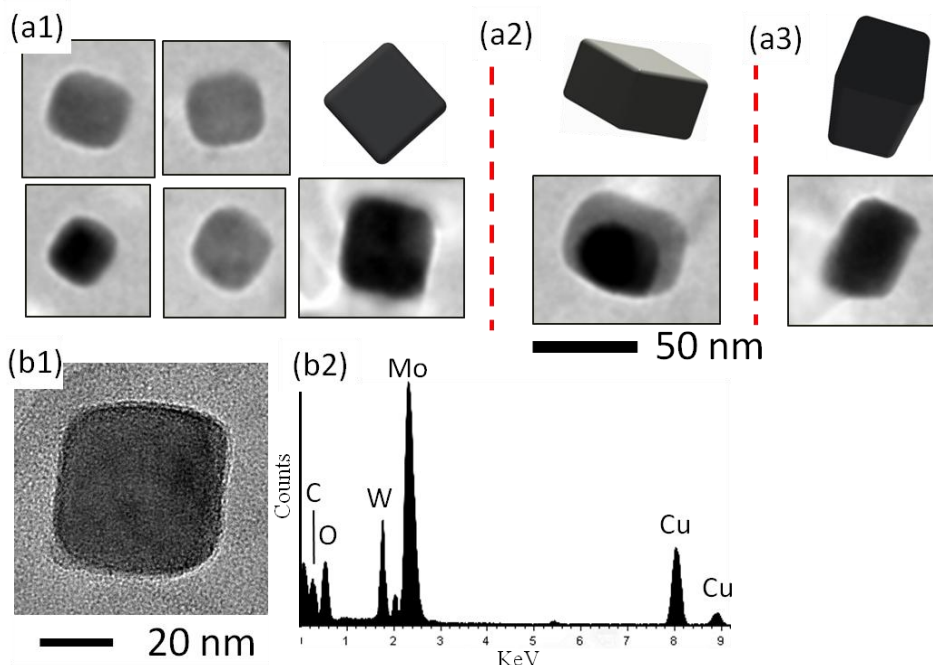
Figure 5-10- (a) Nanocube structures collected at Z= 9 mm and resembling computer generated images; (b) EDS analysis of the sample nanocube in (b1) indicates both elements of W and Mo.

Some samples of collected W-doped MoO_3 structures are shown figure 5-10a. The structures shown in the TEM image reveal an incomplete image of the true structures. To gain better understanding of true geometry, it is needed to rotate the TEM grid a few degrees to observe another side other than the side normal to the TEM beam. Computer generated images of nanocubes are rotated at different angles to reassemble and support the true shape of the various nanostructures presented in the TEM images of figure 5-10a. Nanocubes in figure 5-10a have all one side normal to the electron beam which makes it easier to interpret the true shape. However, structures in figure 5-10b and c require rotation to find their true shape. Darker part of the images might be due to thicker part of the structures. These images clearly indicate that all structures have width less than 50 nm. The EDS analysis of the nanocube shown in figure 5-10b reveals that the nanocube contains both W and Mo. All the EDS analyses show 20:1

101

weight ratio of Mo to W. The lower weight ratio along with change in lattice spacing confirms that as-grown mixed Mo and W oxide is W-doped MoO_3.

5-7- Chapter conclusions

Counter-flow flame is employed to synthesis W-doped MoO_3 in gas-phase. Mixed Mo-W oxides display improved performance in gas sensing, eletrochromic device, and lithium-ion batteries. High purity molybdenum and tungsten probes, 1 mm in diameter, are introduced to the flame at Z=14 mm and Z=12 mm, respectively. Materials are collected via thermophoretic sampling technique during evolution process as they travel towards stagnation plane inside the flame volume. Instantaneous evaporation/sublimation and combination with oxygen leads to formation of shapeless particles and subsequently nanocubes of MoO_3 near W probe. Tungsten particles deposit on surface of nanocubes and diffuse in layers of MoO_3 since required energy is provide by the high temperature flame. Fully grown structures, collected near the stagnation plane, are nanocube with well-defined edges in width of less than 100 nm. Smooth surface of nanocubes is evidence of complete diffusion/intercalation of tungsten into MoO_3 structures without destructing the morphology and crystalline structure of original material (α-MoO_3). The W-doped MoO_3 nanocubes can be grown through proposed single-step and inexpensively method continuously.

Electron Beam Induced Formation of Tungsten Sub-Oxide Nanorods from Flame-Formed Fragments[3]

6-1- Introduction

Vapor-phase growth mechanism has been observed in different synthesize methods such CVD, plasma, and flame. In order to continue the study on vapor-phase growth mechanism, in this chapter, growth of tungsten sub-oxide nanorods from flame-formed fragments is discussed. Previously, tungsten oxide nanostructure was grown using the flame method. However, growth of tungsten sub-oxide (WO_x, $0<x<1$) nanostructure requires a further step of reduction from oxide to sub-oxide. Low pressure (vacuum) along with excitation energy of electron beam provides a suitable condition for reduction and growth of nano-size structures. Electron beam energy causes evaporation/sublimation of source materials and formation of vapor particles, subsequently nanostructures are formed by collisions of vapor particles. The growth is very similar to the growth of nanostructurs through the flame synthesis. Thus, experiment procedure and in-detail growth mechanism of tungsten sub-oxides nanorods are investigated for the last chapter of this dissertation.

By scanning a focused electron-beam over a sample in the presence of a precursor (gas or solid), the pattern is defined directly and in principle no pre- or post-processing is required. It is mostly performed in electron microscopes (SEM and TEM), thus direct in situ inspection of the fabricated structure is simple. Since electron-beams can be focused into spots with diameters varying from the micrometer to sub-angstrom

---

[3] The content of this chapter is an extension of a published paper by the author. The paper contains results of research which was solely conducted as partial fulfillment for the PhD requirement. Materials presented in the paper have not been submitted for a course or extra credit.

level, this process is suitable for the micro- and nanometer regimes. Apart from deposition, the electron-beam can be employed to induce other effects such as heating or/and local etching. These processes are known as focused electron-beam induced processing [178].

Electron-beam irradiation is a promising technique to fabricate small-sized structures on substrates. Due to the easy controllability of the electron beam (EB), nanometer- or micrometer-sized 1D or 3D structures containing designed elements have been productively fabricated [179, 180]. The EB irradiation method incorporates the bombardment of highly excited electrons from a filament on the surface of deposited fragments. Through the electron beam irradiation process, electron bombardment can decompose material located on a surface into volatile and nonvolatile components. The volatile as-products are detached and pumped out the vacuum chamber, while the nonvolatile components are redeposit on a substrate. Precursor compounds, scanning parameters, beam conditions, and the pressure of the vacuum chamber influence the quality and species of deposited structures.

One-dimensional transition metal oxide micro/nanostructures have been investigated broadly due to their unique physical and chemical properties. Modeling and formation predication process of nanoparticles are presented [181, 182]. Nanostructures that have been fabricated employing EB induced deposition include tungsten, gold and platinum-containing nanotips and nanowires [183-186]. Among nanostructured TMOs, tungsten oxide (WO_3 and WO_2) and its suboxides (WO_{3-x} and WO_x) have wide applications such as electrochromic devices [187], electrocatalysts [188], information storage [189], and chemical sensors [190]. Because of high acidity of supported WO_x

on alumina, zirconia or titania are employed as catalysts for alcohol dehydrogenation, oxidative desulfurization and cracking of hydrocarbons [191, 192]. Commonly, gases such as tungsten hexafluoride (WF_6) and tungsten hexacarbonyl ($W(CO)_6$) are employed as precursors for the fabrication of tungsten and tungsten suboxide nanostructures by EB induced deposition [179, 193]. At present, various methods have been reported for fabrication of tungsten oxide nanostructures. However, methods capable of fabricating highly crystallized nanostructured tungsten sub-oxide (WO_x) have not been proposed.

In this study, we show the almost instantaneous formation of tungsten sub-oxide nanorods by subjecting flame-formed tungsten-oxide fragments (WO_3, WO_{3-x} and WO_2) to a convergent electron beam irradiation in a 200 keV transmission electron microscope. Individual tungsten sub-oxide nanorods are rapidly grown on the surface of the carbon film present on one side of a TEM grid as the flame-formed fragments are exposed to a focused EB. Also, the lengths of the formed nanorods can be approximately predicted as a function of the exposure time and distance between the fragments (irradiated spot) and nanorods.

6-2- Experimental details

The large-sized flame-formed fragments were grown on the surface of a W probe using a counter-flow combustion reactor. The formed micro-sized crystals or fragments are later exposed to an EB in order to transform them into 1D nanostructures. The burner forms a stable flame with a stagnation plane on the fuel side (figure 6-1a). Fuel ($96\%CH_4 + 4\%C_2H_2$) is injected from the top nozzle, and the oxidizer ($50\%O_2 + 50\%N_2$) is introduced from the bottom nozzle.

A 99.9% pure W probe with the diameter of 1.0 mm was inserted into the flame at 12 mm distance from the top nozzle. The probe was introduced in the oxygen rich zone (blue color) of the flame for approximately 2 minutes (figure 6-1a).

Scanning electron microscopy analyses on the oxidizer-side-faced surface of the probe shows the presence of no deposits. However, on the fuel-side-faced surface of the probe deposits of materials are evident to the naked eye. The surface of the W probe, facing the oxidizer side, is rapidly oxidized as it is exposed to a higher concentration of both atomic and molecular oxygen and temperature gradient than the surface of the probe facing the fuel side. Strong surface erosion is present on the oxidizer side of probe, primarily because of exposure to the high temperature (figure 6-1b). Different tungsten oxides (WO_{3-x}) continually formed and instantly evaporated from the oxidizer side of the probe. Then the W probe is withdrawn from the flame medium and a razor blade was used to scrape the surface of the probe facing the oxidizer side resulting in small fragments of materials. A suspension was formed containing methanol as a solvent and the removed fragments as the solute. The solution was sonicated for several minutes and a drop of the suspension was placed on the surface of a 3-mm lacey carbon film copper substrate TEM grid and dried.

The large flame-formed segments were exposed to transmission electron microscope electron beam irradiation (figure 6-1c-d). More detailed descriptions of the characteristics of the flame formed nanorods and micron-sized structures can be found in the literature [172, 194, 195].
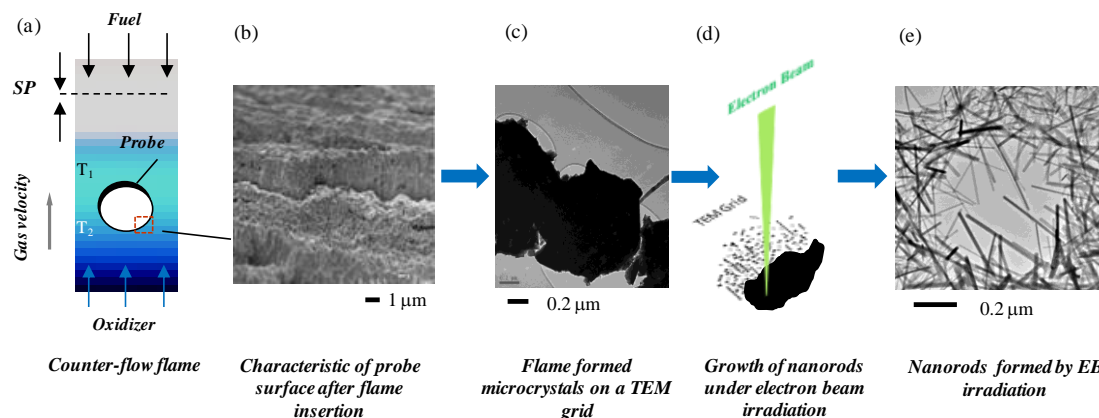
Figure 6-1- Formation of nanorods by electron beam irradiation from micron-sized flame-formed fragments; (a) insertion of a W probe inside a counter-flow flame; (b) SEM image of the surface characteristic of the probe facing the oxidizer side; (c) TEM image of a typical flame-formed fragment; (d) schematic of the formation of nanorods through the electron beam irradiation; (e) TEM image of the as-grown nanorods on the carbon film of the TEM grid.

The transmission electron microscope used in the experiments was JEOL2000FX (200 keV). The flame-formed fragment precursors only reacted to a highly intense electron beam. Electron beam irradiation of the flame-formed fragments at low magnification does not result in a noticeable growth or modification. In order to produce the nanorods, the EB was focused near the crossover to a spot size of approximately 500 nm and held over the fragment for a specified amount of time. Each time-step refers to the total amount of time that the tungsten oxide fragments were held under the EB at high intensity (115 pA/cm^2). Subsequently, the beam was amputated at the precursor fragments then expanded back to normal viewing intensity so images could be taken. Once the electron beam is focused on the surface of a tungsten oxide fragment, nanorods of remarkable high quality are instantaneously formed (figure 6-1e). This process was repeated until no further growth occurred. All experiments were performed at room temperature.

6-3- Results and discussion

It is well accepted that when a high-energy EB of an electron microscope passes through a sample, energy of electrons might partially transfer to the sample and augment the movement of atoms. If the intensity of EB passes above the threshold, the sample is usually disturbed. The beam disturbance usually causes displacement of atoms in a specimen, known as knock-on displacement. This structural modification can occur in a very short time to cause atomic defects [186]. Higher beam energy under ultrahigh vacuum in an electron microscope enhances atomic mobility in tungsten oxides, allowing rearrangement and/or improvement in crystallinity of deposited structures [179].

Figure 6-2 represents TEM images collected after a flame-formed tungsten-oxide fragment was exposed to an electron beam irradiation at various times. It can be observed that subjecting the surface of the large crystal fragment to an EB irradiation for a fraction of a second (~0.25 sec) resulted in the formation of mostly circular particles and very few short elongated structures (figures 2a1 and a2). By increasing the EB irradiation time to ~0.75 second the density and length of the produced nanocrystals significantly increased (figures 2b1 and b2).

A smaller increase in the density and growth of the nanorods is observed when the surface of the tungsten oxide fragments is exposed for an additional 2.30 seconds (figure 6-2c). The small interval of EB irradiation time on the surface of the flame-formed tungsten oxide fragments to form the precursors allowed for investigation of the growth rates of selected nanorods (figures 6-2a, b and c). Arrows 1, 2, 3, and 4 in figure 6-2a point to the early formed crystal nanorods. Arrows 1 and 2 (figure 6-2a2) point to

what appears to be the beginning of elongated structures of only a few nanometers in length after the EB irradiation of ~0.25 seconds. In the same TEM image, arrows 3 and 4 point to circular particles of a few nanometers in diameter. By increasing the EB irradiation time to ~0.75 seconds, the nanorods rapidly grew and reached lengths in the order of tens of nanometers as indicated by arrows 1 and 2 in figure 6-2b2. Furthermore, at the site where only circular particles were located (arrows 3 and 4 in figure 6-2a1), increased exposure time resulted in the formation of numerous elongated nanorods (figure 6-2b2). A further increase of the EB irradiation to ~2.30 seconds (~3 times the second EB irradiation) the lengths of the nanorods did not increase significantly but the increase in diameter of some of the structures is clearly visible (figure 6-2c2).
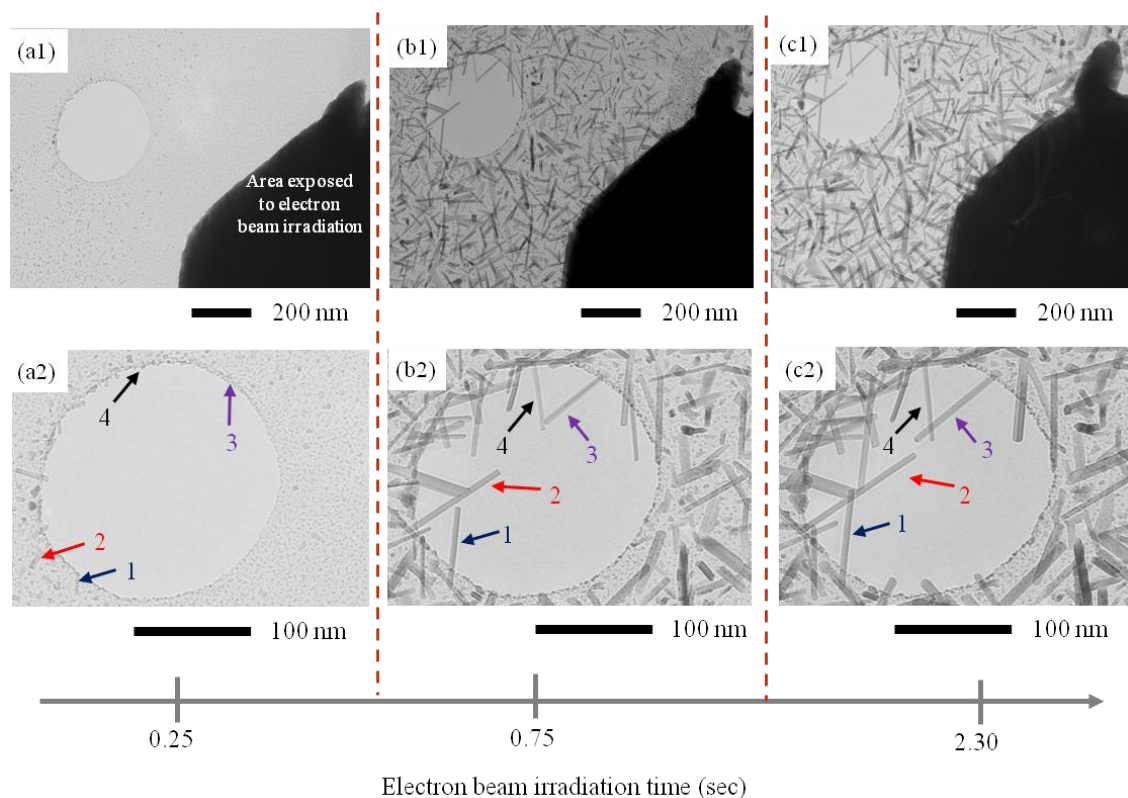
Figure 6-2- TEM images of W nanorods after precursor fragment was exposed to a concentrated EB for approximately: (a) 0.25s (b) 0.75s (c) 2.30s; Arrows indicate same nanorods grown under the EB.

Further characterization was performed with EDS combined with HR-TEM on as-produced nanorods. Figure 6-3 shows EDS spectra of corresponding grown materials before and after electron irradiation and also a HR-TEM image of a nanorod. Figure 6-3a shows EDS spectrum of selected area (inset) of a flame formed fragment.
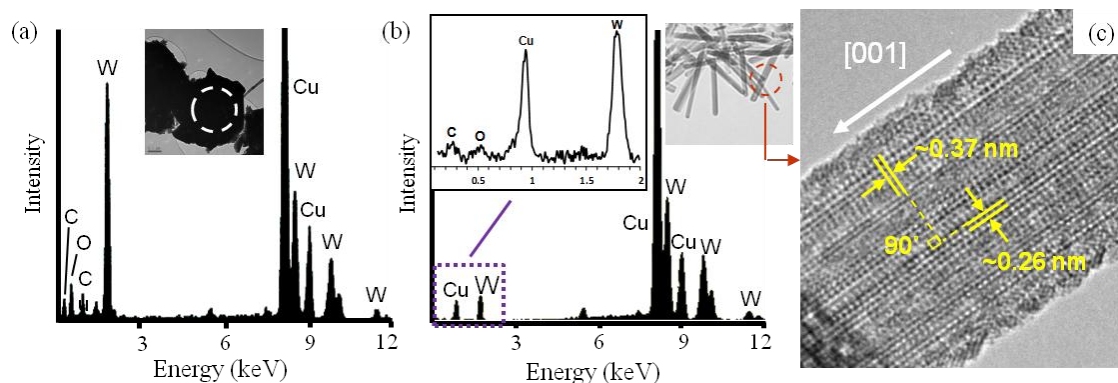
Figure 6-3- (a) EDS spectrum of the tungsten oxide structure before the electron irradiation; (b) EDS spectrum of as-produced lower state tungsten oxide nanorods; (c) HRTEM of tungsten oxide nanorods and preferred growth direction.

As it is shown in figures 6-3a and 3b, the oxygen ratio was significantly reduced in as-produced nanorods after EB irradiation, confirming the reduction of flamed formed tungsten oxide fragments to a lower oxygen state of tungsten oxide nanorods. The copper and carbon readings are attributed to the copper grid and carbon film, respectively. Figure 6-3c shows a HR-TEM image of an as-produced ordered nanorod with lattice spacing of 0.37 nm and 0.26 nm which closely corresponds to (001) and (200) of WO_x, respectively. The angle between the two planes is about 90˚. The representative HR-TEM image (figure 6-3c) indicates that grown nanorods have a preferential growth direction of [001]. The crystal structure is similar to nonstoichiometric tungsten oxide nanostructures [196]. Hence, all the evidence gathered by HRTEM and EDS is consistent with tetragonal WO_x.

In our experiments we observed that the length of the nanorods formed by EB irradiation greatly depends on the distance from the surface of the micro-sized fragments as evidenced in figure 6-4. Longer and thicker nanorods are present closer to the surface of the flame formed fragment. This was typical for every instance of nanorod formation. A semi-log plot of the length of nanorods (distributed logarithmically) versus distance from the surface of the source after 2.1 secs is shown in figure 6-4a. The TEM images in figure 6-4b were collected at $R_1 \approx 500$, $R_2 \approx 1000$, and $R_3 \approx 1500$ nm radial distances between the surface of fragments and nanorods. Under electron beam irradiation, it is well known that if the irradiated zone is considered to be the point source, the flux will be inversely proportional to the distance from the source [186].
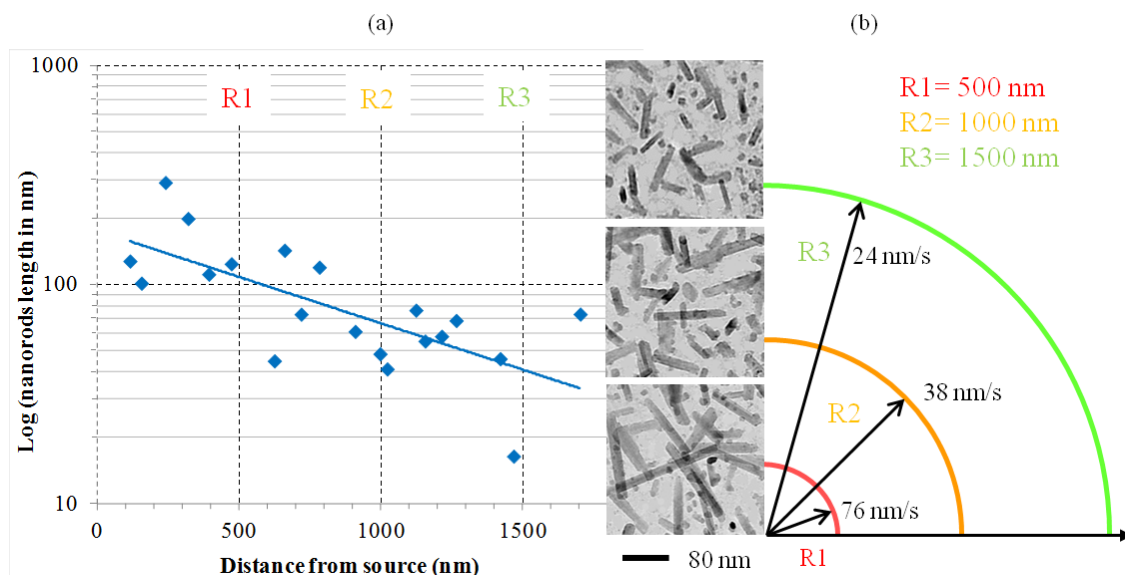
figure 6-4- (a) Exponential regression curve of length of nanorods as a function of distance from source after 2.1 seconds; (b) Growth rate and length of nanorods formed at different distances from the precursor.

The nanorods have average lengths decreasing from ~160, 82 and 52 nm at distances from the source of 500, 1000 and 1500 nm, respectively, verifying that lengths

of the nanorods continuously decrease with increasing distance from the source of particle flux (figure 6-4a). The growth rate of nanorods at a distance of ~500 nm from the surface of a precursor fragment to the nanorods is approximately 2 and 3 times higher than that of nanorods at distances of 1000 and 1500 nm from the surface of the fragmental precursor, respectively (figure 6-4b). Larger nanorods of ~200 nm long are grown near the precursor fragment and only ultra-small particles as small as 5 nm are present 2 µm away from the surface of the precursor.

The length of the nanorods as a function of EB irradiation time of the surface of the flame formed tungsten oxide microcrystals was also studied. Figure 6-5 represents TEM images collected at 0.1, 0.6, 1.1 and 180 seconds after EB irradiation time. Figure 6-2 shows a representative progression of structural morphology and size with EB irradiation times ranging from 0.25 to 2.30 seconds which all resulted in an increase in the lengths of the nanorods. The exposure of the EB to the precursor fragment for ~0.1 sec resulted in a high density of spherical particles (figure 6-5a). The almost instant appearance of these particles shows short incubation time (the time required by the specimen to show visible nucleus) required for crystallization [197]. The increase of the EB irradiation time on the surface of same fragment to ~0.6 sec resulted in significant modification of the morphology of the grown structures in which circular particles transform into elongated structures. A significant change in density of the zero-dimensional particles (seeds) to one-dimensional nanorods after a second short EB irradiation time is very evident, figures 6-5a-b. After an EB irradiation time of ~1.1 seconds it can be observed that there is no significant change in the density of the nanorods (figure 6-5c) and the lengths of the nanorods increased only by a small

fraction. Finally, a further increase in the EB irradiation time to ~180 secs did not result in a significant increase in length or density of the rods (figure 6-5d).
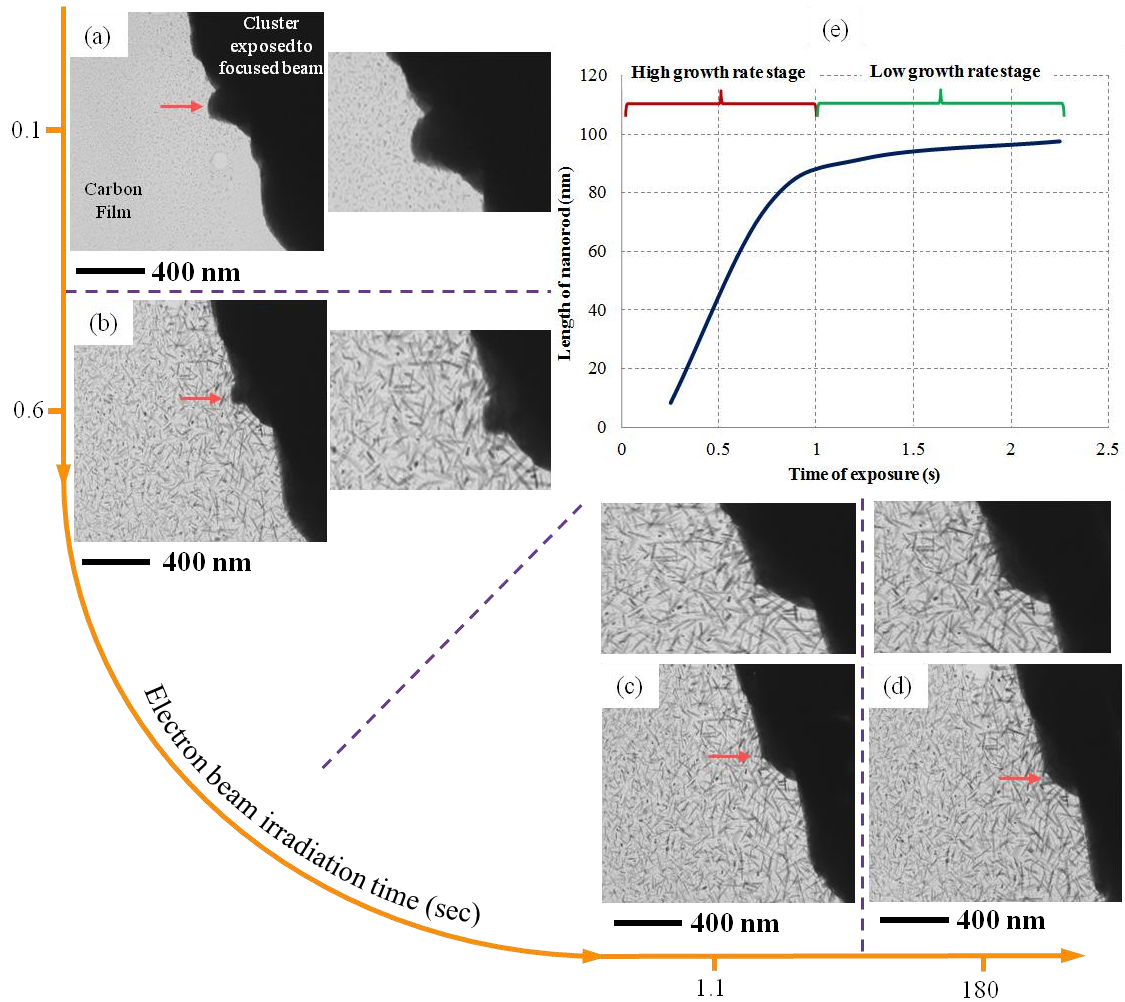
Figure 6-5- Tracking growth of nanorods over time. TEM images of tungsten oxide nanorods after the flame formed fragment was exposed to the concentrated EB for approximately: (a) 0.1s; (b) 0.6s; (c) 1.1s; (d) 180s; (e) variation of nanorod growth rate with applied EB irradiation.

The plot in figure 6-5e shows growth rate of the nanorods as a function of irradiation time. The experimental results suggest that an increase in EB irradiation of less than one second generates a linear growth increase of nanorods. That is, the tungsten oxide nanorods reach ~90% of their final length within approximately one second of EB irradiation. This is due to high flux of the reduced tungsten oxide and

rapid deposition after the initial irradiation. High flux of deposited tungsten oxides at this stage results in a growth rate of ~80 nm/s. However after one second, the nanorods grow at a lower rate of ~13 nm/s (figures 6-5c and 5d). As shown in figure 6-5e, the growth rate after a short amount of time (~two seconds) is negligible.

A study conducted by Shen et al. [186] showed that $W_{18}O_{49}$ nanorods with lengths of ~80 nm were produced after a 30 second EB irradiation. In the present work, EB irradiation (within one second) of the surface of flame-formed precursor fragments produces WO_x nanorods with lengths of ~80 nm. In our experiments, the precursors were formed using a high flame temperature environment. The almost instantaneous growth of the nanorods from fragments are principally due to the considerable amount of residual stresses attained in the material as they are formed in a high flame temperature environment [197].

It is also evident that as the EB exposure time increases on the flame formed tungsten oxide fragment to produce nanorods, a significant change in the shape of the surface of the fragment occurs as highlighted by the arrows in figure 6-5a-d. The surface of the fragment is originally composed of indentations and small grains but becomes smooth and flat as the EB irradiation time is increased. The arrow in figure 6-5 points to a notch that virtually disappears as the EB time is increased. The first process involves the formation of the tungsten oxide fragments using a counter-flow flame. The micron-sized fragments, which serve as the precursors to the nanorods, were created on the surface of a cylindrical probe introduced in the oxygen zone containing strong temperature and chemical gradients.

6-4- Proposed growth mechanism for the nanorods

The growth mechanism of the nanorod formation through EB irradiation is discussed. To gain insights into a possible growth mechanism of the nanorods by the EB irradiation, HR-TEM images were collected after the micro-sized fragments were exposed to various EB irradiation times.

The possible consequences of irradiation with high-energy electrons are small thermal effect, bond breaking, knock-on-collisions (atomic displacement), and creation of electron-hole pairs (for semiconductors materials). Thus, the EB might promote atomic mobility [197]. If transferred energy from the EB exceeds displacement threshold energy, displacement atomic nuclei to interstitial positions can occur. This effect is commonly observed in TEMs [198].

In the present work, the flame-formed tungsten-oxide fragments were held under the electron beam of a TEM operating at intensity of 115 pA/cm^2. A short EB irradiation time of ~0.25 seconds results in the formation of a high density of small shapeless and spherical crystal nanostructures on the surface of the grid (figure 6-6a). The diameter of the spherical particles is less than a few nanometers and they are very transparent to the electron beam (figure 6-6a1). These newly generated particles coalesce and deposit on the copper grid to form seeds for further nanostructure growth. It is also very interesting to note the high density of the small particles that are present within the larger structures as highlighted by solid black arrows in figures 6-6b1 and 6b2. The presence of the shapeless small particles accompanying the larger structures is evident. It appears that small particles are the building blocks for the formation of the elongated nanorods. The TEM images in figures 6-6b1 and 6b2 show the presence of an

115

early formation of elongated structures surrounded by a high density of individual spherical structures (solid white arrows). A close inspection clearly shows that the elongated structures are composed of a number of individual spherical particles, dashed black arrows in figures 6-6b1 and 6b2. The presence of distinct morphologies within a single nanorod is evident. One section of the nanorod appears to have uniform and well defined diameter (dotted black arrows) while the other section of the rod appears to be less defined composed of link-like chain particles that are fused together (dashed black arrows).

The physical characteristics of the less defined section of the nanorods resemble those of the surrounding particles suggesting that they are the basis for the formation of the nanorods. The confirmed hypothesis is that once a site is formed, a continuous influx of W/O(g) is consumed or nucleated on the surface of the seeds to grow in a preferable direction forming the nanorods. This effect is particularly evident in two of the selected structures highlighted by arrows 2 and 3, in figures 6-2b2 and 2c2. The surfaces of the structures in figures 6-2b2 and 2c2 are very smooth and no evidence of attached spherical-like particles is present after the structures grow tens of nanometers through the EB irradiation. The smooth surface of the nanorods suggests that the influx of W/O(g) is totally consumed/diffused on/into the surface of the existing nanorods. The selective growth of elongated crystals occurs through preferred materials deposition on the tips of the growing nanorods where the bonding energy is high which is typical of crystal growth. In figure 6-6b1 it can be observed that an individual spherical particle is attached to the tip of a developed nanorod as pointed out by the dotted white arrow. Other surrounding nanorods appear to have the same characteristics. Figure 6-6c2

represents a HR-TEM of a nanorod and spherical-like structure interface, arrow in figure 6-6c1. The necking effect between the particle and the rod is very evident as pointed out by the arrow in figure 6-6c2. The atomic structure of both the nanorod and attached spherical-like structure is well-organized, figure 6-6c2. It appears that the nanorod and sphere are fused together. A necking effect is also observed in some of the formed nanorods (arrows in inset figure 6-6c2). When the high-energy EB passes through the flame-formed tungsten oxide fragments, it creates electron-hole pairs which can effectively reduce the melting temperature. Consequently, a small increase in localized temperature causes the fragments to evaporate or sublime and simultaneously decompose leading to release of elemental oxygen and tungsten. Furthermore, the temperature required for melting materials in the micro- and nano-scale range is significantly less than their bulk counterparts. Great decrease (almost 60%) in melting temperatures have been stated for the nano-size particles compared to that of bulk materials [70, 199]. The decomposition of tungsten oxides and release of the elements can be further attributed to the removal of oxygen induced by core-hole Auger decay [200, 201]. Moreover, it has been reported that reductive decomposition of tungsten oxide can occur in the low oxygen pressure environment of the TEM ($\sim 10^{-7}$ Torr) at high temperature ($\sim 650°C$) [193, 202]. A substantial amount of decomposed oxygen is constantly vacuumed in the high-vacuum electron microscope column. The vacuum column brings about oxygen deprivation and, as a result, the tungsten oxide formed would have a lower oxidation state than the fragment precursors. Therefore, the nanorods synthesized are likely to be oxygen reduced.
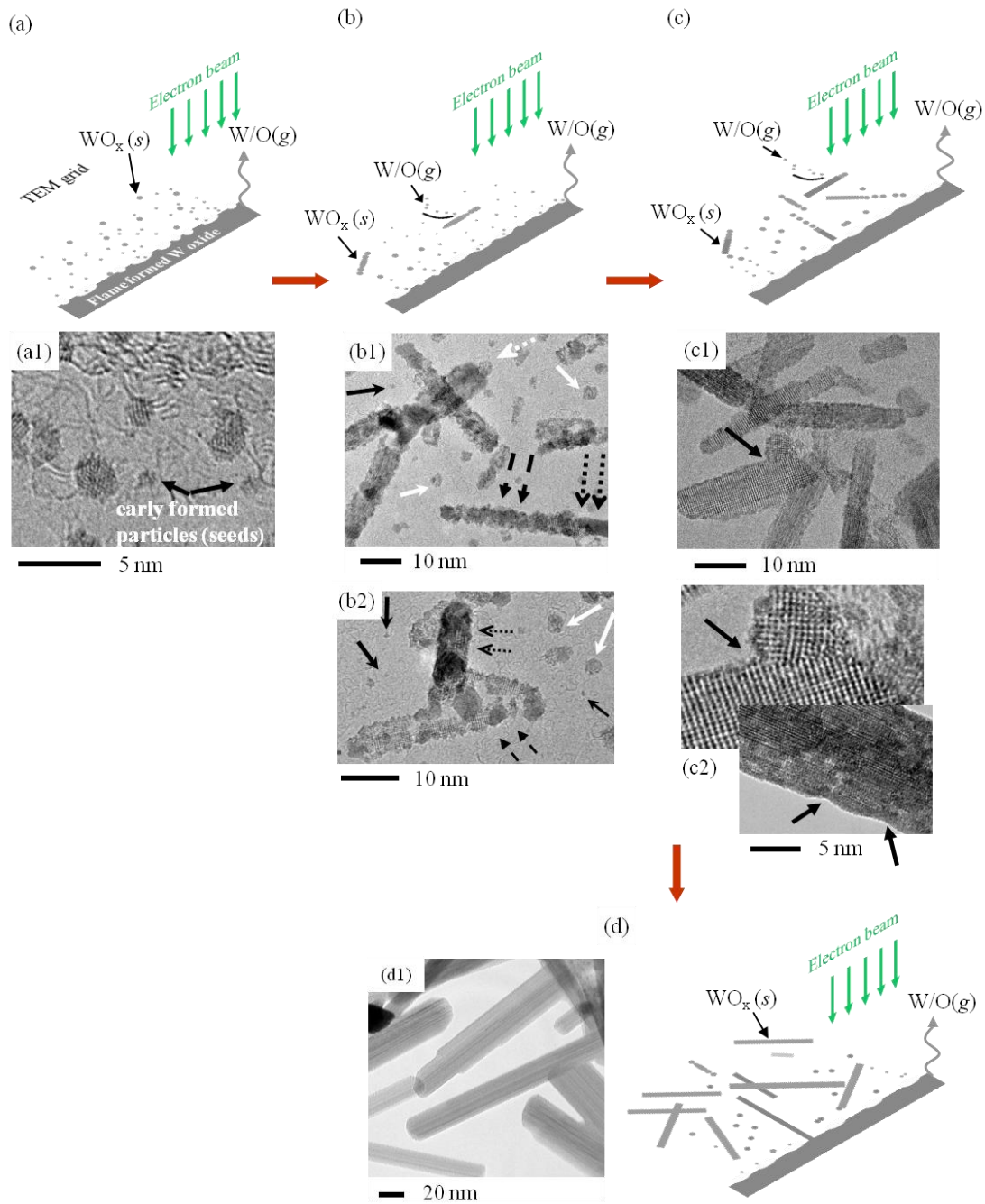
Figure 6-6- Schematics and supportive TEM images of the proposed growth mechanism of nanorods due to electron beam irradiation; (a) formation of small particle (early stage); (b) nucleation and recombination of the ultra-small particles to nanorods; (c) formation of tungsten sub-oxide nanorods; (d) fully formed tungsten oxide nanorods.

We can hypothesize that the following processes take place: (I) as the concentrated EB passes through the flame-formed fragments, elemental oxygen and tungsten are instantaneously released. Ultra-small size particles are formed by the

118

nucleation of the W/O molecules evaporated and/or sublimated due to EB irradiation; (II) in the very high vacuum environment as the elements travel, they nucleate/recombine/aggregate to form small discrete shapeless seeds; and (III) once the seeds are formed and as the influx of WO_x and/or elemental W and O continue to be supplied due to the EB irradiation, they can be completely consumed/diffused at the tip of existing solid structures resulting in longer nanorods.

It is noteworthy that the temperature of the growing environment changes; it is higher during EB irradiation and lower as the seeds travel and deposit further away from the EB irradiated spot. The gas-to-solid conversion is evident within the formed structures.

The effect of cooling, solidification, and crystallization process in the structures is apparent from our TEM analysis in figure 6-6 where some of the particles appear to cool, solidify, and crystallize before they were completely diffused and consumed into the surface of the existing rods. Experiments conducted at longer EB irradiation times showed that no significant change in density and length of the nanorods occurs. Furthermore, a significant amount of the fragments (source materials) remained after the longer EB irradiation. This is due to the fact that the remaining material is composed of more stable material such as WO_3 since it can be relatively stable under an intense electron beam [186]. The results of stable material correlates well with our flame formed WO_3 nanorods where no changes in morphology of the rods occurred during the structural and chemical characterization with low and HR-TEM.

6-5- Chapter conclusions

We report the electron beam induced growth of tungsten sub-oxide nanorods. Tungsten oxides precursor fragments were grown in a counter-flow flame environment on the surface of a high purity tungsten probe. The precursors were exposed to a high intensity electron beam that resulted in the growth of tungsten sub-oxide nanorods of various lengths and aspect ratios. The electron beam irradiation over the flame formed fragments lead to decomposition of the precursor and formation of tungsten oxide nanorods with lower state oxygen. Early formed ultra-small sized particles were the seed for growth of 1-D nanorods under the irradiation. The growth rate of nanorods is an exponential function of their distance to the irradiated spot i.e. the higher growth rate was achieved closer to the precursor cluster. Longer nanorods are observed closer to the irradiated spot. Electron beam irradiated growth using an in-situ flame-formed precursor offers a way to produce nanorods of a desired length locally and very rapidly by controlling the distance to the precursor and time of irradiation.

Recommendations for future work

Feasibility of synthesizing metal oxide nanostructures inside the flame has been fully investigated at this point. Following recommendation are made for future studies:

1- Studying the mechanical and electrical properties is proposed to be conducted. Characteristic and properties and flame grown material have not been compared with materials grown with different methods.

2- Aligned and uniform nanostructures are the most desirable form for applications. Producing aligned nanostructures are more expensive and finding a way to reduce the production cost is proposed to be investigated in the future.

3- Although experimental observation and proposed growth mechanism have been studied by several researchers, theoretical investigation on growth of metal oxide nanostructures inside the flame has not been carried out thoroughly. Numerical computer code that can predict the growth and morphology of nanostructure at different conditions (source material, environment temperature and oxygen content) reduces production cost which is desirable for industry.

References

[1] M. Cahay, J.P. Leburton, D.J. Lockwood, S. Bandyopadhyay, J.S. Harris, Quantum confinement VI: nanostructured materials and devices, The electrochemical Society, Pennington, New Jersey, 2001.

[2] E. Comini, C. Baratto, G. Faglia, M. Ferroni, A. Vomiero, G. Sberveglieri, Quasi-one dimensional metal oxide semiconductors: Preparation, characterization and application as chemical sensors, Prog. Mater. Sci., 54 (2009) 1-67.

[3] G. Malandrino, S.T. Finocchiaro, R.L. Nigro, C. Bongiorno, C. Spinella, I.L. Fragalà, Free-standing copper(II) oxide nanotube arrays through an MOCVD template process, Chem. Mater., 16 (2004) 5559-5561.

[4] Z. Liu, D. Zhang, S. Han, C. Li, T. Tang, W. Jin, X. Liu, B. Lei, C. Zhou, Laser ablation synthesis and electron transport studies of tin oxide nanowires, Adv. Mater., 15 (2003) 1754-1757.

[5] Z.R. Dai, Z.W. Pan, Z.L. Wang, Novel nanostructures of functional oxides synthesized by thermal evaporation, Adv. Funct. Mater., 13 (2003) 9-24.

[6] R.S. Wagner, W.C. Ellis, Vapor-liquid-solid mechanism of single crystal growth, Appl. Phys. Lett., 4 (1964) 89-90.

[7] Q. Zhao, X. Xu, H. Zhang, Y. Chen, J. Xu, D. Yu, Catalyst-free growth of single-crystalline alumina nanowire arrays, Appl. Phys. A, 79 (2004) 1721-1724.

[8] A. Sekar, S.H. Kim, A. Umar, Y.B. Hahn, Catalyst-free synthesis of ZnO nanowires on Si by oxidation of Zn powders, J. Cryst. Growth, 277 (2005) 471-478.

[9] Y. Sun, G.M. Fuge, M.N.R. Ashfold, Growth mechanisms for ZnO nanorods formed by pulsed laser deposition, Superlattices Microstruct., 39 (2006) 33-40.

[10] J.M. Blakely, K.A. Jackson, Growth of crystal whiskers J. Chem. Phys., 37 (1962) 428-431.

[11] Y. Xia, P. Yang, Y. Sun, Y. Wu, B. Mayers, B. Gates, Y. Yin, F. Kim, H. Yan, One-dimensional nanostructures: synthesis, characterization, and applications, Adv. Mater., 15 (2003) 353-389.

[12] X.M. Liu, Y.C. Zhou, Electrochemical deposition and characterization of Cu_2O nanowires, Appl. Phys. A, 81 (2005) 685-689.

[13] Y.W. Chen, Y.C. Liu, S.X. Lu, C.S. Xu, C.L. Shao, C. Wang, J.Y. Zhang, Y.M. Lu, D.Z. Shen, X.W. Fan, Optical properties of ZnO and ZnO:In nanorods assembled by sol-gel method, J. Chem. Phys., 123 (2005) 134701-134706.

[14] X. Wang, X. Wang, W. Huang, P.J. Sebastian, S. Gamboa, Sol-gel template synthesis of highly ordered MnO_2 nanowire arrays, J. Power Sources, 140 (2005) 211-215.

[15] L.I. Stepanova, L.S. Ivashkevich, G.A. Branitskii, Hydrothermal synthesis of tungsten molybdenum mixed oxides, Russ. J. Inorg. Chem., 54 (2009) 1553-1558.

[16] D.-S. Kang, S.K. Han, J.-H. Kim, S.M. Yang, J.G. Kim, S.-K. Hong, D. Kim, H. Kim, J.-H. Song, ZnO nanowires prepared by hydrothermal growth followed by chemical vapor deposition for gas sensors, J. Vac. Sci. Technol. B, 27 (2009) 1667-1673.

[17] J. Qiu, X. Li, W. He, S.J. Park, H.K. Kim, Y.H. Hwang, J.H. Lee, Y.D. Kim, The growth mechanism and optical properties of ultralong ZnO nanorod arrays with a high aspect ratio by a preheating hydrothermal method, Nanotechnology, 20 (2009) 155603.

[18] R. Strobel, S.E. Pratsinis, Flame aerosol synthesis of smart nanostructured materials, J. Mater. Chem., 17 (2007) 4743-4756.

[19] S. Thybo, S. Jensen, J. Johansen, T. Johannessen, O. Hansen, U.J. Quaade, Flame spray deposition of porous catalysts on surfaces and in microsystems, J. Catal., 223 (2004) 271-277.

[20] K.C. Patil, S.T. Aruna, S. Ekambaram, Combustion synthesis, Curr. Opin. Solid State Mater. Sci., 2 (1997) 158-165.

[21] S.T. Aruna, A.S. Mukasyan, Combustion synthesis and nanomaterials, Curr. Opin. Solid State Mater. Sci., 12 (2008) 44-50.

[22] R.A. Dobbins, C.M. Megaridis, Morphology of flame-generated soot as determined by thermophoretic sampling, Langmuir, 3 (1987) 254-259.

[23] W. Merchan-Merchan, S.G. Sanmiguel, S. McCollam, Analysis of soot particles derived from biodiesels and diesel fuel air-flames, Fuel, 102 (2012) 525-535.

[24] A.M. Taylor, in: Aerospace and Mechanical Engineering, University of Oklahoma, Norman, 2008.

[25] C.J. Sung, J.B. Liu, C.K. Law, Structural response of counterflow diffusion flames to strain rate variations, Combust. Flame, 102 (1995) 481-492.

[26] J. Thangala, S. Vaddiraju, S. Malhotra, V. Chakrapani, M.K. Sunkara, A hot-wire chemical vapor deposition (HWCVD) method for metal oxide and their alloy nanowire arrays, Thin Solid Films, 517 (2009) 3600-3605.

[27] V. Levitin, High temperature strain of metals and alloys: Physical fundamentals, Wiley-VCH, Weinheim, 2006.

[28] K. Arshak, G. Hickey, J. Harris, E. Forde, in: Sensors Applications Symposium, IEEE, Atlanta, GA 2008, pp. 187-192.

[29] M.A. Aegerter, Sol–gel niobium pentoxide: A promising material for electrochromic coatings, batteries, nanocrystalline solar cells and catalysis, Sol. Energy Mater. Sol. Cells, 68 (2001) 401-422.

[30] N. Uekawa, T. Kudo, F. Mori, Y.J. Wu, K. Kakegawa, Low-temperature synthesis of niobium oxide nanoparticles from peroxo niobic acid sol, J. Colloid Interface Sci., 264 (2003) 378-384.

[31] S.-J. Kim, B.J. Cho, M.B. Yu, M.-F. Li, Y.-Z. Xiong, C. Zhu, A. Chin, D.-L. Kwong, Metal-insulator-metal RF bypass capacitor using niobium oxide (Nb_2O_5) with HfO_2/Al_2O_3 barriers, IEEE Electron Device Lett., 26 (2005) 625 - 627

[32] H. Lin, S. Jiang, J. Wu, F. Song, N. Peyghambarian, E.Y.B. Pun, Er^{3+} doped $Na_2O–Nb_2O_5–TeO_2$ glasses for optical waveguide laser and amplifier, J. Phys. D: Appl. Phys., 36 (2003) 812–817.

[33] F. Lai, M. Li, H. Wang, H. Hu, X. Wang, J.G. Hou, Y. Song, Y. Jiang, Optical scattering characteristic of annealed niobium oxide films, Thin Solid Films, 488 (2005) 314-320.

[34] A.L. Viet, M.V. Reddy, R. Jose, B.V.R. Chowdari, S. Ramakrishna, Nanostructured Nb_2O_5 polymorphs by electrospinning for rechargeable lithium batteries, J. Phys. Chem. C, 114 (2010) 664-671.

[35] M. Paulis, M. Martín, D.B. Soria, A. Díaz, J.A. Odriozola, M. Montes, Preparation and characterization of niobium oxide for the catalytic aldol condensation of acetone, Appl. Catal. A: Gen, 180 (1999) 411-420.

[36] B. Varghese, S.C. Haur, C.-T. Lim, Nb_2O_5 nanowires as efficient electron field emitters, J. Phys. Chem. C, 112 (2008) 10008–10012.

[37] C.O. Avellaneda, A. Pawlicka, M.A. Aegerter, Two methods of obtaining sol–gel Nb_2O_5 thin films for electrochromic devices, J. Mater. Sci., 33 (1998) 2181-2185.

[38] P. Viswanathamurthi, N. Bhattarai, H.Y. Kim, D.R. Lee, S.R. Kim, M.A. Morris, Preparation and morphology of niobium oxide fibres by electrospinning, Chem. Phys. Lett., 374 (2003) 79-84.

[39] J.H. Lim, G. Park, J. Choi, Synthesis of niobium oxide nanopowders by field-crystallization-assisted anodization, Curr. Appl Phys., 12 (2012) 155-159.

[40] J. Choi, J.H. Lim, J. Lee, K.J. Kim, Porous niobium oxide films prepared by anodization–annealing–anodization, Nanotechnology, 18 (2007) 055603.

[41] K. Hara, T. Horiguchi, T. Kinoshita, K. Sayama, H. Sugihara, H. Arakawa, Highly efficient photon-to-electron conversion with mercurochrome-sensitized nanoporous oxide semiconductor solar cells Sol. Energy Mater. Sol. Cells, 64 (2000) 115-134.

[42] S.A. O'Neill, I.P. Parkin, R.J.H. Clark, A. Mills, N. Elliott, Atmospheric pressure chemical vapour deposition of thin films of Nb2O5 on glass, J. Mater. Chem., 13 (2003) 2952-2956

[43] R.L. Karlinsey, Preparation of self-organized niobium oxide microstructures via potentiostatic anodization, Electrochem. Commun., 7 (2005) 1190-1194.

[44] M. Mozetič, U. Cvelbar, M.K. Sunkara, S. Vaddiraju, A method for the rapid synthesis of large quantities of metal oxide nanowires at low temperatures, Adv. Mater., 17 (2005) 2138–2142.

[45] U. Cvelbar, M. Mozetič, Behaviour of oxygen atoms near the surface of nanostructured Nb2O5, J. Phys. D: Appl. Phys., 40 (2007) 2300-2303.

[46] M.E. Gimon-Kinsel, K.J.B. Jr., Pulsed laser deposition of mesoporous niobium oxide thin films and application as chemical sensors, Microporous Mesoporous Mater., 28 (1999) 113-123.

[47] K. Teo, C. Singh, M. Chhowalla, W.M. WI, Catalytic synthesis of carbon nanotubes and nanofibers in: H.S. Nalwa (Ed.) Encyclopedia of Nanoscience and Nanotechnology, American Scientific Publishers, 2004.

[48] A. Dabirian, Y. Kuzminykh, S. Harada, C. Parsons, S.C. Sandu, E. Wagner, G. Benvenuti, S. Rushworth, P. Muralt, P. Hoffmann, in: IOP Conf. Series: Materials Science and Engineering, IOP Publishing, 2010, pp. 012026.

[49] A. Pawlicka, M. Atik, M.A. Aegerter, Synthesis of Nb2O5 thin films for electrochromic devices, J. Mater. Sci. Lett., 15 (1995) 1568-1570.

[50] I. Sieber, H. Hildebrand, A. Friedrich, P. Schmuki, Formation of self-organized niobium porous oxide on niobium, Electrochem. Commun., 7 (2005) 97-100.

[51] S. Yang, H. Habazaki, T. Fujii, Y. Aoki, P. Skeldon, G.E. Thompson, Control of morphology and surface wettability of anodic niobium oxide microcones formed in hot phosphate–glycerol electrolytes, Electrochim. Acta, 56 (2011) 7446-7453.

[52] M. Guenin, R. Frety, E. Garbowski, P. Vergnon, Characterization of niobium pentoxide prepared by flame reaction, J. Mater. Sci., 23 (1988) 1009-1013.

[53] R. Tomasi, Z.A. Munir, Effect of particle size on the reaction wave propagation in the combustion synthesis of Al_2O_3–ZrO_2–Nb composites, J. Am. Ceram. Soc., 28 (2004) 1985–1992.

[54] I.J. Shon, D.H. Rho, H.C. Kim, Z.A. Munir, Synthesis of WSi_2–ZrO_2 and WSi_2–Nb composites by field-activated combustion, J Alloy Compd, 327 (2001) 66-72.

[55] S.M. Zanetti, E.I. Santiago, L.O.S. Bulhoes, J.A. Varela, E.R. Leite, E. Longo, Preparation and characterization of nanosized $SrBi_2Nb_2O_9$ powder by the combustion synthesis, Mater. Lett., 57 (2003) 2812–2816.

[56] A. Teleki, N. Bjelobrk, S.E. Pratsinis, Flame-made Nb- and Cu-doped TiO_2 sensors for CO and ethanol, Sensor. Actuat. B, 130 (2008) 449–457.

[57] J.A. Nuetzel, C.J. Unrau, R. Indeck, R.L. Axelbaum, Flame synthesis of superparamagnetic Fe/Nb nanocomposites for biomedical applications, Proc. Combust. Inst., 32 (2009) 1871–1877.

[58] S. Phanichphant, C. Liewhiran, K. Wetchakun, A. Wisitsoraat, A. Tuantranont, Flame-made Nb-doped TiO_2 ethanol and acetone sensors, Sensors, 11 (2011) 472-484.

[59] C.L. Yeh, J.H. Chen, Combustion synthesis of $(Ti_{1-x}Nb_x)_2AlC$ solid solutions from elemental and Nb_2O_5/Al_4C_3-containing powder compacts, Ceram. Int., 37 (2011) 3089-3094.

[60] V. Kruefu, C. Liewhiran, C. Khantha, S. Phanichphant, in: 5th IEEE International Conference on Nano/Micro Engineered and Molecular Systems (NEMS), Chiang Mai, Thailand 2010, pp. 61 - 65

[61] C.R. Kachelmyer, A.S. Rogachev, A. Varma, Mechanistic and processing studies in combustion synthesis of niobium aluminides, J. Mater. Res., 10 (1995) 2260 - 2270

[62] S. Gedevanishvili, Z.A. Munir, Field-activated combustion synthesis in the Nb-Si system, Mater. Sci. Eng., A, 211 (1996) 1-9.

[63] M. Silvestrini, W. Merchan-Merchan, H. Richter, A. Saveliev, L.A. Kennedy, Fullerene formation in atmospheric pressure opposed flow oxy-flames, Proc. Combust. Inst., 30 (2005) 2545-2552.

[64] Y. Lin, Y.J. Yang, C.c. Hsu, Synthesis of niobium oxide nanowires using an atmospheric pressure plasma jet, Thin Solid Films, 519 (2011) 3043.

[65] C.C. Hsu, M.J. Titus, D.B. Graves, Measurement and modeling of time- and spatial-resolved wafer surface temperature in inductively coupled plasmas J. Vac. Sci. Technol. A, 25 (2007) 607.

[66] M.J. Titus, C.C. Hsu, D.B. Graves, "SensArray" voltage sensor analysis in an inductively coupled plasma, J. Vac. Sci. Technol. A, 28 (2009) 139.

[67] N.P. Bansal, Synthesis and thermal evolution of structure in alkoxide-derived niobium pentoxide gels J. Mater. Sci., 29 (1994) 4481-4486.

[68] W. Merchan-Merchan, A.V. Saveliev, M. Desai, Volumetric flame synthesis of well-defined molybdenum oxide nanocrystals, Nanotechnology, 20 (2009) 475601.

[69] W. Merchan-Merchan, A.V. Saveliev, W.C. Jimenez, Solid support flame synthesis of 1-D and 3-D tungsten-oxide nanostructures, Proc. Combust. Inst., 33 (2011) 1899-1908.

[70] W. Merchan-Merchan, A.V. Saveliev, L.A. Kennedy, Flame synthesis of molybdenum oxide whiskers, Chem. Phys. Lett., 422 (2006) 72-77.

[71] F. Holtzberg, A. Reisman, M. Berry, M. Berkenblit, Chemistry of the group VB pentoxides. VI. the polymorphism of Nb_2O_5, J. Am. Chem. Soc., 79 (1957) 2039–2043.

[72] D.W. Bridges, W.M. Fassell, High pressure oxidation of niobium J. Electrochem. Soc., 103 (1956) 326-330.

[73] Y. Ito, K. Kushida, K. Sugawara, H. Takeuchi, A 100-MHz ultrasonic transducer array using ZnO thin films Ultrasonics, Ferroelectrics and Frequency Control, IEEE 42 (1995) 316-324.

[74] K. Keis, E. Magnusson, H. Lindstrom, S.E. lindquist, A. Hagfeldt, A 5% efficient photoelectrochemical solar cell based on nanostructured ZnO electrodes, Sol. Energy, 73 (2002) 51-58.

[75] H. Yumoto, T. Inoue, S.J. Li, T. Sako, K. Nishiyama, Application of ITO films to photocatalysis, Thin Solid Films, 345 (1999) 38-41.

[76] Uedono A, Koida T, Tsukazaki A, Kawasaki M, Chen Z Q, Chichibu S F, K. H, Defects in ZnO thin films grown on ScAlMgO4 substrates probed by a monoenergetic positron beam, J. Appl. Phys., 93 (2003) 2481-2485.

[77] J.H. Lim, C.K. Kang, K.K. Kim, I.K. Park, D.K. Hwang, S.J. Park, UV electroluminescence emission from ZnO light-emitting diodes grown by high-temperature radiofrequency sputtering, Adv. Mater., 18 (2006) 2720–2724.

[78] Wei Z. P., Lu Y. M., Shen D. Z., Zhang Z. Z., Yao B., Li B. H., Zhang J. Y., Zhao D. X., Fan X. W., T.Z. K., Room temperature p-n ZnO blue-violet light-emitting diodes, Appl. Phys. Lett., 90 (2007) 042113-042113.

[79] S. Xiao-Ping, Y. Ai-Huan, H. Ye-Min, J. Yuan, X. Zheng, H. Zheng, Fabrication, characterization and field emission properties of large-scale uniform ZnO nanotube arrays, Nanotechnology, 16 (2005) 2039-2043.

[80] G.I. Dovbeshko, O.P. Pennytska, E.D. Obraztsova, Y.V. Shtogun, DNA interaction with single-walled carbon nanotubes: a SEIRA study, Chem. Phys. Lett., 372 (2003) 432-437.

[81] X.D. Bai, P.X. Gao, Z.L. Wang, E.G. Wang, Dual-mode mechanical resonance of individual ZnO nanobelts, Appl. Phys. Lett., 82 (2003) 4806-4809.

[82] W.L. Hughes, Z.L. Wang, Nanobelts as nanocantilevers, Appl. Phys. Lett., 82 (2003) 2886-2889.

[83] H.-W. Ryu, B.-S. Park, S.A. Akbar, W.-S. Lee, K.-J. Hong, Y.-J. Seo, D.-C. Shin, J.-S. Park, G.-P. Choi, ZnO sol–gel derived porous film for CO gas sensing, Sensor. Actuat. B-Chem., 96 (2003) 717-722.

[84] Q.H. Li, Q. Wan, Y.X. Liang, T.H. Wang, Electronic transport through individual ZnO nanowires, Appl. Phys. Lett., 84 (2004) 4556-4559.

[85] G.S.T. Rao, D.T. Rao, Gas sensitivity of ZnO based thick film sensor to NH$_3$ at room temperature, Sensor. Actuat. B-Chem., 55 (1999) 166-169.

[86] X.L. Cheng, H. Zhao, L.H. Huo, S. Gao, J.G. Zhao, ZnO nanoparticulate thin film: preparation, characterization and gas-sensing property, Sensor. Actuat. B-Chem., 102 (2004) 248-252.

[87] A. Kolmakov, M. Moskovits, Chemical sensing and catalysis by one-dimensional metal-oxide nanostructures, Annu. Rev. Mater. Res., 34 (2004) 151-180.

[88] Y. Gu, I.L. Kuskovsky, M. Yin, S. O'Brien, G.F. Neumark, Quantum confinement in ZnO nanorods, Appl. Phys. Lett., 85 (2004) 3833-3836.

[89] I. Shalish, H. Temkin, V. Narayanamurti, Size-dependent surface luminescence in ZnO nanowires, Phys. Rev. B, 69 (2004) 24401-24405.

[90] M.S. Arnold, P. Avouris, Z.W. Pan, Z.L. Wang, Field-effect transistors based on single semiconducting oxide nanobelts, J. Phys. Chem. B, 107 (2003) 659-663.

[91] W.I. Park, J.S. Kim, G.-C. Yi, M.H. Bae, H.J. Lee, Fabrication and electrical characteristics of high-performance ZnO nanorod field-effect transistors Appl. Phys. Lett., 85 (2004) 5052-5055.

[92] C. Li, G. Fang, N. Liu, J. Li, L. Liao, F. Su, G. Li, X. Wu, X. Zhao, Structural, photoluminescence, and field emission properties of vertically well-aligned ZnO nanorod arrays, J. Phys. Chem. C, 111 (2007) 12566-12571.

[93] Z. Guo, D. Zhao, D. Shen, F. Fang, J. Zhang, B. Li, Structure and Photoluminescence Properties of Aligned ZnO Nanobolt Arrays, Cryst. Growth Des., 7 (2007) 2294-22996.

[94] L. Vayssieres, Growth of Arrayed Nanorods and Nanowires of ZnO from Aqueous Solutions, Adv. Mater., 15 (2003) 464-466.

[95] C. Xu, Z. Liu, S. Liu, G. Wang, Growth of hexagonal ZnO nanowires and nanowhiskers, Scr. Mater., 48 (2003) 1367-1371

[96] Y.X. Chen, X.Q. Zhao, J.H. Chen, fault directed growth of thin ZnO nanobelt, Mater. Lett., 62 (2008) 2369-2371.

[97] P.X. Gao, Z.L. Wang, High-yield synthesis of single-crystal nanosprings of ZnO, Small, 1 (2005) 945–949.

[98] Z.L. Wang, X.Y. Kong, J.M. Zuo, Induced growth of asymmetric nanocantilever arrays on polar surfaces, Phys. Rev. Lett., 91 (2003) 185502.

[99] H.T. Ng, J. Li, M.K. Smith, P. Nguyen, A. Cassell, J. Han, M. Meyyappan, Growth of epitaxial nanowires at the junctions of nanowalls Science, 300 (2003).

[100] J.Y. Lao, J.Y. Huang, D.Z. Wang, Z.F. Ren, Hierarchical ZnO Nanostructures, Nano. Lett., 3 (2003) 235-238.

[101] X. Zhang, Y. Zhang, J. Xu, Z. Wang, X. Chen, D. Yu, P. Zhang, H. Qi, Y. Tian, Peculiar ZnO nanopushpins and nanotubes synthesized via simple thermal evaporation, Appl. Phys. Lett., 87 (2005).

[102] P.X. Gao, Y. Ding, W. Mai, W.L. Hughes, C. Lao, Z.L. Wang, Conversion of zinc oxide nanobelts into superlattice-structured nanohelices, Science, 309 (2005) 1700-1704.

[103] J.Y. Lao, J.Y. Huang, D.Z. Wang, Z.F. Ren, Hierarchical oxide nanostructures, J. Mater. Chem., 14 (2004) 770-773.

[104] R.T.R. Kumar, E. McGlynn, C. McLoughlin, S. Chakrabarti, R.C. Smith, J.D. Carey, J.P. Mosnier, M.O. Henry1, Control of ZnO nanorod array density by Zn supersaturation variation and effects on field emission Nanotechnology, 18 (2007) 1215704.

[105] P.-C. Chang, Z. Fan, D. Wang, W.-Y. Tseng, W.-A. Chiou, J. Hong, J.G. Lu, ZnO nanowires synthesized by vapor trapping CVD method, Chem. Mater., 16 (2004) 5133-5137.

[106] R. Yang, J. Zheng, W. Li, J. Qu, X. Zhang, X. Li, Low-temperature growth of ZnO nanostructures by oxygen plasma oxidation of $ZnCl_2$, Mater. Chem. Phys., 129 (2011) 693-695.

[107] S. Singh, R. Kumar, T. Ganguli, R.S. Srinivasa, S.S. Major, High optical quality ZnO epilayers grown on sapphire substrates by reactive magnetron sputtering of zinc target, J. Cryst. Growth, 310 (2008) 4640-4646.

[108] M.J. Height, L. Mädler, S.E. Pratsinis, Nanorods of ZnO made by flame spray pyrolysis, Chem. Mater., 18 (2006) 572-578.

[109] N. Tamaekong, C. Liewhiran, A. Wisitsoraat, S. Phanichphant, Flame-spray-made undoped zinc oxide films for gas sensing applications, Sensors, 10 (2010) 7863-7873.

[110] Y. Masuda, K. Kato, Aqueous synthesis of ZnO rod arrays for molecular sensor, Cryst. Growth Des., 9 (2009) 3083-3088.

[111] H. Saitoh, M. Satoh, N. Tanaka, Y. Ueda, S. Ohshio, Homogeneous growth of zinc oxide whiskers, Jpn. J. Appl. Phys., 38 (1999) 6973-6877.

[112] L. Znaidi, G.J.A.A.S. Illia, S. Benyahia, A.V.K. C. Sanchezb, Oriented ZnO thin films synthesis by sol-gel process for laser application, Thin Solid Films, 428 (2003) 257-262.

[113] Y. Zhang, N. Wang, S. Gao, R. He, S. Miao, J. Kiu, J. Zhu, X. Zhang, A simple method to synthesize nanowire, Chem. Mater., 14 (2002) 3564-3568.

[114] T. Tani, L. Madler, S.E. Pratsinis, Homogeneous ZnO nanoparticles by flame spray pyrolysis, J. Nanopart. Res., 4 (2002) 337-343.

[115] F. Xu, X. Liu, S.D. Tse, F. Cosandey, B.H. Kear, Flame synthesis of zinc oxide nanowires Chem. Phys. Lett., 449 (2007) 175-181.

[116] P. Kathirvela, J. Chandrasekaran, D. Manoharan, S. Kumar, Formation and characterization of flame synthesized hexagonal zinc oxide nanorods for gas sensor applications, Ceram. Int., 39 (2013) 5321-5325.

[117] N.L. Tarwal, P.R. Jadhav, S.A. Vanalakar, S.S. Kalagi, R.C. Pawar, J.S. Shaikh, S.S. Mali, D.S. Dalavi, P.S. Shinde, P.S. Patil, Photoluminescence of zinc oxide nanopowder synthesized by a combustion method, Powder Technol., 208 (2011) 185-188.

[118] A. Beltrame, P. Porshnev, W. Merchan-Merchan, A. Saveliev, A. Fridman, L.A. Kennedy, O. Petrova, S. Zhdanok, F. Amouri, O. Charon, Soot and NO formation in methane–oxygen enriched diffusion flames, Combust. Flame, 124 (2001) 295-310.

[119] H.B. Lu, L. Liao, H. Li, D.F. Wang, J.C. Li, Q. Fu, B.P. Zhu, Y. Wu, Well-aligned ZnO microprism arrays with umbrella-like tips: Low-temperature preparation, structure and UV photoluminescence improvement, Physica E, 40 (2008) 2931-2936.

[120] N.-K. Park, G.B. Han, J.D. Lee, S.O. Ryu, T.J. Lee, W.C. Chang, C.H. Chang, The growth of ZnO nano-wire by a thermal evaporation method with very small amount of oxygen, Curr. Appl Phys., 6S1 (2006) 176-181.

[121] X.N. Zhang, C.R. Li, Z. Z, Controlling the growth direction of one-dimensional ZnO nanostructures by changing the O content in reaction atmosphere, Appl. Phys. A, 82 (2006) 33-37.

[122] J. Zhang, Y. Yang, B. Xu, F. Jiang, J. Li, Shape-controlled synthesis of ZnO nano- and micro-structures, J. Cryst. Growth, 280 (2005) 509-515.

[123] D.H. Liu, L. Liao, J.C. Li, H.X. Guo, Q. Fu, Preparation and photoluminescence of ZnO nanostructures by thermal evaporation growth without catalysts, Mater. Sci. Eng., B, 121 (2005) 77-80.

[124] W.-J. Li, E.-W. Shi, W.-Z. Zhong, Z.-W. Yin, Growth mechanism and growth habit of oxide crystals, J. Cryst. Growth, 203 (1999) 186–196.

[125] F. Li, Z. Li, F. Jin, Fabrication and characterization of ZnO micro and nanostructures prepared by thermal evaporation, Physica B, 403 (2008) 664-669.

[126] R.T.R. Kumar, E. McGlynn, M. Biswas, R. Saunders, G. Trolliard, B. Soulestin, J.R. Duclere, J.P. Mosnier, M.O. Henry, Growth of ZnO nanostructures on Au-coated Si: Influence of growth temperature on grwoth mechanism and morphology, J. Appl. Phys., 104 (2008) 084309-084311.

[127] W. Merchan-Merchan, A.V. Saveliev, A.M. Taylor, Nucleation and growth mechanism for flame synthesis of MoO_2 hollow microchannels with nanometer wall thickness, Micron, 40 (2009) 821-826.

[128] L.Q. Mai, B. Hu, W. Chen, Y.Y. Qi, C.S. Lao, R.S. Yang, Y. Dai, Z.L. Wang, Lithiated MoO_3 nanobelts with greatly improved performance for lithium batteries, Adv. Mater., 19 (2007) 3712-3716.

[129] B. Hu, L. Mai, W. Chen, F. Yang, From MoO_3 nanobelts to MoO_2 nanorods: Structure transformation and electrical transport, ACS Nano, 3 (2009) 478-482.

[130] B. Yan, Z. Zheng, J. Zhang, H. Gong, Z. Shen, W. Huang, T. Yu, Orientation controllable growth of MoO_3 nanoflakes: Micro-raman, field emission, and birefringence properties, J. Phys. Chem. C, 113 (2009) 20259-20263.

[131] J. Zhou, N.S. Xu, S.Z. Deng, J. Chen, J.C. She, Z.L. Wang, Large-area nanowire arrays of molybdenum and molybdenum oxides: Synthesis and field emission properties, Adv. Mater., 15 (2003) 1835-1840.

[132] L. Zhou, L. Yang, P. Yuan, J. Zou, Y. Wu, C. Yu, α-MoO_3 nanobelts: A high performance cathode material for lithium ion batteries, J. Phys. Chem. C, 114 (2010) 21868-21872.

[133] R. Radhakrishnan, C. Reed, S.T. Oyama, Variability in the structure of supported MoO_3 catalysts: Studies using raman and X-ray absorption spectroscopy with ab initio calculations, J. Phys. Chem. B, 105 (2001) 8519-8530.

129

[134] E. Comini, L. Yubao, Y. Brando, G. Sberveglieri, Gas sensing properties of MoO_3 nanorods to CO and CH_3OH, Chem. Phys. Lett., 407 (2005) 368-371.

[135] J.N. Yao, K. Hashimoto, A. Fujishima, Photochromism induced in an electrolytically pretreated MoO_3 thin film by visible light, Nature, 355 (1992) 624-626.

[136] S.-Y. Lin, C.-M. Wang, K.-S. Kao, Y.-C. Chen, C.-C. Liu, Electrochromic properties of MoO_3 thin films derived by a sol-gel process, J. Sol-Gel Sci. Technol., 53 (2010) 51-58.

[137] R. Prakash, D.M. Phase, R.J. Choudhary, R. Kumar, Structural, electrical, and magnetic properties of $Mo_{1-x}Fe_xO_2$ (x = 0–0.05) thin films grown by pulsed laser ablation J. Appl. Phys., 103 (2008) 043712.

[138] P.M. Woodward, A.W. Sleight, T. Vogt, Structure refinement of triclinic tungsten trioxide, J. Phys. Chem. Solids, 56 (1995) 1305-1315.

[139] J.S.E.M. Svensson, C.G. Granqvist, Electrochromic tungsten oxide films for energy efficient windows, Sol. Energ. Mater., 11 (1984) 29-34.

[140] A.C. Dillon, A.H. Mahan, R. Deshpande, P.A. Parilla, K.M. Jones, S.-H. Lee, Metal oxide nano-particles for improved electrochromic and lithium-ion battery technologies, Thin Solid films, 516 (2008) 794–797.

[141] X. Chang, S. Sun, Z. Lib, X. Xub, Y. Qiu, Assembly of tungsten oxide nanobundles and their electrochromic properties, Applied Surface Science, 257 (2011) 5726-5730.

[142] Y. He, Z. Wu, L. Fu, C. Li, Y. Miao, L. Cao, H. Fan, B. Zou, Photochromism and Size Effect of WO3 and WO3-TiO2 Aqueous Sol, Chemistry of Materials, 15 (2003) 4039-4045.

[143] M. Breedon, P. Spizzirri, M. Taylor, J.d. Plessis, D. McCulloch, J. Zhu, L. Yu, Z. Hu, C. Rix, W. Wlodarski, K. Kalantar-zadeh, Synthesis of Nanostructured Tungsten Oxide Thin Films: A Simple, Controllable, Inexpensive, Aqueous Sol-Gel Method, Crystal Growth and Design, 10 (2010) 430-439.

[144] S. Wang, Nano-crystalline tungsten oxide NO2 sensor, Sensors and Actuators B: Chemical, 94 (2003) 343-351.

[145] X.-L. Li, J.-F. Liu, Y.-D. Li, Large-Scale synthesis of tungsten oxide nanowires with high aspect ratio, Inorganic Chemistry, 42 (2003) 921-924.

[146] D. Chen, J. Ye, Hierarchical WO_3 Hollow Shells: Dendrite, Sphere, Dumbbell, and Their Photocatalytic Properties, Adv. Funct. Mater., 18 (2008) 1922–1928.

[147] P.F. Carcia, E.M.M. III, Synthesis and properties of thin film polymorphs of molybdenum trioxide, Thin Solid Films, 155 (1987) 53-63.

[148] L. Kihlborg, The crystal chemistry of molybdenum oxides, in: Nonstoichiometric Compounds, American Chemical Society, 1963, pp. 37-45.

[149] A.K. Prasad, P.I. Gouma, MoO_3 and WO_3 based thin film conductimetric sensors for automotive applications, J. Mater. Sci., 38 (2003) 4347-4352.

[150] K. Galatsis, Y. Li, W. Wlodarski, C. Cantalini, M. Passacantando, S. Santucci, MoO_3, WO_3 single and binary oxide prepared by sol-gel method for gas sensing applications, J. Sol-Gel Sci. Technol., 26 (2003) 1097-1101.

[151] O. Merdrignac-Conanec, P.T. Moseley, Gas sensing properties of the mixed molybdenum tungsten oxide, $W_{0.9}Mo_{0.1}O_3$, J. Mater. Chem., 12 (2002) 1779-1781.

[152] K. Galatsis, Y.X. Li, W. Wlodarski, K. Kalantar-zadeh, Sol–gel prepared MoO_3-WO_3 thin-films for O_2 gas sensing, Sensor. Actuat. B, 77 (2001) 478-483.

[153] S.-H. Baeck, T.F. Jaramillo, D.H. Jeong, E.W. McFarland, Parallel synthesis and characterization of photoelectrochemically and electrochromically active tungsten-molybdenum oxides, Chem. Commun., (2004) 390-391.

[154] C.G. Granqvist, Electrochromic tungsten oxide films: Review of progress 1993–1998, Sol. Energy Mater. Sol. Cells, 60 (2000) 201-262.

[155] K. Gesheva, A. Szekeres, T. Ivanova, Optical properties of chemical vapor deposited thin films of molybdenum and tungsten based metal oxides, Sol. Energy Mater. Sol. Cells, 76 (2003) 563-576.

[156] X. Fang, B. Guo, Y. Shi, B. Li, C. Hua, C. Yao, Y. Zhang, Y.-S. Hu, Z. Wang, G.D. Stucky, L. Chen, Enhanced Li storage performance of ordered mesoporous MoO_2 via tungsten doping Nanoscale, (2012) 1541-1544.

[157] L. Kondrachova, B.P. Hahn, G. Vijayaraghavan, R.D. Williams, K.J. Stevenson, Cathodic electrodeposition of mixed molybdenum tungsten oxides from peroxo-polymolybdotungstate solutions, Langmuir, 22 (2006) 10490-10498.

[158] S. Li, M.S. El-Shall, Synthesis and characterization of photochromic molybdenum and tungsten oxide nanoparticles, Nanostruct. Mater., 12 (1999) 215–219.

[159] L. Zheng, Y. Xu, D. Jin, Y. Xie, Novel metastable hexagonal MoO_3 nanobelts: Synthesis, photochromic, and electrochromic properties, Chem. Mater., 21 (2009) 5681-5690.

[160] K.A. Gesheva, A. Cziraki, T. Ivanova, A. Szekeres, Crystallization of chemically vapor deposited molybdenum and mixed tungsten/molybdenum oxide films for electrochromic application, Thin Solid Films, 515 (2007) 4609-4613.

[161] T. Ivanova, K. A. Gesheva, M. Ganchev, E. Tzvetkova, Electrochromic behavior of CVD molybdenum oxide and Mo-W mixed-oxide thin films, J. Mater. Sci. Mater. Electron., 14 (2003) 755-758.

[162] X.L. Sun, A.H. Chen, H.Z. Zhang, H.T. Cao, Optical and Electrochromic Properties of Sol-Gel Deposited Mixed MoO_3-WO_3 Thin Films, Adv. Mat Res., 79-82 (2009) 843-846.

[163] C.E. Tracy, D.K. Benson, Preparation of amorphous electrochromic tungsten oxide and molybdenum oxide by plasma enhanced chemical vapor deposition J. Vac. Sci. Technol. A, 4 (1986) 2377-2383.

[164] U. Cvelbar, Z. Chen, I. Levchenko, R.M. Sheetz, J.B. Jasinski, M. Menon, M.K. Sunkara, K.K. Ostrikov, Sub-oxide-to-metallic, uniformly-nanoporous crystalline nanowires by plasma oxidation and electron reduction, Chem. Commun., 48 (2012) 11070-11072.

[165] K.A. Gesheva, T. Ivanova, A low-temperature atmospheric pressure CVD process for growing thin films of MoO_3 and MoO_3-WO_3 for electrochromic device applications, Chem. Vap. Deposition, 12 (2006) 231-238.

[166] T.M. McEvoy, K.J. Stevenson, Electrochemical preparation of molybdenum trioxide thin films: effect of sintering on electrochromic and electroinsertion properties, Langmuir, 19 (2003) 4316-4326.

[167] A. Vomiero, G.D. Mea, M. Ferroni, G. Martinelli, G. Roncarati, V. Guidi, E. Comini, G. Sberveglieri, Preparation and microstructural characterization of nanosized Mo-TiO$_2$ and Mo-W-O thin films by sputtering: tailoring of composition and porosity by thermal treatment Mater. Sci. Eng., B, 101 (2003) 216-221.

[168] K. Galatsis, Y.X. Li, W. Wlodarski, E. Comini, G. Sberveglieri, C. Cantalini, S. Santucci, M. Passacantando, Comparison of single and binary oxide MoO$_3$, TiO$_2$ and WO$_3$ sol-gel gas sensors, Sensor. Actuat. B, 83 (2002) 276-280.

[169] L. Cai, P.M. Rao, X. Zheng, Morphology-Controlled Flame Synthesis of Single, Branched, and Flower-like α-MoO$_3$ Nanobelt Arrays, Nano. Lett., 11 (2011) 872-877.

[170] L. Cai, P.M. Rao, Y. Feng, X. Zheng, Flame synthesis of 1-D complex metal oxide nanomaterials, Proc. Combust. Inst., 34 (2013) 2229-2236.

[171] Y. Feng, I.S. Cho, L. Cai, P.M. Rao, X. Zheng, Sol-flame synthesis of hybrid metal oxide nanowires, Proc. Combust. Inst., 34 (2013) 2179-2186.

[172] W. Merchan-Merchan, A.V. Saveliev, S.G. Sanmiguel, M. Farmahini-Farahani, Flame volume synthesis of carbon-coated WO$_3$ nanoplatelets and nanorods, J. Nanopart. Res., 14 (2012) 1276-1278.

[173] Z. Hu, C. Zhou, M. Zheng, J. Lu, B. Varghese, H. Cheng, C.-H. Sow, K-enriched moo3 nanobundles: A layered structure with high electric conductivity, J. Phys. Chem. C, 116 (2012) 3962−3967.

[174] E. Salje, R. Gehlig, K. Viswanathan, Structural phase transition in mixed crystals W$_x$MO$_{1−x}$O$_3$, J. Solid State Chem., 25 (1978) 239-250.

[175] W. Widiyastuti, A. Purwanto, W.-N. Wang, F. Iskandar, H. Setyawan, K. Okuyama, Nanoparticle formation through solid-fed flame synthesis: Experiment and modeling, AlChE J., 55 (2009) 885-895.

[176] T. Kodas, Aerosol processing of materials, Wiley-VCH, New York, 1999.

[177] M. Figlarz, New oxides in the WO$_3$-MoO$_3$ system, Prog. Solid St. Chem., 19 (1989) 1-46.

[178] W.F.v. Dorp, C.W. Hagen, A critical literature review of focused electron beam induced deposition J. Appl. Phys., 104 (2008) 081301.

[179] K.L. Klein, S.J. Randolph, J.D. Fowlkes, L.F. Allard, H.M.M. III, M.L. Simpson, P.D. Rack, Single-crystal nanowires grown via electron-beam-induced deposition Nanotechnology, 19 (2008) 345705.

[180] Z.-Q. Liu, K. Mitsuishi, K. Furuya, Crystallization of Focused-Electron-Beam Deposited Tungsten Wire on Molybdenum Substrate, Jpn. J. Appl. Phys., 42 (2006) 5548-5551.

[181] K. Kuwana, K. Saito, Modeling CVD synthesis of carbon nanotubes: Nanoparticle formation from ferrocene, Carbon, 43 (2005) 2088-2095.

[182] M. Mahmoudi, M.A. Shokrgozar, A. Simchi, M. Imani, A.S. Milani, P. Stroeve, H. Vali, U.O. Häfeli, S. Bonakdar, Multiphysics Flow Modeling and in Vitro Toxicity

of Iron Oxide Nanoparticles Coated with Poly(vinyl alcohol), J. Phys. Chem. C, 113 (2009) 2322–2331.

[183] H.W.P. Koops, C. Schössler, A. Kaya, M. Weber, Conductive dots, wires, and supertips for field electron emitters produced by electron-beam induced deposition on samples having increased temperature J. Vac. Sci. Technol. B, 14 (1996) 4105-4109.

[184] K. Mølhave, D.N. Madsen, S. Dohn, P. Bøggild, Constructing, connecting and soldering nanostructures by environmental electron beam deposition, Nanotechnology, 15 (2004) 1047-1053.

[185] L. Rotkina, S. Oh, J.N. Eckstein, S.V. Rotkin, Logarithmic behavior of the conductivity of electron-beam deposited granular Pt/C nanowires, Phys. Rev. B, 72 (2005) 233407.

[186] G. Shen, Y. Bando, D. Golberg, C. Zhou, Electron-Beam-Induced Synthesis and Characterization of $W_{18}O_{49}$ Nanowires, J. Phys. Chem. C, 112 (2008) 5856-5859.

[187] S.-H. Lee, R. Deshpande, P.A. Parilla, K.M. Jones, B. To, A.H. Mahan, A.C. Dillon, Crystalline WO_3 nanoparticles for highly improved electrochromic applications, Adv. Mater., 18 (2006) 763-766.

[188] C. Bock, B. MacDougall, The electrochemical oxidation of organics using tungsten oxide based electrodes, Electrochim. Acta, 47 (2002) 3361-3373.

[189] I. Turyan, U.O. Krasovec, B. Orel, T. Saraidorov, R. Reisfeld, D. Mandler, "Writing-reading-erasing" on tungsten oxide films using the scanning electrochemical microscope, Adv. Mater., 12 (2000) 330-333.

[190] J. Polleux, A. Gurlo, N. Barsan, U. Weimar, M. Antonietti, M. Niederberger, Template-Free Synthesis and Assembly of Single-Crystalline Tungsten Oxide Nanowires and their Gas-Sensing Properties, Angew, Chem. Int. Ed., 45 (2005) 261-265.

[191] S. Eibl, B.C. Gates, H. Knözinger, Structure of WO_x/TiO_2 catalysts prepared from hydrous titanium oxide hydroxide: Influence of peparation arameters, Langmuir, 17 (2001) 107-115.

[192] T. Kim, A. Burrows, C.J. Kiely, I.E. Wachs, Molecular/electronic structure–surface acidity relationships of model-supported tungsten oxide catalysts, J. Catal., 246 (2007) 370-381.

[193] J.F. Al-Sharab, R.K. Sadangi, V. Shukla, S.D. Tse, B.H. Kear, Synthesis of Nanostructured Tungsten Oxide ($WO_{2.9}$) Fibers and Discs, Cryst. Growth Des., 9 (2009) 4680-4684.

[194] W. Merchan-Merchan, M. Farmahini-Farahani, Flame synthesis of zinc oxide nanocrystals, Mater. Sci. Eng., B, 178 (2013) 127-134.

[195] W. Merchan-Merchan, M. Farmahini-Farahani, Rapid catalyst-free flame synthesis of α-Nb_2O_5 micro/nanorods, Mater. Chem. Phys., 140 (2013) 516-521.

[196] G.L. Frey, A. Rothschild, J. Sloan, R. Rosentsveig, R. Popovitz-Biro, R. Tenne, Investigations of nonstoichiometric tungsten oxide nanoparticles, J. Solid State Chem., 162 (2001) 300-314.

[197] R. Pandian, B.J. Kooi, J.T.M.D. Hosson, A. Pauza, Influence of electron beam exposure on crystallization of phase-change materials, J. Appl. Phys., 101 (2007) 053529.

[198] R.F. Egerton, P. Li, M. Malac, Radiation damage in the TEM and SEM, Micron, 35 (2004) 399-409.

[199] Z.W. Liu, Y. Bando, A novel method for preparing copper nanorods and nanowires, Adv. Mater., 15 (2003) 303-305.

[200] P.J. Feibelman, M.L. Knotek, Reinterpretation of electron-stimulated desorption data from chemisorption systems, Phys. Rev. B, 18 (1978) 6531–6539.

[201] M.L. Knotek, P.J. Feibelman, Ion desorption by core-hole auger decay, Phys. Rev. Lett., 40 (1978) 964–967.

[202] J.L. Morán-López, J.M. Sánchez, Advanced topics in materials science and engineering, Plenum Press, New York, 1993.

Appendix A- List of published papers

Journal Papers:

1. W. Merchan-Merchan, **M. Farmahini-Farahani**, Z.M. Rosenberg, "Electron-beam Induced Formation of Tungsten Sub-Oxide Nanorods from Flame-Formed Microcrystals," Mircon, 57, 23, 2014.

2. W. Merchan-Merchan and **M. Farmahini-Farahani**, "Rapid Catalyst-Free Flame Synthesis of α-Nb_2O_5 Micro/Nanorods," Materials Chemistry and Physics, 140, 516, 2013.

3. W. Merchan-Merchan and **M. Farmahini-Farahani**, "Flame Synthesis of Zinc Oxide Nanocrystals," Materials Science and Engineering B, 178, 127, 2013.

4. W. Merchan-Merchan, A.V. Saveliev, S.G. Sanmiguel, **M. Farmahini-Farahani**, "Flame Volume Synthesis of Carbon-coated WO_3 Nanoplatelets and Nanorods," J. of Nanoparticle Research, 49, 1276, 2012.

Conference Papers:

1. **M. Farmahini-Farahani**, A.V. Savaliev, W. Merchan-Merchan, "Synthesis of Niobium Pentoxide Micro/Nanorods in a Counter-Flow Flame," *8th US nat'l. Combust. Meeting*, Salt Lake City, UT, May 2013.

2. W. Merchan-Merchan, A.V. Saveliev, **M. Farmahini-Farahani**, *et al.*, "Flame Synthesis of Tungsten Oxide Nanostructures and Their Application for Increasing the Performance of Solar Cells," *MRS,* Boston, MA, Nov. 2012.

3. W. Merchan-Merchan, **M. Farmahini-Farahani**, "Rapid Combustion Synthesis of Zinc Oxide Nanostructures," *Nanotech 2012*, Santa Clara, CA, USA, Jun. 2012.

4. W. Merchan-Merchan, A.V. Saveliev, **M. Farmahini-Farahani**, "Hybrid Tungsten Oxide /Carbon Nanoplatelets and Nanorods Prepared Directly in a Flame Volume," *Intl. Conf. on Nanotechnology,* Omaha, NE, USA, Mar. 2012.